NANOMECHANICAL AND ELECTROMECHANICAL CHARACTERIZATION ON ZINC OXIDE NANOBELT USING ATOMIC FORCE MICROSCOPY

by

Minhua Zhao

BS, Zhejiang University, 1991

MS, Zhejiang University, 1994

Submitted to the Graduate Faculty of

School of Engineering in partial fulfillment

of the requirements for the degree of

Doctor of Philosophy

University of Pittsburgh

2004

UNIVERSITY OF PITTSBURGH

SCHOOL OF ENGINEERING

This dissertation was presented

by

Minhua Zhao

It was defended on

November 23, 2004

and approved by

Minking K. Chyu, Professor, Department of Mechanical Engineering

Scott X. Mao, Professor, Department of Mechanical Engineering

William S. Slaughter, Associate Professor, Department of Mechanical Engineering

Judith C. Yang, Associate Professor, Department of Materials Science & Engineering

Dissertation Director: Scott X. Mao, Professor, Department of Mechanical Engineering

NANOMECHANICAL AND ELECTROMECHANICAL CHARACTERIZATION ON ZINC OXIDE NANOBELT USING ATOMIC FORCE MICROSCOPY

Minhua Zhao, PhD

University of Pittsburgh, 2004

ZnO nanobelts are a group of quasi-one-dimensional nanostructures that have a unique rectangle-like cross section, with typical widths of several hundred nanometers, width-to-thickness ratios of 1 to 10, and lengths of tens to hundreds of micron meters. They are the promising candidates for nanoscale ultrahigh frequency resonator, nanosensors and nanoactuators due to their well-defined geometry, prefect single crystallinity and excellent piezoelectric properties. In this study, we revealed the following unique nanomechanical and electromechanical properties of a single ZnO nanobelt using Atomic Force Microscopy. (i) Elastic modulus, hardness and fracture toughness of the ZnO nanobelt are much smaller than its bulk counterpart. (ii) Strong photoinduced elastic effect is observed in ZnO nanobelt, while there is no effect in its bulk counterpart. (iii) The effective piezoelectric coefficient, d_{33}, of ZnO nanobelt is frequency dependent and much higher than that of its bulk counterpart. These unique properties cannot be accounted for using macroscale theory such as continuum mechanics, while they may be related to surface effects thanks to the high surface to volume ratio of ZnO nanobelt. One of the consequences of our findings is that these properties are fundamental to the real applications and may be universal phenomena in quasi-one-dimensional semiconducting nanostructures, which are becoming building blocks of MEMS (Micro Electromechanical Systems) and NEMS (Nano Electromechanical Systems).

TABLE OF CONTENTS

LIST OF TABLES

LIST OF FIGURES

ACKNOWLEDGEMENTS

My first acknowledgement must go to my advisor, Professor Scott X. Mao, who makes it possible for me to investigate the exciting fields of nanomechanics and atomic force microscopy. None of this work is possible without his financial support and professional guidance.

My special thanks go to our collaborator, Professor Zhonglin Wang, Department of Materials Science and Engineering, Georgia Institute of Technology. The pioneering work on ZnO nanobelt in his group ignites my interests of this study. I am grateful to his provision of the samples and helpful discussion on the papers published on Applied Physics Letters and Nano Letters.

My next acknowledgement goes to our former and current group members: Nianqiang Wu, Nicolas Perrusquia, Brain Ennis, Zheng Chen, Huiyao Wang, Jianhui Xu, Zhiwei Shan and Pavin Ganmon. In particular, I appreciate the contribution of Dr. Chen 's work on synthesis of ZnO nanostructures and Jianhui's work on UV light sensor. My thanks also go to my friends at PITT, especially Fengtin Xu and Hongzhou Ma.

I appreciate the time spent by the committee members and their suggestions to improve the thesis.

Finally, I would like to dedicate this thesis to my dear wife Ling Zhu. Her support, encouragement and companionship have turned my life into a pleasant journey during PhD study.

1.0 GENERAL INTRODUCTION

One dimensional (1D) semiconducting nanostructures are the key components for microelectromechanical systems (MEMS) and nanoelectromechanical systems (NEMS) fabrication. With a continuing miniaturization trend in MEMS and NEMS, questions inevitably arise as to how valid it is to extrapolate material properties downward from the macroscale to microscale or nanoscale. No clear answer has been derived yet, although there are many examples, which show that material properties, such as mechanical, electrical, magnetic and thermal properties, are quite different in various scales. This study focuses on the mechanical and electromechanical properties at the nanoscale, using ZnO nanobelt as a model material and atomic force microscopy as a main tool for characterization.

ZnO nanobelt, a quasi-one-dimensional belt-like nanostructure (so called nanobelt) with unique rectangular cross section, was first reported in Science by Dr. Wang's group [1]. The belt-like morphology is distinct from those of semiconducting nanowires. Since its first discovery in 2001, it has attracted considerable attention, which is manifested by the over 1000 references on the related research. The discovery of nanobelts is being attributed to the same category as the discovery of the carbon nanotubes and it is stimulating a vast interest in investigating nanobelt-based materials and applications [2-10]. The application of ZnO nanobelts as nanosensors[11, 12], nanocantilevers[13], field effect transistors[14] and nanoresonators[15] has been reported. However, we still know little about its mechanical and electromechanical properties, which are fundamental to the real applications. For instance, ZnO is a traditional piezoelectric material with good electromechanical coupling. Piezoelectric ZnO is mainly employed in the form of polycrystalline thin film[16-23]. The grain boundary and other defects

may weaken the piezoelectric coefficients because they pin the domain walls and inhibit poling of the materials. As ZnO nanobelt is perfect single crystalline and almost defect free, it is interesting to find out if it has much higher piezoelectric coefficient than that of polycrystalline thin film. The piezoelectric coefficients of the ZnO nanobelt are also critical parameters in the design of nanosensors or nanoactuators using its piezoelectric properties. In the meantime, with a well-defined geometry and perfect single crystallinity, ZnO nanobelt is likely to be an ideal system for understanding mechanical behaviors at nanoscale almost absence of stress and defects.

Hence, fundamental understanding on the nanomechanical and electromechanical behavior of a single ZnO nanobelt is very desired. A key challenge to today's research is the experimental difficulty in manipulating and testing the physical properties of a single nanobelt, for the small size of the object prohibits the applications of the well-established techniques, such as acoustic wave method for Young's modulus measurement, tensile test for strength and resonance and anti-resonance method for piezoelectric coefficient measurement. On the other hand, atomic force microscopy (AFM) has been applied successfully in nanoscale mechanical and electromechanical characterization on 1D nanostructures since 1990s [24-36]. Most of these work are related to one dimensional carbon nanotubes, while characterization on quasi-one-dimensional nanostructures such as ZnO nanobelt, is much less developed [37-39]. Hence, the objectives of the current research are not only to characterize nanoscale mechanical and electromechanical behaviors of ZnO nanobelt using AFM, but also to develop new AFM testing techniques applicable to the quasi-one-dimensional nanostructures.

The following chapters will be organized as follows. Chapter 2 is the background introduction to ZnO, ZnO nanobelt, AFM and nanoindenter. Chapter 3 is about nanomechanical

characterization on ZnO nanobelt using Triboscope nanoindenter and AFM cantilever indenter. The deformation realms are classified into the 3 stages: elasticity, plasticity and fracture. Strong optical and mechanical coupling in ZnO nanobelt is covered in Chapter 4, while Chapter 5 deals with the electro-mechanical coupling in ZnO nanobelt. In addition, a quick responsive and highly sensitive and selective UV photodetector based on a single ZnO nanobelt is demonstrated in Chapter 6. Finally, conclusions and outlook of this research is provided in Chapter 7.

2.0 BACKGROUND

2.1 STRUCTURES AND PROPERTIES OF ZNO

Zinc oxide has a hexagonal wurtzite structure with lattice parameters a=0.3249nm and c=0.5206nm. The c/a ratio is 1.602, which is slightly less than the value of 1.633 for the ideal close packed structure. The structure of ZnO [3] can be simply described as a series of alternating planes composed of tetrahedrally coordinated Zn^{2+} and O^{2-} ions, stacking alternatively along the c-axis (Figure 2.1).

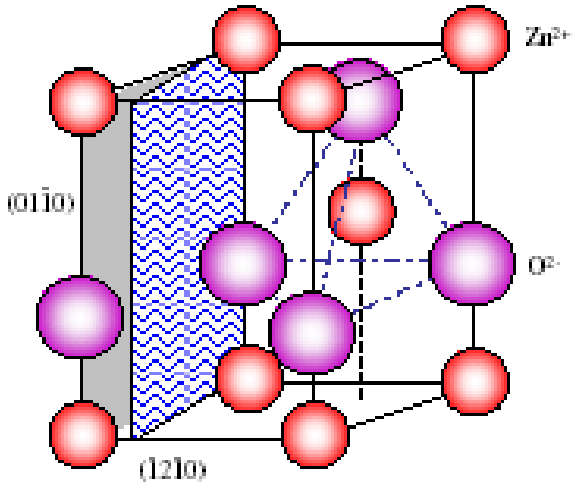

Figure 2.1 The wurtzite structural model of ZnO

The Zn-O distance is 1.922Å parallel to the c-axis and 1.973Å in the other three directions of the tetrahedral arrangements of nearest neighbors. The lack of the inversion symmetry in the ZnO tetrahedral structure is the origin of its piezoelectricity and pyroelectricity. Another important feature of ZnO is polar surfaces. The most common polar surface is the basal plane. The oppositely charged ions produce positively charged Zn- (0001) and negatively charged O-

$(000\bar{1})$ surfaces, resulting in a spontaneous polarization along the c-axis and vastly different properties in Zn-terminated and O-terminated plane. The other two commonly observed facets for ZnO are $\{2\bar{1}\bar{1}0\}$ and $\{01\bar{1}0\}$, which are non-polar surfaces and have lower energy than the $\{0001\}$ facets. In addition, ZnO is a wide band-gap (3.37eV) II-VI semiconductor that is promising in short wavelength optoelectronic applications. The high exciton binding energy (60meV) in ZnO crystal can ensure efficient excitonic emission at room temperature.

ZnO has been under intensive investigation since the 1950s. It is a versatile functional material with a variety of practical applications, such as transparent conductive films[21], varistors [40], catalysts [19], sensors [22], transducers [23], surface acoustic wave (SAW) [41]filters and optoelectronic devices [17]. In particular, with the advance of the nanotechnology in the recent years, one-dimensional (1D) ZnO nanostructures have received broad attention due to unique electrical, optical, chemical and mechanical properties compared to their bulk (3D), thin film (2D) and nanoparticles (0D) counterparts.

In geometrical structures, 1D nanostructures can be classified into three main groups: 1) hollow nanotubes, 2) solid nanowires, and 3) nanobelts or nanoribbons. The first two have a common characteristic of cylindrical symmetric cross section, while the last have a rectangular cross-section, in correspondence to a belt-like morphology. ZnO nanobelt was first reported by Dr. Wang's group in 2001. The belt-like morphology is distinct from other nanostructures. With a well-defined homogeneous geometry and perfect crystallinity, ZnO nanobelt is likely to be a model material for the fundamental understanding in the mechanical, electrical, optical, thermal, and ionic transport processes in 1D semiconducting nanostructures. In fact, the discovery of nanobelts is being attributed to the same category as the discovery of nanotubes and has attracted considerable attention [2]. Hence, we will focus on ZnO nanobelt thereafter.

2.2 SYNTHESIS OF ZNO NANOBELT

2.2.1 Thermal evaporation without catalyst

Over the past a few years, one-dimensional ZnO nanostructures including nanowires, nanobelts, nanocables and nanotube as well as tetrapod nanorods have been synthesized by various methods such as catalytic growth *via* the vapor-liquid-solid (VLS) mechanism[42], thermal evaporation[1] and wet chemical method[43, 44]. The vapor transport and condensation process has been widely used to synthesize various ZnO nanostructures due to simplicity, low cost and fewer necessary apparatuses[1, 42, 45, 46] .

ZnO nanobelt can be synthesized via thermal evaporation by a solid vapor process with or without the catalyst. In this study, for the purity of the sample, ZnO nanobelt was synthesized by thermal evaporation process without the presence of the catalyst. The processes are usually carried out in a horizontal tube furnace, as shown in Figure 2.2.

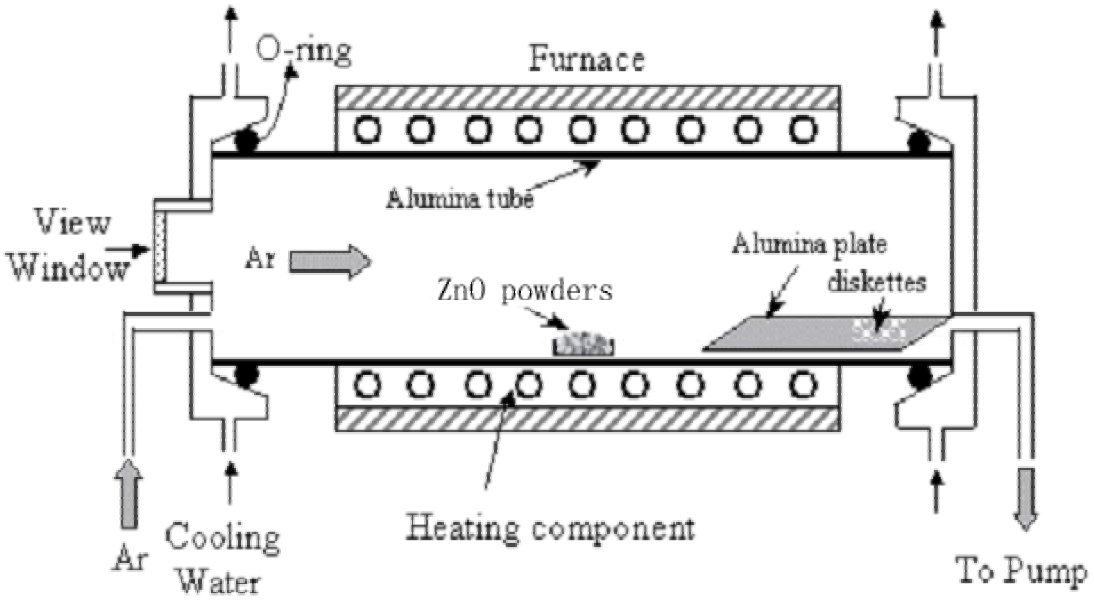

Figure 2.2 Schematic of the synthesis of the ZnO nanobelts by thermal evaporation

ZnO powders (99.99%) was placed in an alumina boat and then loaded into the central region of the alumina tube, after the tube had been evacuated by a mechanical rotary pump to a pressure of 5Pa, a carrier gas of high purity Ar was kept flowing at a rate of 200sccm. The pressure inside tube was kept at 400 torr until the temperature increased to 1400°C. The thermal evaporation was performed at 1400°C for 3.5 hours at 100 torr. White wool-like products were collected on the alumina substrate, placed in the temperature range of 800-1100°C at the downstream end of alumina tube. The temperature gradient was established by using a movable stainless cooling finger at the outlet end of the alumina tube. SEM observations reveal that the products consist of a large quantity of belt-like nanostructures with typical lengths in the range of several tens to several hundreds of micrometers (Figure 2.3). Some of them even have lengths on the order of millimeters. EDS microanalysis and powder XRD measurement [1] (Figure 2.4) show that the sample is wurtzite (hexagonal) structured ZnO with lattice constants of a=3.249 Å and C=5.206Å, consistent with the standard value for bulk ZnO.

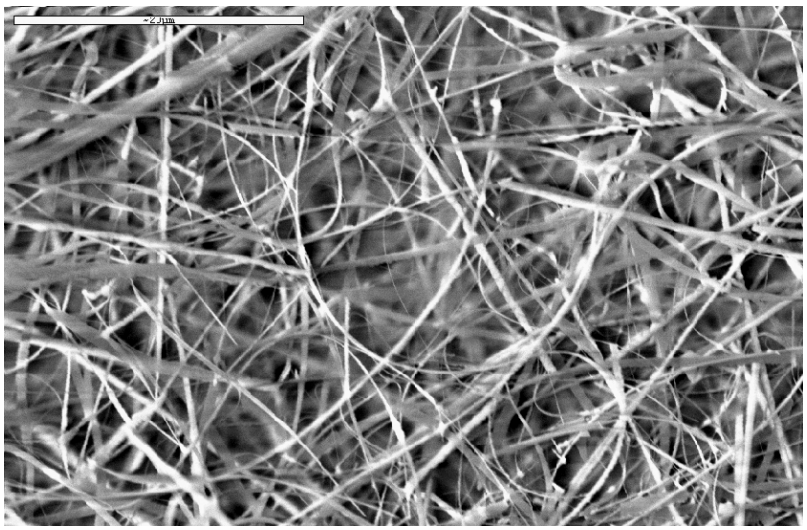

Figure 2.3 SEM pictures of as-synthesized ZnO nanobelts (scale bar 20μm)

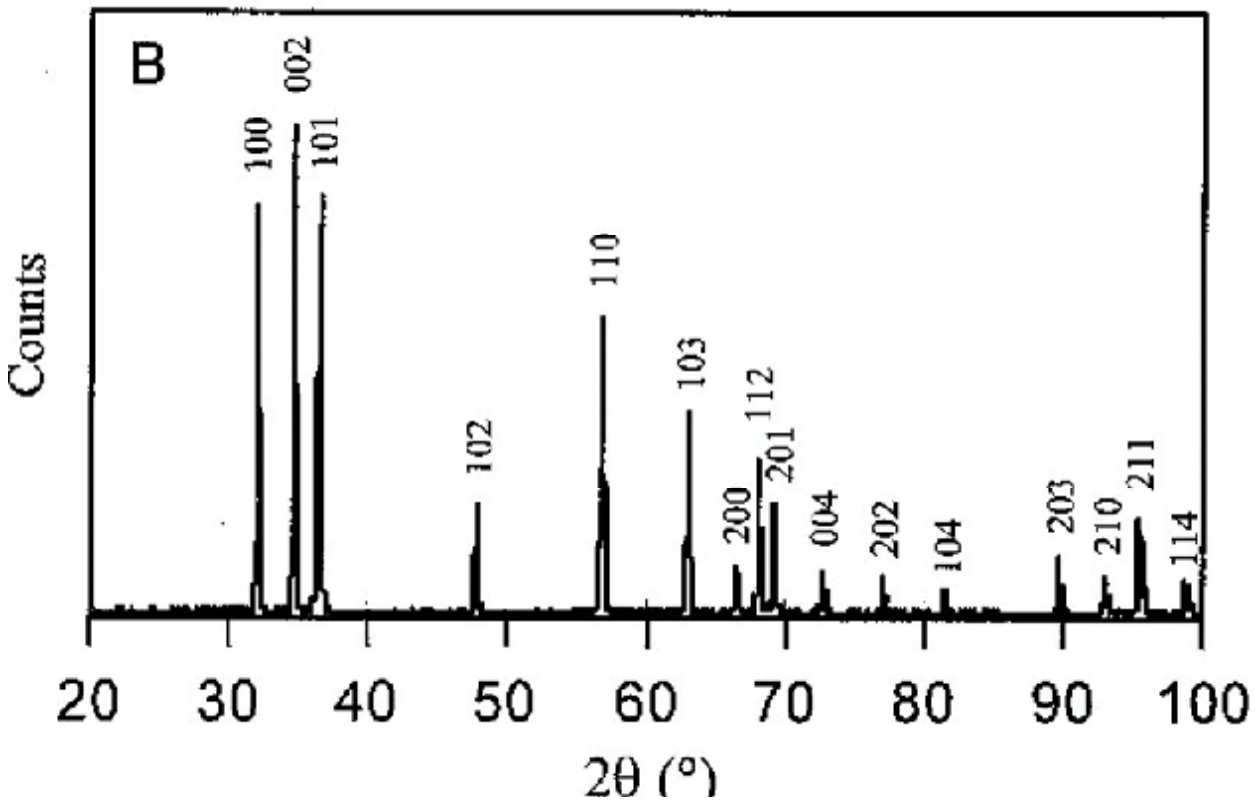

Figure 2.4 XRD patterns of ZnO nanobelts [1]

TEM images [1] reveal that the geometrical shape of ZnO nanostructures is a belt (Figure 2.5, A to C). Each nanobelt has a uniform width along its entire length, and the typical widths of the nanobelt are in the range of 50 to 800nm. A ripple like contrast observed in the TEM image is due to strain resulting from the bending of the belt. Figure 2.5D is a cross-sectional TEM image taken from a nanobelt, which exhibits a rectangular cross section. The typical thickness and width-to-thickness ratios of the ZnO nanobelts are in the range of 20 to 600nm and ~1 to 10 respectively. HRTEM and electron diffraction show that the ZnO nanobelts are structurally uniform and single crystalline but with two different growth directions. The nanobelt, growing along [0001] and enclosed by $\pm(2\bar{1}\bar{1}0)$ and $\pm(01\bar{1}0)$ facets, shows no defect and no dislocation; the one growing along $[01\bar{1}0]$ and enclosed by $\pm(0001)$ and $\pm(2\bar{1}\bar{1}0)$ facets is also dislocation free but with only a single stacking fault that is parallel to the axis and runs through out the entire length

of the nanobelt (Figure 2.5, E and G). The surfaces of the nanobelts are clean, atomically sharp and without any sheathed amorphous phase (Figure 2.5F).

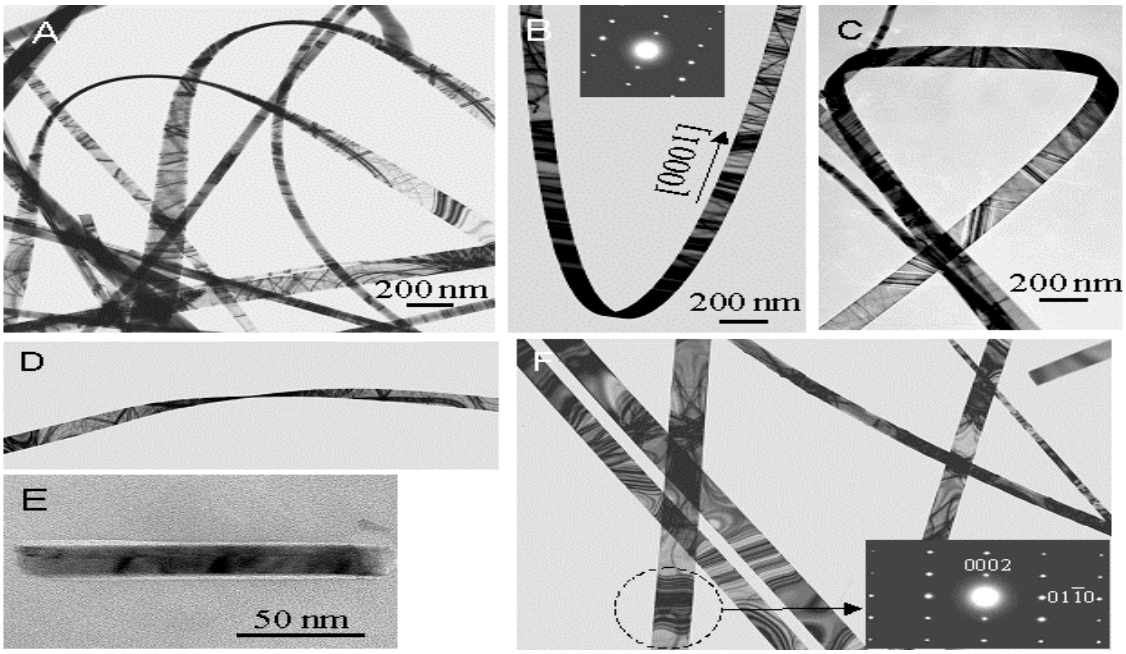

Figure 2.5 TEM analysis on ZnO nanobelts [1]

2.2.2 Thermal evaporation with addition

Synthesis of ZnO nanobelt by thermal evaporation without catalyst requires high temperature of 1400 °C, which is inconvenient in many cases. So the synthesis of ZnO nanobelt was also carried out by thermal evaporation with addition at much lower temperature [47]. A mixture of pure ZnO powder (Alfa Aesar, 99.99%) and graphite powder (Alfa Aesar, -300 mesh, 99.9%) in a 1:1 molar ratio was placed at the center region of a quartz tube. The quartz tube was then inserted into the furnace. The mixture was heated to 1100 °C with a heating rate of 50^{o}C/min under a flow of high purity nitrogen as a carrier gas at a rate from 70 to more than 150 sccm (standard cubic centimeter per minute). The growth time was typically 0.5-1 h. The temperature

distribution along the quartz tube was measured before synthesis, so that the growth temperature of different products can be determined. After evaporation and deposition, the quartz tube was drawn out from the furnace when it was cooled down to about 500^{o}C. By adjusting the flow rate of N_2, different products were obtained in different positions on the inner wall of the quartz tube, namely from ZnO nanotetrapods to ZnO and Zn nanowires (some of them are nanobelts, same for the following). The as-grown Zn nanowires were further oxidized in air at 800^{o}C for 1 h. The crystal structure and morphology were characterized using X-ray diffractometer (XRD-PHILIPS APD 3720, Cu *Kα*), field-emission scanning electron microscope (FE-SEM, PHILIPS XL30) with which an energy-dispersive X-ray spectroscopy (EDX) is equipped and a transmission electron microscope (TEM, JEOL 2000F at 200 kV). The photoluminescence (PL) measurements were carried out at room temperature on a spectrophotometer with a Xe lamp as the excitation light source (325 nm).

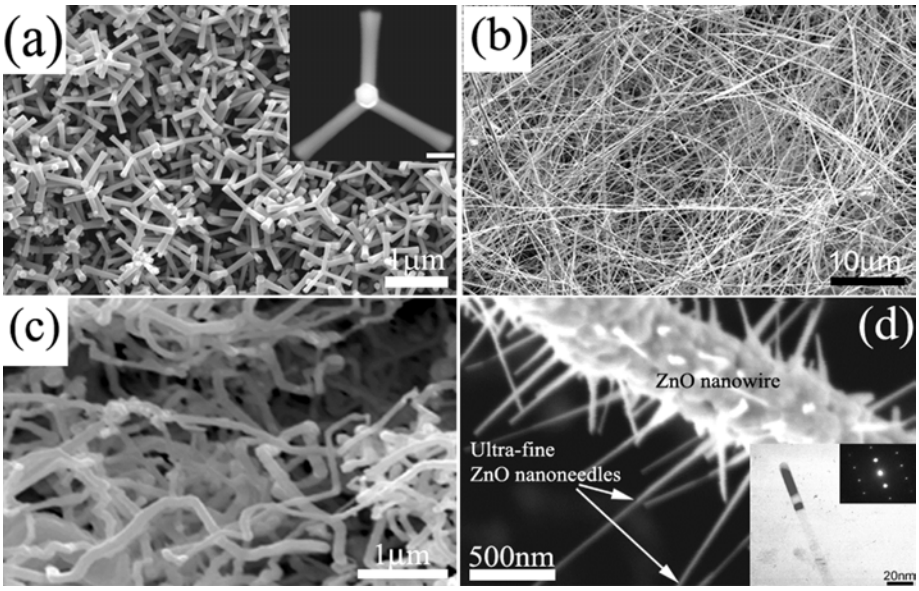

Figure 2.6 FE-SEM images of ZnO and Zn nanocrystals: (a) ZnO nanotetrapods, inset showing an individual nanotetrapod, scale bar =100 nm; (b) ZnO nanowires; (c) Zn nanowires; (d) ZnO nanowires + nanoneedles after oxidation of Zn nanowires at 800^{o}C for 1h, inset showing TEM image of a ZnO nanoneedle and corresponding SAD pattern.

Under N_2 flow rate of 70 sccm, fine ZnO nanotetrapods were deposited on the inner wall of the quartz tube located downstream of the carrier gas by a distance of approximately 88-106 mm from the reactants, where the growth temperature was estimated to be in the range of 950-980^{o}C. Figure 2.6(a) shows the SEM image of as-synthesized ZnO nanotetrapods. The diameter of tetrapods legs typically ranged from 80 nm to 200 nm, and ~1 μm in length. The cross-sectional views were hexagonal in shape for each leg (insets in Figure 2.6(a)), indicating the growth of nanotetrapods was in thermodynamical equilibrium condition. The morphology of our synthesized ZnO nanotetrapods was somewhat different from those reported in the literatures [48-51] where ZnO nanotetrapods usually had a needle shape at the tip of tetrapod legs; whereas a hexagonal flat surface was always maintained at the tip of present tetrapod legs.

When the flow rate of N_2 was tuned to 90-100 sccm, instead of nanotetrapods, ZnO nanowires were formed (Figure 2.6(b)). The diameter of ZnO nanowires normally ranged from 60-120 nm and their lengths were 10-40 μm, although some thinner wires (~30 nm) were also observed. XRD measurements (Figure 2.7) demonstrated that ZnO nanotetrapods and nanowires were hexagonal wurtzite structured ZnO with lattice parameters of a = 0.3249 nm and c = 0.5206 nm. The strong intensities relative to the background signal indicate the high purity and high crystallite of ZnO nanotetrapods and nanowires. EDX analysis of the ZnO nanotetrapods and nanowires showed that the atomic composition ratio of O to Zn ($R_{O:Zn}$) is about 0.9 and 0.78, respectively.

The dark-gray Zn nanowires were formed as N_2 flow rate was increased to more than 150 sccm. Zn nanowires exhibited an entangled and curved wire-like nanostructures (Figure 2.6(c)). They were hexagonal structure Zn with lattice constants of a = 0.2655 nm and c = 0.4928 nm, in accordance with the JCPDS data of bulk Zn, as shown in Figure 2.7.

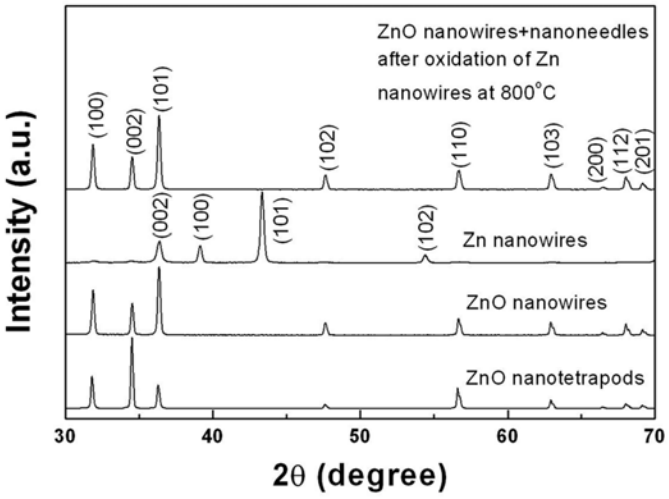

Figure 2.7 X-ray diffraction spectrums of ZnO nanotetrapods, ZnO nanowires, Zn nanowires and ZnO nanowires + nanoneedles after oxidation of Zn nanowires.

However, the peaks from the wurtzite-structural ZnO with significant low intensity were also found, indicating that Zn nanowires had been slightly oxidized by the residual oxygen within the tube during synthesis. This is similar to that reported by Lee [45] where coaxial Zn/ZnO nanocables were formed by heating ZnS powders at 1300°C using a pre-evacuated tube furnace under a flow of Ar + 5%H_2. After oxidation of the Zn nanowires in air at 800°C, white wool products were produced (Figure 2.6(d)). The XRD Pattern of oxidized Zn nanowires (Figure 2.8) can be indexed to a hexagonal wurtzite structured ZnO. From Figure 2.6(d), it was worthy noting that besides thick ZnO nanowires, abundant ultra-fine (UF) ZnO nanoneedles (as shown by

arrows) grew out from thick ZnO nanowires base in a radial direction. The diameters of these in-situ grown UF-ZnO nanoneedles were in the range of 8-20 nm and their lengths were 400 nm–1 μm, having a high aspect ratio of ~ 50. Inset in Figure 2.6(d) shows a TEM image of an individual UF-ZnO nanoneedle (8 nm in diameter). The UF-ZnO nanowires were single crystalline and the growth direction was along [0001] as evidenced by the SAD pattern (insert in Figure 2.6(d)). $R_{O:Zn}$ of ZnO nanowires + nanoneedles was determined to be 0.85 by EDX.

Figure 2.8 shows PL spectra of the ZnO nanostructures synthesized under different N_2 flow rate. In addition to the emissions in UV region (380~386 nm) for all the samples, which correspond to the near band edge emission, a strong broad peak at ~490 nm (2.53 eV) was detected from the ZnO nanotetrapods (Pattern A) and ZnO nanowires + nanoneedles (Pattern D). This deep-band green light emission had been reported from ZnO nanotetrapods in the previous work [48, 51] and was attributed to the single ionized oxygen vacancy in ZnO [52]. ZnO nanowires + nanoneedles formed at 800^{o}C during oxidation showed a poorer UV and a stronger green emission than ZnO nanotetrapods did. This was due to a large concentration of defects formed during oxidation process, and the oxidation temperature was not high enough to get rid of these defects [53]. Two very weak peaks (382 nm and 492 nm) from Zn nanowires (Pattern C) were due to surface oxidation. However, different from above PL spectra, ZnO nanowires exhibited two much stronger visible emissions (Pattern B in Figure 2.9). One was a blue band around 442 nm (2.81 eV), and the other luminescence band was a green-yellow light emission at 564 nm (2.2 eV). This blue emission is very interesting since it was rarely observed in ZnO nanowires, although some researchers have reported this blue emission (446 nm) for ZnO films and whiskers [54]. Previous study on ZnO film proved that the blue emission was related to the oxygen vacancy in the ZnO film [55], and the oxygen vacancy could be decreased by increasing

the oxygen partial pressure [56]. Deposition of ZnO nanowires under relative large N_2 flow rate, i.e. low oxygen partial pressure condition, might resulted in significant oxygen vacancies in the ZnO nanowires, as evidenced by lower $R_{O:Zn}$ (0.78). Oxygen vacancies can produce the deep donor level located at 1.3-1.6 eV below the conductor band [57], and the shallow donor level below the conductor band at 0.3-0.5 eV . The energy interval from the top of the valence band to the shallow donor level is about 2.8 eV, which is consistent with the photon energy of the 2.81 eV blue emission observed in the present study. Therefore, we think this blue emission originated from the electron transition from the shallow donor level of oxygen vacancies to the valence band.

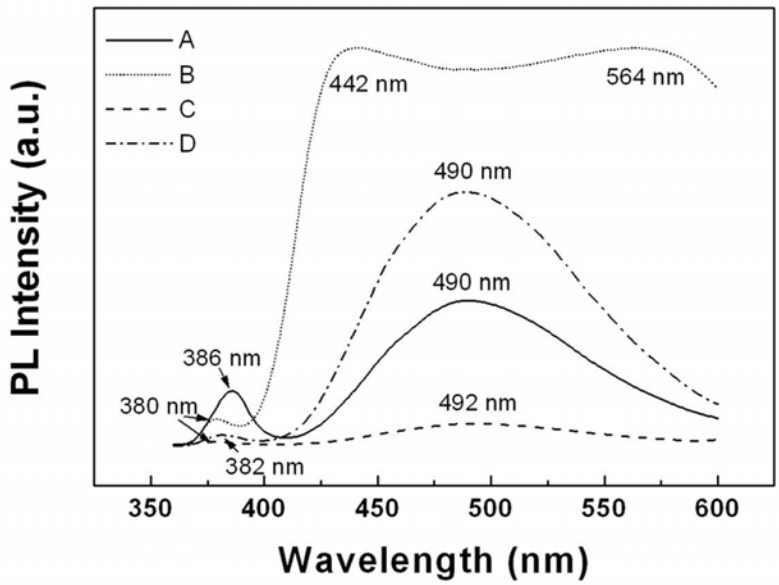

Figure 2.8 Photoluminescence of ZnO nanocrystals synthesized under different conditions. (A: ZnO nanotetrapods; B: ZnO nanowires; C: Zn nanowires; D: ZnO nanowires + nanoneedles after oxidation of Zn nanowires)

It can be observed from Figure 2.8 that the ratio of the UV to visible emission was clearly dependent on the fabrication conditions. It was reported that the ratio of the UV to visible

emission (such as green emission) is dependent on the nanostructure size [42]. However, no clear conclusions on the effect of the size on the ratio of UV intensity to visible emission can be made from our results. Therefore, it is likely that other factors would play an important role in the obtained PL results. Based on the present results, we have found that the intensity of the UV band increased with $R_{O:Zn}$; while for the visible emission, its intensity decreased with increasing $R_{O:Zn}$. This is consistent with the PL results by Wu *et al*. on ZnO films [58].

Table 2.1 Effect of N_2 flow rate on growth, structure, composition and PL spectra of ZnO nanocrystals

Flew rate (sccm)	Distance from source (mm)	Growth temperature (^oC) and mechanism	Products	$R_{O:Zn}$	Size (nm)	PL (wavelength) (nm)
70	88-106	950-980, VS	ZnO tetrapods	0.9	80-200	490
90	120-130	780-850, VLS	ZnO wires	0.78	60-120	442, 564
≥150	250-275	Room temperature, VS	Zn wires and needles		200-250	492
Oxidation of Zn nanowires		800, VLS	ZnO wires and needles	0.85	8-20 (needle)	490

As can be seen from Table 2.1, present study indicated that N_2 flow rate, during vapor phase deposition *via* carbothermal reduction process, can significantly affect the morphology, composition and optical properties of synthesized nanocrystals. Different from direct evaporation of pure Zn to produce Zn vapor [49], the amount of Zn vapor generated by the reaction of $2ZnO\ (s) + 2C\ (s) + O_2\ (v) \rightarrow 2Zn\ (v) + 2CO_2\ (v)$ can be reduced when increasing the N_2 flow rate. Therefore, a high flow rate, which yielded a low oxygen partial pressure and low supersaturation of Zn vapor, carried Zn vapor to a relative low temperature region, which favors 1-D ZnO nanowires growth with low $R_{O:Zn}$ [59], probably by 'self-catalyst' VLS growth mechanism [60], since no catalyst was used in the present study. On the contrary, a higher super saturation of Zn vapor and oxygen lead to the formation of ZnO nanotetrapods with high $R_{O:Zn}$ when N_2 flow rate

was reduced. Since the growth temperature of tetrapods (950-980^{o}C) was higher than the boiling point of Zn, the growth of tetrapods was considered to be *via* the vapor-solid (VS) mechanism.

In summary, we have shown that N_2 flow rate can significantly affect the morphology, composition and PL spectra of ZnO nanostructure synthesized by carbothermal reduction-vapor transport-condensation process. ZnO nanotetrapods were formed under low N_2 flows rate (70 sccm). A 'seed'-twinning mechanism has been proposed to explain the growth of ZnO nanotetrapod. ZnO nanowires (some of them are nanobelts) were deposited as increasing N_2 flows rate to 90-100 sccm. Zn nanowires were eventually formed as N_2 flow rate was increased to more than 150 sccm. Further oxidation of as-grown Zn nanowires resulted in the growth of ultra-fine ZnO nanoneedles out of Zn nanowires. Besides the UV band at 380-386 nm, ZnO nanotetrapods and ZnO nanowires + nanoneedles (oxidized Zn nanowires) showed a green emission at 490 nm, whereas ZnO nanowires demonstrated a much stronger blue light emission at 442 nm and a yellow emission at 564 nm.

2.3 INTRODUCTION TO ATOMIC FORCE MICROSCOPY

The atomic force microscopy (AFM), or scanning force microscopy (SFM) was invented in 1986 by Binning, Quate and Gerber. Like other scanning probe microscopy[61, 62] (SPM), the AFM utilizes a sharp probe moving over the surface of a sample in a raster scan. In the case of the AFM, the probe is a tip on the end of a cantilever, which bends in response to the force between the tip and the sample. The first AFM used a scanning tunneling microscopy at the end of the cantilever to detect the bending of the lever, but now most AFMs employ an optical lever technique. The diagram (Figure 2.9) illustrates how this works; as the cantilever flexes, the light

from the laser is reflected onto the photosensitive detector (PSD). By measuring the difference signal at PSD, changes in the bending of the cantilever can be measured. Since the cantilever obeys Hooker's Law for small displacements, the interaction force between the tip and the sample can be found. The movement of the tip or sample is performed by an extremely precise positioning device made from piezo-electric ceramics, most often in the form of a tube scanner. The scanner is capable of sub-angstrom resolution in x-, y- and z-directions. The z-axis is conventionally perpendicular to the sample.

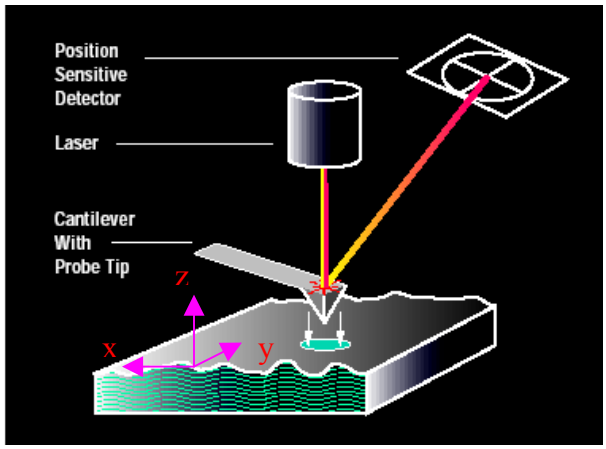

Figure 2.9 Schematic of an atomic force microscopy

2.3.1 Feedback operation

The AFM can be operated in two principal ways

- With feedback control
- Without feedback control

If the electronic feedback is switched on, then the positioning piezo that is moving the sample (or tip) up and down can respond to any changes in force that are detected, and alter the tip-sample separation to restore the force to a pre-determined value. This mode of operation is

known as *constant force*, and usually enables a fairly faithful topographical image to be obtained (hence the alternative name, *height mode*).

If the feedback electronics are switched off, then the microscope is said to be operating in *constant height* or *deflection* mode. This is particularly useful for imaging very flat samples at high resolution. Often it is best to have a small amount of feedback-loop gain, to avoid problems with thermal drift or the possibility of a rough sample damaging the tip and/or cantilever. Strictly, this should then be called *error signal* mode.

The error signal mode may also be displayed whilst feedback is switched on; this image will remove slow variations in topography but highlight the edges of features.

2.3.2 Operation mode

The way in which image contrast is obtained can be achieved in many ways. The three main classes of interaction are *contact mode*, *tapping mode* and *non-contact mode*.

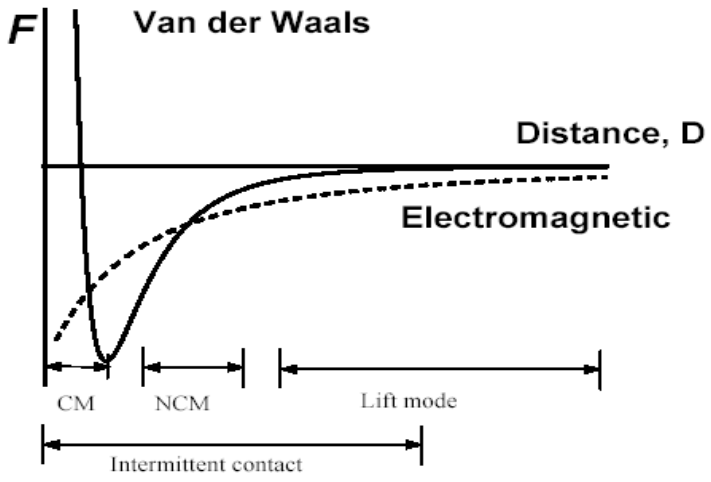

Figure 2.10 Distance dependence of Van Der Waals and electrostatic forces compared to the typical tip-surface separations in the contact mode (CM), non-contact mode (NCM), intermittent contact (or tapping) mode and lift mode. In the last case, the tip cannot acquire the topographic information and additional scan is necessary to position the tip at required separation from the surface.

Contact mode is the most common method of operation of the AFM. As the name suggests, the tip and sample remain in close contact as the scanning proceeds. By "contact" we mean in the repulsive regime of the inter-molecular force curve (see Figure 2.10). The repulsive region of the curve lies above the x-axis. One of the drawbacks of remaining in contact with the sample is that there exist large lateral forces on the sample as the tip is "dragged" over the specimen. **Tapping mode** (or Intermittent contact) is the next most common mode used in AFM. When operated in air or other gases, the cantilever is oscillated at its resonant frequency (often hundreds of kilohertz) and positioned above the surface so that it only taps the surface for a very small fraction of its oscillation period. This is still contact with the sample in the sense defined earlier, but the very short time over which this contact occurs means that lateral forces are dramatically reduced as the tip scans over the surface. When imaging poorly immobilized or soft samples, tapping mode may be a far better choice than contact mode for imaging. Other (more interesting) methods of obtaining image contrast are also possible with tapping mode. In constant force mode, the feedback loop adjusts so that the amplitude of the cantilever oscillation remains (nearly) constant. An image can be formed from this amplitude signal, as there will be small variations in this oscillation amplitude due to the control electronics not responding instantaneously to changes on the specimen surface.

More recently, there has been much interest in **phase** imaging. This works by measuring the phase difference between the oscillations of the cantilever driving piezo and the detected oscillations. It is thought that image contrast is derived from image properties such as stiffness and viscoelasticiy. Digital Instruments has an application note on this topic.

Non-contact operation is another method, which may be employed when imaging by AFM. The cantilever must be oscillated above the surface of the sample at such a distance that we are no longer in the repulsive regime of the inter-molecular force curve. This is a very difficult mode to operate in ambient conditions with the AFM. The thin layer of water contamination, which exists on the surface on the sample, will invariably form a small capillary bridge between the tip and the sample and cause the tip to "jump-to-contact". Even under liquids and in vacuum, jump-to-contact is extremely likely, and imaging is most probably occurring using tapping mode.

Lift mode

Several techniques in AFM rely on removing topographical information from some other signal. Magnetic force imaging and Electrostatic force imaging work by first determining the topography along a scan line, and then lifting a pre-determined distance above the surface to re-trace the line following the contour of the surface. In this way, the tip-sample distance should be unaffected by topography, and an image can be built up by recording changes which occur due to longer range force interactions, such as magnetic forces.

Lateral Force Microscopy

The earlier discussion of the way in which the bending of the cantilever is detected considered the use of a laser and a split photo-diode. Lateral force microscopy (LFM) uses a 4-segment (or quadrant) photo-diode to enable measurement of the torsion of the cantilever as well. As the cantilever is scanned over the specimen surface (with the cantilever now scanning with its long axis perpendicular to the fast scan direction), variations in friction between the tip and sample will cause the tip to slick / slip during its scan, resulting in twisting of the cantilever.

Chemical Force Microscopy [63] combines LFM with treatments to the tip to customize its interaction with the sample.

2.3.3 Tip effects

One of the most important factors influencing the resolution, which may be achieved with an AFM, is the sharpness of the scanning tip. The first tips used by the inventors of the AFM were made by gluing diamond onto pieces of aluminum foil. Commercially fabricated probes are now universally used. The best tips may have a radius of curvature of only around 2nm. The need for sharp tips is normally explained in terms of *tip convolution*. This term is often used (slightly incorrectly) to group together any influence that the tip has on the image. The main influences are

- Broadening
- Compression
- Interaction forces
- Aspect ratio

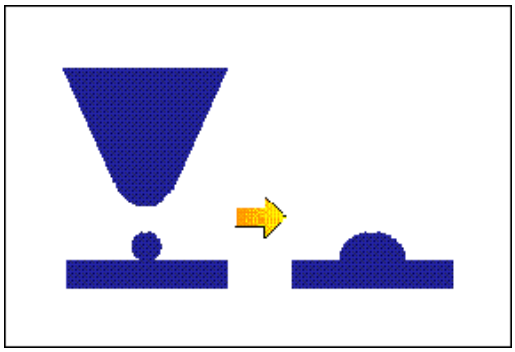

Figure 2.11 Tip broadening effect

Tip broadening arises when the radius of curvature of the tip is comparable with, or greater than, the size of the feature trying to be imaged. The diagram (Figure 2.11) illustrates this problem. As the tip scans over the specimen, the sides of the tip make contact before the apex, and the microscope begins to respond to the feature. This is what we may call tip convolution.

Compression occurs when the tip is over the feature trying to be imaged. It is difficult to determine in many cases how important this effect is, but studies on some soft biological polymers (such as DNA) have shown the apparent DNA width to be a function of imaging force. It should be born in mind that although the force between the tip and sample may only be from nN to μN, the *pressure* might be MPa to GPa. Interaction forces between the tip and sample are the reason for image contrast with the AFM. However, some changes that may be perceived as being topographical may be due to a change in force interaction. Forces due to the chemical nature of the tip are probably most important here, and selection of a particular tip for its material can be important. Chemical mapping using specially treated or modified tips is another important aspect of current research in AFM.

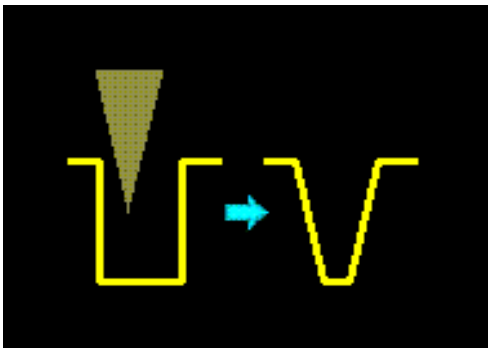

Figure 2.12 Tip aspect ratio effect

The aspect ratio (or cone angle) of a particular tip is crucial when imaging steep sloped features (Figure 2.12). Electron beam deposited tips have been used to image steep-walled features far more faithfully than can be achieved with the common pyramidal tips.

2.3.4 Force curve measurement

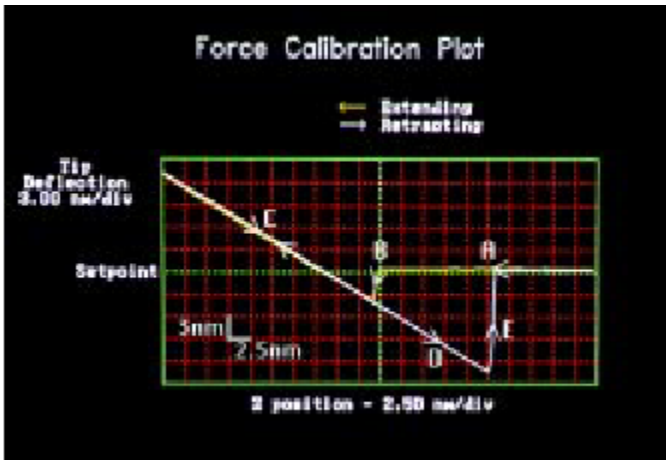

Figure 2.13 A typical AFM force curve

In addition to these topographic measurements, the AFM can also provide much more information. The AFM can also record the amount of force felt by the cantilever as the probe tip is brought close to — and even indented into — a sample surface and then pulled away. This technique can be used to measure the long range attractive or repulsive forces between the probe tip and the sample surface, elucidating local chemical and mechanical properties like adhesion and elasticity, and even thickness of adsorbed molecular layers or bond rupture lengths.

Figure 2.13 is a typical AFM force curve generated by Nanoscope III AFM system Force measurements are made by recording the deflection of the free end of the cantilever as the fixed end of the cantilever is extended towards and retracted from the sample [64]. As shown in Figure 2.13, the cantilever starts (point A) not touching the surface. In this region, if the cantilever feels a long-range attractive (or repulsive) force it will deflect downwards (or upwards) before making contact with the surface. In the case shown, there is minimal long-range force, so this "non-contact" part of the force curve shows no deflection. As the probe tip is

brought very close to the surface, it may jump into contact (point B) if it feels sufficient attractive force from the sample. Once the tip is in contact with the surface, cantilever deflection will increase (point C) as the fixed end of the cantilever is brought closer to the sample. If the cantilever is sufficiently stiff, the probe tip may indent into the surface at this point. In this case, the slope or shape of the contact part of the force curve (section C) can provide information about the elasticity of the sample surface. After loading the cantilever to a desired force value, the process is reversed. As the cantilever is withdrawn, adhesion or bonds formed during contact with the surface may cause the cantilever to adhere to the sample (section D) some distance past the initial contact point on the approach curve (point B). A key measurement of the AFM force curve is the point (E) at which the adhesion is broken and the cantilever comes free from the surface. This can be used to measure the rupture force required to break the bond or adhesion as shown in Figure 2.14.

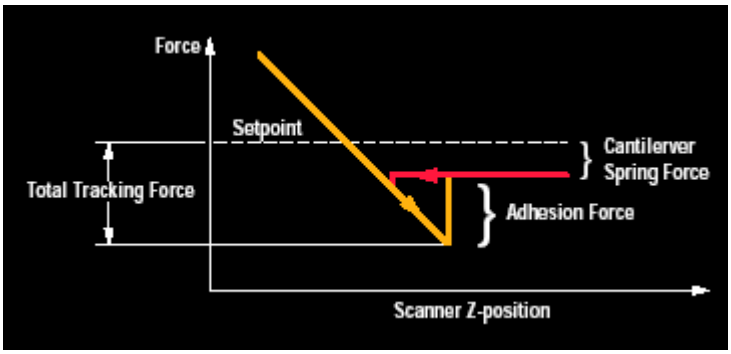

Figure 2.14 Schematic of AFM force measurement

The force sensed by the AFM probe is calculated by multiplying the deflection of the cantilever by the cantilever's spring constant. The spring constant of an end-loaded cantilevered beam of rectangular cross section is given by

$$k = \frac{Et^3 w}{4l^3} \qquad (2.1)$$

Where E is the elastic modulus, t is the thickness, w is the width, and l is the length. Because cantilever spring constants can vary from cantilever to cantilever, several methods have been developed to measure or calculate the cantilever spring constant. A typical indentation cantilever is shown in Figure 2.15. The cantilever is made of stainless steel with spring constant normally ranges from 100-200 N/m. A diamond tip mounted to the end of the cantilever has a tip radius less than 25nm.

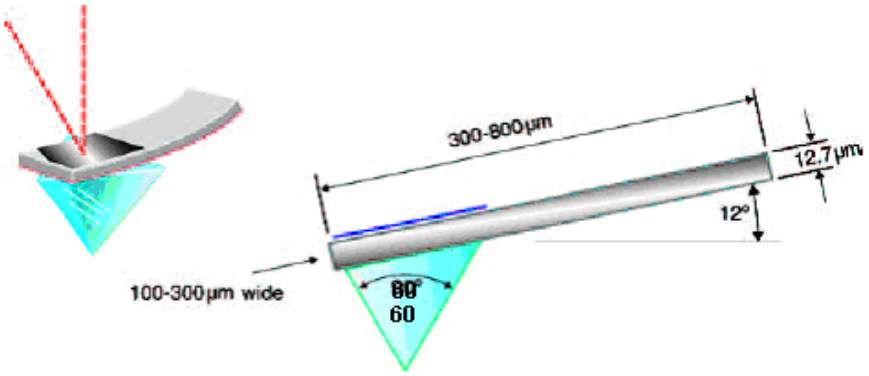

Figure 2.15 Geometry of a typical cantilever indenter

2.3.5 AFM vs. SEM

To conclude this section, it is beneficial to compare between AFM and SEM, which are powerful tools for surface analysis. As shown in table 2.2, the main advantage of AFM lies in its versatile operational environment, 3 dimensional image and local mechanical properties measurement, while lack of the SEM capability for constitutional and structural analysis. So the two techniques are complementary and it is better to combine them together.

Table 2.2 Comparison between SEM and AFM

	SEM	AFM
Sample operating environment	Vacuum	Ambient, air, liquid or vacuum
Depth of field	Large	Medium
Depth of focus	Large	Small
Resolution: X, Y	1-5 nm	2-10 nm dependent on tip
Resolution: Z	N/A	0.05nm
Effective magnification	$10\text{-}10^6$	$500\text{-}10^8$
Constitutional analysis	EDS	N/A
Structural analysis	XRD	N/A
Mechanical analysis	N/A	Local elasticity and plasticity
Characteristics required for sample	Surface must not build up charge and must be vacuum compatible	Sample must not have local variations in surface height >5-10 μm

2.4 INTRODUCTION TO HYSITRON TRIBOSCOPE NANOINDENTER

Although cantilever-typed AFM is capable of nanoindentations, there are still several reasons to employ a fixed probe nanoindenter. First, as there are 12° tilting angle for cantilever indenter (Figure 2.15), the indentation is not totally perpendicular to the sample surface. While for the fixed probe nanoindenter, the diamond probe is normal to the sample surface. Second, the maximum force for AFM cantilever indenter is normally below 100μN, while it is at least 10mN for a fixed probe nanoindenter.

In this study, we also use the Hysitron TriboScope® nanomechanical test instrument, which utilizes an *in-situ* imaging capability to realize the benefits of SPM imaging and nanoindentation in a single system. *In-situ* imaging allows the indenter probe to be positioned within ten-nanometers of any desired feature or phase of a material. After the test is performed, an image of the deformation caused by the test can be obtained immediately by using the

indenter tip to scan the surface. This eliminates the need to reposition an imaging instrument over the testing site. The force and displacement results that are acquired during the test, in conjunction with the *in-situ* image, offer an unparalleled wealth of information concerning the mechanical properties of the material.

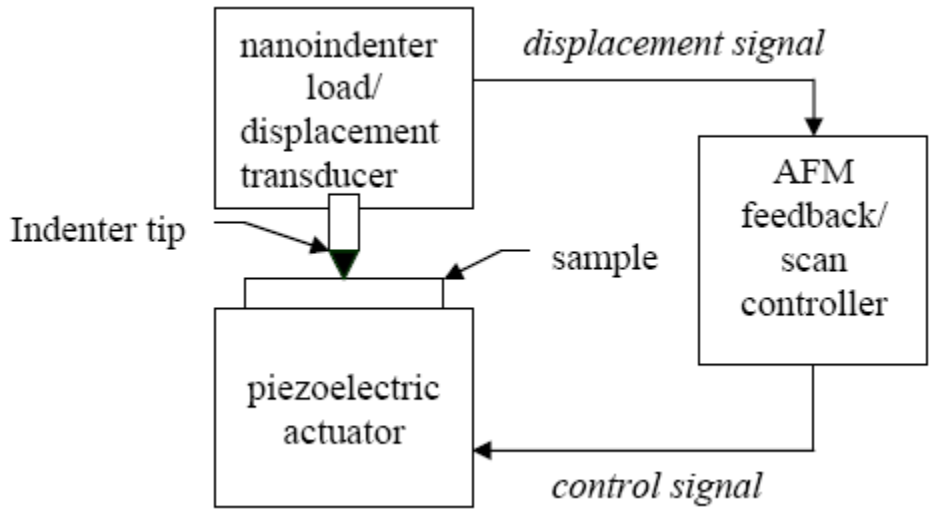

Figure 2.16 Schematic of a fixed probe nanoindenter with in-situ imaging capability

Figure 2.16 is a schematic of the working principle for Hysitron nanoindenter. The design of the Hysitron transducer allows it to be fitted to any commercially available SPM via a simple temporary modification. This involves a replacement of the normal detector head with the Hysitron transducer, in which the transducer then serves the function of sensing the surface and providing topographic feedback for imaging. However, the TriboScope®/SPM system is also then capable of quantitative nanomechanical testing. The indenter utilizes a rigid probe that makes the quantification of the force and displacement measurements more reliable than a measurement made with a probe on the end of a cantilever, which introduces many uncertainties.

3.0 NANOMECHANICAL PROPERTIES OF ZNO NANOBELT

3.1 INTRODUCTION

With a well-defined geometry, perfect crystallinity and chemical stability, the ZnO nanobelts are likely to be a model materials family for understanding mechanical behavior at nano-scale almost absence of defects [38]. The dimension of the nanobelt as a mechanical cantilever potentially can be used as a mechanical resonator [65-67]. Due to its nanoscale dimension in thickness, the natural frequency (resonance) of the nanobelt as a resonator could be very high.

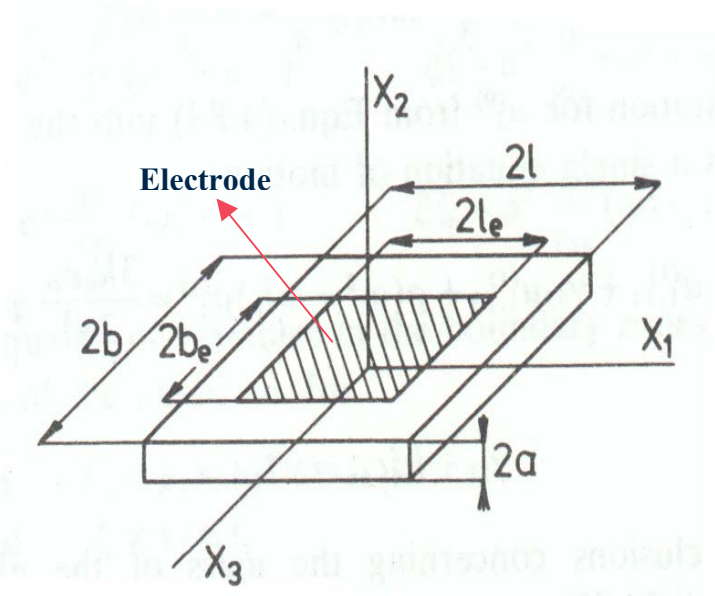

Figure 3.1 Modeling of a thin rectangular piezoelectric plate as a resonator

Figure 3.1 is a modeling of a thin rectangular piezoelectric plate with partial rectangular electrodes. The resonator based on a single nanobelt can be modeled like this. The resonant frequency of the plate is approximated as Eq. (3.1) [65]:

$$\omega_{1p}^2 = \frac{3K_{6P}^2 C_{66}}{\rho a^2} \qquad (3.1)$$

Where K_{6P} is the correction factors, C_{66} is the component of the elastic-stiffness tensor, ρ is the density, a is the thickness of the plate. For ZnO nanobelt, taking $K_{6P} \approx 1$, $C_{66} = 44.25$ GPa [68], $\rho = 5.665 \times 10^3 kg/m^3$, and thickness a=100nm, we get $\omega_{1P} \approx 7.7$ GHz. Hence, resonant frequency of the resonator based on an 100nm-thick ZnO nanobelt can reach GHz region. The thinner the belt is, the higher the resonant frequency can be. With the advance of telecommunication technology, GHz or higher resonator is a bottleneck yet to be solved. In this respect, ZnO nanobelt is a promising candidate for ultrahigh frequency resonator.

As ZnO nanobelt can potentially be used as a nanomechanical device, it is critical to study its mechanical properties such as elastic modulus, strength and fracture toughness. In the meantime, the freeing standing single crystalline ZnO nanobelt provides an ideal object for investigating the mechanical behavior of stress-free semiconducting oxides at nano-scale [69, 70]. In contrast, there are large residue stress existed in the thin film grown on the substrate owing to the incompatibility at the interface. So it is desirable to study nanomechanical properties of ZnO nanobelt. However, very little experimental data is available in this field [15, 38]. This is mainly due to the experimental difficulty in manipulating and testing the mechanical properties of a single nanobelt, for the nanoscale size of the object prohibits the applications of the well-established techniques, such as acoustic wave method for Young's modulus measurement, tensile test for strength. On the other hand, atomic force microscopy (AFM) and nanoindenter have been applied successfully in nanoscale mechanical study since 1990s [24-36, 71-73]. Most of these work are related to thin film, nano clusters or one dimensional carbon nanotubes, while characterization on quasi-one-dimensional nanostructures is much less

developed [37, 38, 74-76]. In particular, fixed probe nanoindenters with in-situ imaging capability are tailored for nanomechanical study, which is more suitable for study of nanomechanical properties of the quasi-one-dimensional nanostructures. The rectangular cross section of the naonbelt and atomically smooth surface are well suited for nanoindentation tests. Next part I will briefly explain how to extract nanomechanical properties from depth sensing nanoindentations using fixed sharp probe indenters.

3.2 DETERMINATION OF MECHANICAL PROPERTIES BY DEPTH SENSING NANOINDENTATIONS

3.2.1 Elastic modulus and hardness

Depth sensing nanoindentations [77-89], a continuous record of the variation of indentation depth, P, as a function of the depth of the penetration, h, into the indented specimen, have been used to extract mechanical properties such as elastic modulus and hardness since the method proposed by Oliver and Pharr in 1992 [87], which has its origins in an earlier treatment by Doerner and Nix [88]. Nowadays, both methods are accepted for the analysis of the indentation data by the ISO/FDIS 14577-1 standard [90].

If during the initial withdraw of the indenter, the material's recovery follows an elastic behavior and the contact area between the indenter and the specimen remains constant. Then for the case of the indentation of an elastic half-space by a cylindrical punch, the Sneddon's solutions [91] approach to the elastic behavior, which leads to a simple relation between the load, P, and the penetration depth, h, in the form of:

$$P = \frac{4\mu a}{1-\upsilon} h \qquad (3.2)$$

Where a is the radius of the cylinder; μ is the shear modulus; and υ is Poisson's ratio. Knowing that the area of the contact circle projected onto the surface, Ac, is equal to πa^2 and that the shear modulus is related to the elastic modulus in by:

$$E = 2\mu(1+\upsilon) \qquad (3.3)$$

Substituting (3.3) into (3.2) and differentiating the obtained expression with respect to h gives:

$$S = \frac{dP}{dh} = \frac{2}{\pi}\sqrt{A_c}\,\frac{E}{1-\upsilon^2} \qquad (3.4)$$

Where S is the contact stiffness and can be taken directly from the unloading slope at $h = h_{\max}$ (Figure 3.4). As the elastic modulus of the indenter is not infinite, Eq. (3.4) should be written in terms of reduced elastic modulus E_r, according to Hertz Equation:

$$\frac{1}{E_r} = \frac{1-\upsilon^2}{E} + \frac{1-\upsilon_i^2}{E_i} \qquad (3.5)$$

Where E, E_i, υ and υ_i are the elastic moduli and Poison's ratios of the specimen and indenter, respectively. For diamond, $E_i = 1141\,GPa, and\ \nu_i = 0.07$. For the indentation of a plane surface of a semi-infinite elastic solid by a rigid punch, Eq. (3.4) can be written as:

$$E_r = \frac{\sqrt{\pi}}{2}\frac{S}{\sqrt{A_C}} \qquad (3.6)$$

Eq. (3.6) shows that, for axisymmetric indenters, the relationship between unloading stiffness, S, and contact area, A_C, does not dependent on indenter geometry. That is to say, Eq. (3.6) is applicable to any axisymmetric indenters, not constrained to indenters with cylindrical shape. Using finite elements method, King [92] has introduced to Eq. (3.6) a correction factor (β) for non-axisymmetric indenters:

$$E_r = \beta \frac{\sqrt{\pi}}{2} \frac{S}{\sqrt{A_C}} \qquad (3.7)$$

A_C is the projected contact area at the maximum applied load. For geometrically perfect cube corner indenter, $A_C = 2.598 h_C^2$. However, the diamond indenter is not perfect and has some rounding at the apex, which must be taken into consideration if accurate results are to be obtained at shallow depth. To account for the tip radius effect, contact area is derived from the empirically determined area function such as Eq. (3.8) [93]. A series of nanoindentations of various sizes are made in a material with well-known isotropic elastic properties (usually fused quartz with $E_r = 69.6$GPa) by assuming the elastic modulus of the material is independent of depth.

$$Ac = C_0 h_C^2 + C_1 h_C + C_2 h_C^{1/2} + C_3 h_C^{1/4} + C_4 h_C^{1/8} + C_5 h_C^{1/16} \qquad (3.8)$$

Where h_C is the contact depth of indenter at the maximum applied load and C_0~C_5 are constants. Figures 3.2 to 3.4 show the main parameters used in analyzing indentation data [81]. The contact depth h_C (Figure 3.3) is determined by:

$$h_C = h_{\max} - h_S = h_{\max} - \varepsilon \frac{P_{\max}}{S} \qquad (3.9)$$

Where $\varepsilon \approx 0.75$ for pyramids indenters [94]. Hence hardness is given by:

$$H = \frac{P_{\max}}{A_C} \qquad (3.10)$$

With good experimental technique and careful analysis, the hardness and elastic modulus of many materials can be measured using these methods with accuracies of better than 10%. There are, however, some materials in which the methodology significantly overestimates *H* and *E*, specifically, materials in which a large amount of pile-up forms around the hardness impression.

The reason for the overestimation is that Eq. (3.7) and Eq. (3.9) are derived from a purely elastic contact solution that accounts for sink-in only. When pile-up is prevalent, the above methods for analyzing nanoindentation load-displacement data underestimate the true contact area. The parameter $h_f / h_{\max}$, which can be measured experimentally, is a useful indicator of when pile-up may be an important factor [83]. When $h_f / h_{\max}$ is less than 0.7 and materials are strongly work-harden, the above analysis procedures can give accurate results.

An important variation on the procedures just described is offered by a special measurement technique, continuous stiffness measurement (CSM), in which the contact stiffness, *S*, is measured continuously during the loading portion of the test. CSM [84] is accomplished by imposing a small, sinusoidally varying signal on the output which drives the motion of the indenter and analyzing the resulting response of the system by means of a frequency specific amplifier. This technique offers a direct measure of dynamic contact stiffness during the loading portion of an indentation test. Furthermore, it is somewhat insensitive to thermal drift, allowing more accurate observation of small volume deformation.

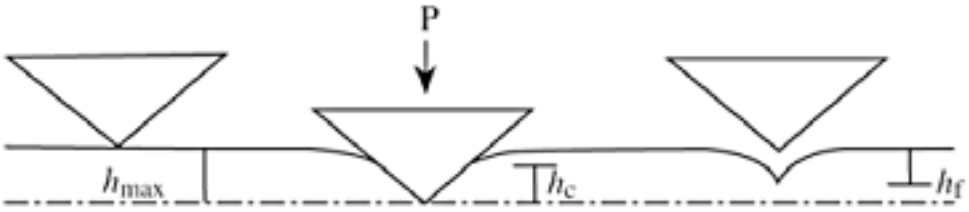

Figure 3.2 Profile of the surface before and after indentation

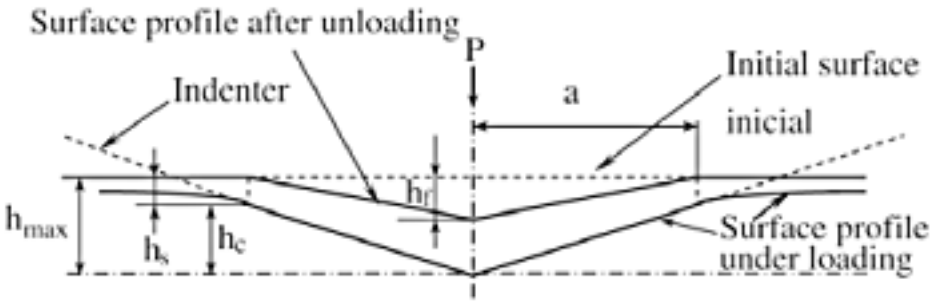

Figure 3.3 Main parameters used in analyzing unloading vs. indenter depth curve

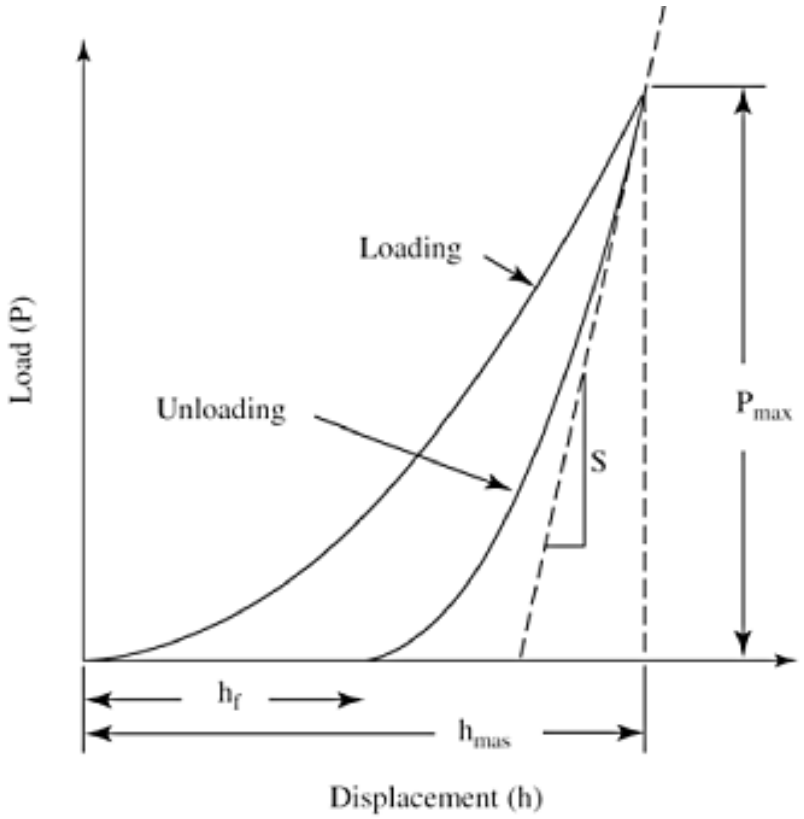

Figure 3.4 Schematic representation of load-displacement data for a depth sensing indentation experiment

3.2.2 Fracture toughness

Fracture toughness at small scales (micron or sub micron) can be measured by ultra-low load indentation using techniques similar to those developed for microindentation testing [95]. As shown schematically in Figure 3.5, these techniques make use of the radial cracking that occurs when brittle materials are indented by a sharp indenter. Lawn, Evans and Marshall [96] have shown that a simple relationship exists between the fracture toughness, T, and the lengths of the radial cracks, c, of the form:

$$T = \alpha(\frac{E}{H})^{1/2}(\frac{P}{c^{3/2}}) \qquad (3.11)$$

Here, P is the peak indentation load and α is an empirical constant which depends on the geometry of the indenter. For cube-corner indenter, the value of the geometric constant is $\alpha = 0.040$ [95]. E and H are elastic modulus and hardness, which can be determined directly from analyses of the nanoindentation load-displacement data. c is the post-indentation crack length from the center of the hardness impression. Hence, once crack length c is measured after the indentation, the derivation of the fracture toughness using this method is straightforward.

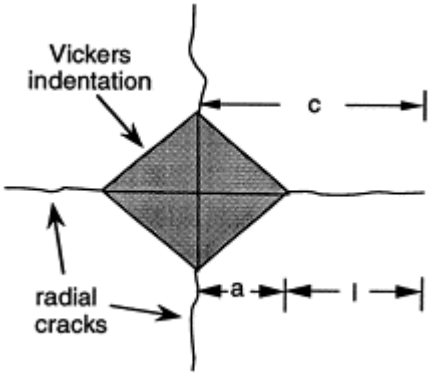

Figure 3.5 Schematic illustration of radial cracking at a Vickers indentation [95]

3.3 EXPERIMENTAL DESCRIPTION

The synthesis of nanobelts was based on thermal evaporation of oxide powders under controlled conditions without presence of catalyst [1]. After the preparing of the nanobelts, the procedures to get the single nanobelt for study are as follows. First immerse the wool like nanobelts in acetone. The mixture was dispersed by ultrasonic devices. Then dropped the mixed solution onto polished (100) p-type silicon wafer. After drying, single nanobelt is lying on silicon substrate.

3.3.1 Nanoindentations using Hysitron Triboscope Nanoindenter

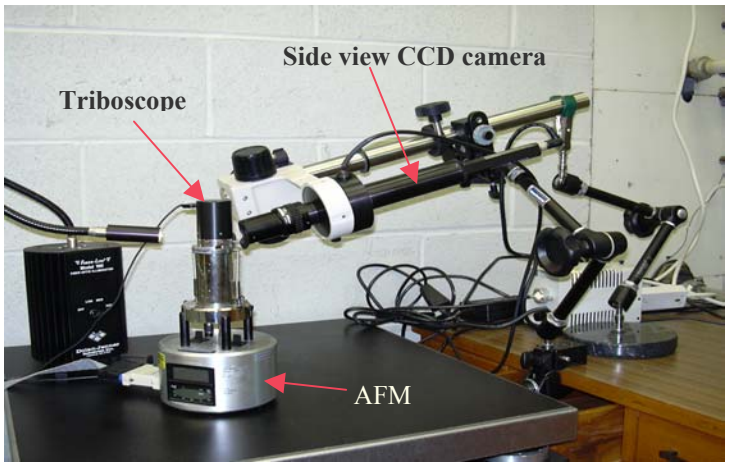

Figure 3.6 Experimental setup of nanoindentations using Hysitron Triboscope

The prepared nanobelt sample was investigated by Hysitron TriboScope® nanoindenter in conjunction with Digital Instruments' Nanoscope IIIa Multimode® AFM. The photo of the experimental setup was shown in Figure 3.6. A homemade side view CCD camera was added to optically locate the nanobelt lying on Si substrate (Figure 3.7). The magnification of which (450×) was much higher than the commercially available add-on CCD camera (~70×) for Triboscope. This is critical for the study of 1D nanostructures, for optical locating could save

huge amount of time in locating 1D nanostructures compared to scanning the surface with indenter tip. Cube corner diamond indenter (three-sided pyramid with 90° included angle) was used to image a ZnO nanobelt and then in situ indent the nanobelt with the same tip.

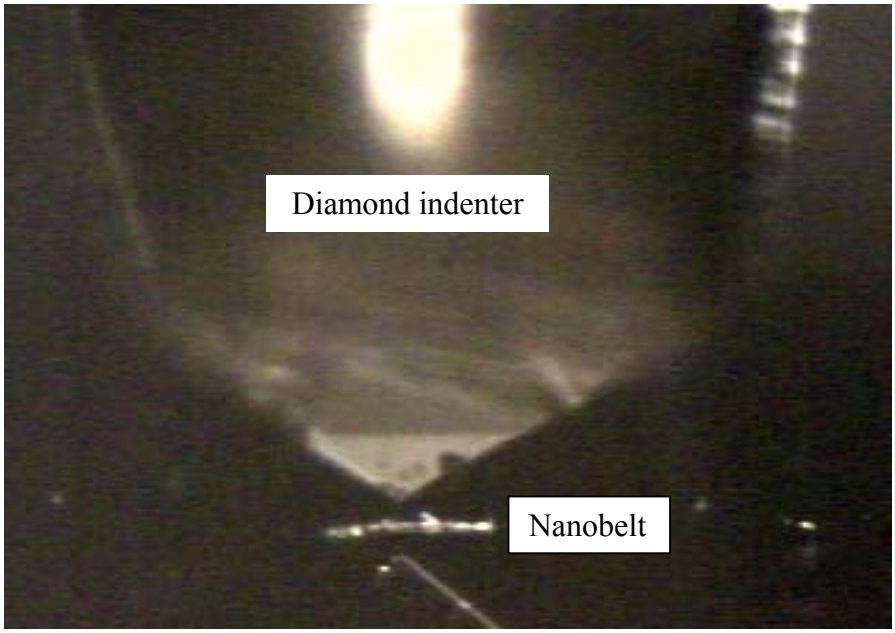

Figure 3.7 Side view of diamond indenter and nanobelt

The loading and unloading rate was kept constant at 10μN/s. After nanoindentations, the indentation impression was imaged with the same tip, which verifies that the test was performed in the anticipated location as shown in Figure 3.8a. The thickness of the investigated ZnO nanobelt derived from Figure 3.8b was 252nm, which restrained the nanoindentation depth below 80nm, as it was generally accepted that the depth of indentation should never exceed 30% of the wire diameter or film thickness [97]. Nanoscale mechanical properties, such as elastic modulus, hardness and fracture toughness of individual zinc oxide nanobelts were characterized by Nanoscope IIIa AFM and Hysitron TriboScope nanoindenter with homemade side view CCD camera.

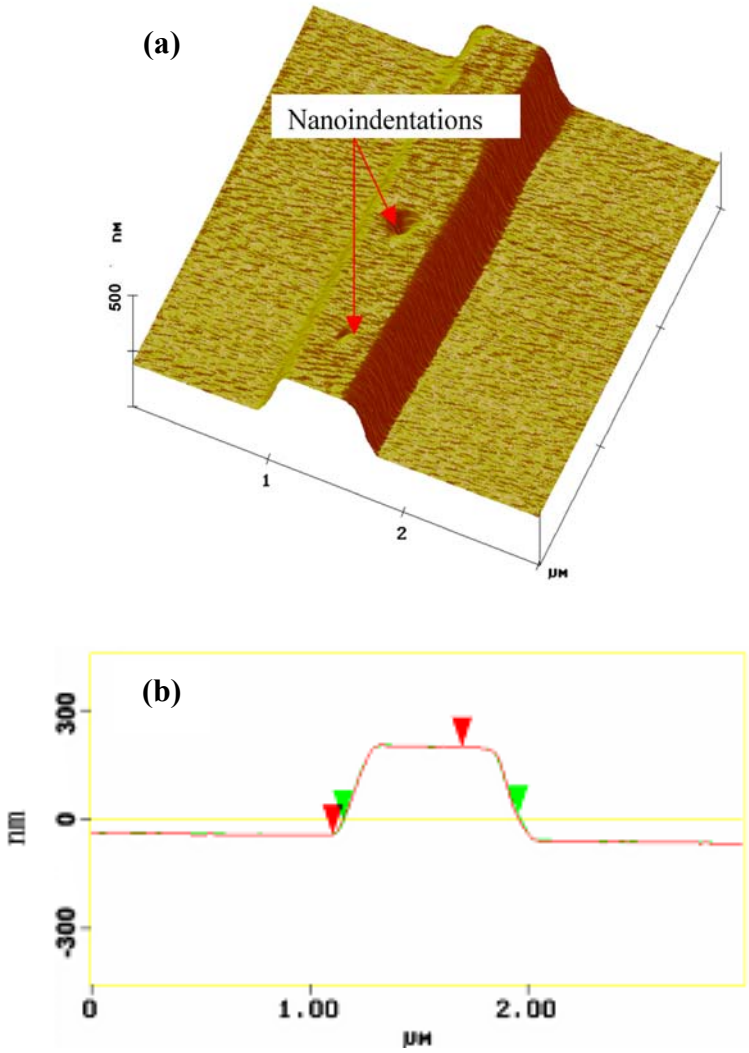

Figure 3.8 AFM image of nanoindentations on the nanobelt (a) 3D images: the large indent was produced by 150 μN load and the smaller one was produced by 100μN load. (b) Section analysis showing the geometry of the nanobelt. Note only the thickness value is correct. The width shown here is larger than the actual value due to the tip broadening effect.

3.3.2 Nanoindentations using AFM cantilever indenter

Nanoindentations on ZnO nanobelt was also performed with Nanoscope IIIa Multimode AFM by using stainless steel cantilever with a diamond tip. The spring constant of the cantilever was calibrated by Veeco Instruments to be 170.2 N/m. The diamond tip, a three sided pyramid with an apex angle of 60 degrees and a nominal tip radius of 25nm, was mounted to the end of the cantilever in a way that the vertical axis of the pyramid was approximately normal to the sample surface. Before nanoindentation, the nanobelt was located by the diamond tip under tapping mode. Then the tip was positioned still to the center of the nanobelt. Indentation mode was used during nanoindentations on ZnO nanobelt. The peaking loading was set from 1μN to 34μN to get elastic, plastic and fractural deformation on the ZnO nanobelt. The loading and unloading rate was kept constant at 1Hz. Deflection versus z piezo movement curves were recorded and converted to force versus displacement curve using the procedure outlined in Appendix 1. The principle of the conversion is as follows. Multiplying the deflection signal (in unit of nm) by the spring constant of the cantilever (in unit of N/m) gives the force (in unit of nN). The sample displacement is the difference between Z piezo movement and cantilever deflection (in unit of nm). Calibration on the sapphire sample was done before and after the nanoindentations on the ZnO nanobelt.

Once force versus displacement curves were derived, similar analysis procedure as fixed probe indentations were done on the elastic modulus, hardness and fracture toughness of the ZnO nanobelt. Comparisons were made in the results by two methods.

3.4 ELASTIC BEHAVIORS

3.4.1 Elastic modulus by Triboscope nanoindenter

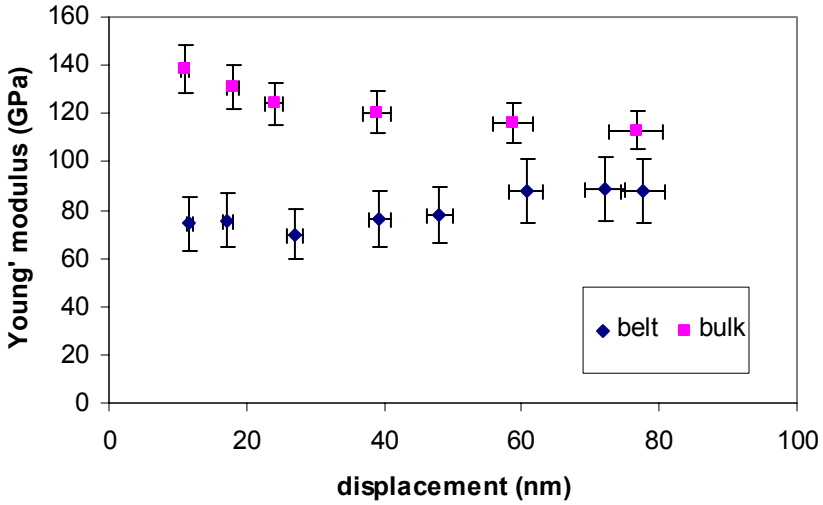

Figure 3.9 Comparison of Young's modulus between ZnO nanobelt and bulk by Triboscope indenter

Figure 3.9 compares Young's modulus derived by the Hystrion Triboscope nanoindenter using the aforementioned procedure. The measured reduced modulus is converted to Young's modulus using Eq. (3.5). Poison's ratio of ZnO is taken as 0.36 [98]. The most striking feature of Figure 3.9 is that Young's modulus of ZnO bulk is significantly larger than that of the nanobelt. A possible reason may be that in our experiments the surface properties dominate the elastic behavior. Surface effects such as dangling bonds, surface relaxation or reconstuction can alter the bonding behavior of the atoms in the surface region. In the case of nanobelt, there are much higher percent of surface atoms than the bulk taking consideration of the high surface to volume ratio in ZnO nanobelt (surface to volume ratio of nanobelt versus bulk is ~2500 to 1 with the

dimension of $250nm \times 500nm \times 50\mu m$ for nanobelt and $0.5mm \times 5mm \times 5mm$ for bulk). So it is reasonable to assume the measured Young's modulus by nanoindentation is lower than that of the bulk. The result is in good agreement with that derived from TEM resonance method, which ranges from 40-60GPa. Furthermore, nanoindentations on SnO_2 nanobelts give similar results. As shown in Figure 3.10, the elastic modulus of SnO_2 nanobelt is significantly smaller than the average elastic modulus in bulk form, which shows significant elastic anisotropy within the (100) crystal plane varying from 174.5 GPa to 340.1GPa [99]. Moreover, similar findings are reported in SnO_2 ultathin thin film [99], nanometer size supported gold clusters [100, 101], ultathin single crystalline silicon cantilevers [102] and atomic simulation of copper nanowire [103].

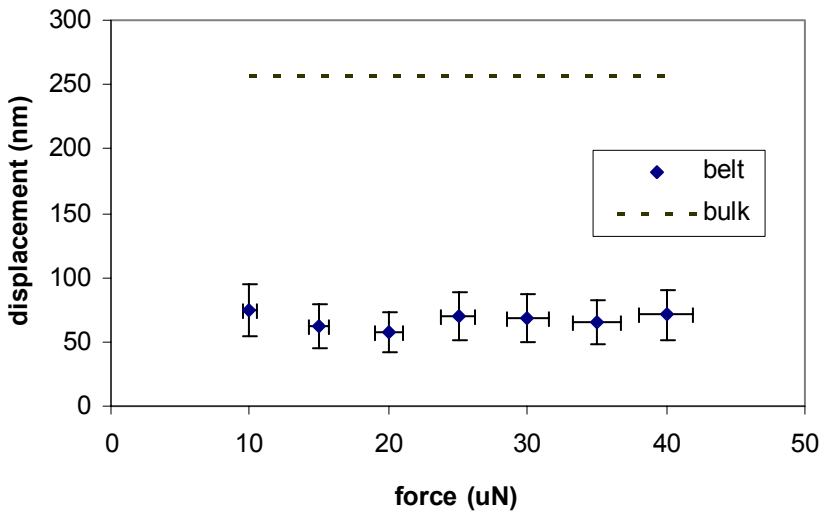

Figure 3.10 Comparison of Young's modulus between SnO_2 nanobelt and bulk by Triboscope indenter

3.4.2 Elastic modulus from AFM cantilever indenter

Figures 3.10 and 3.11 are typical deflection versus z piezo movement curves of ZnO nanobelt and ZnO bulk by AFM cantilever indenter. As the slope of both curves is almost linear, it is suggested that linear elastic model may apply to the analysis. The effective contact sensitivity of the indenter-sample system (in unit of nm/V); S_{eff}, can be derived from the initial unloading slope of the curve, which is 115.4nm/V and 109.0nm/V for nanobelt and bulk respectively. Then the effective contact stiffness of the indenter-sample system (k_{eff}) can be determined by $k_{eff} = k_{indenter} S_{indenter} / S_{eff}$. Taking $k_{indenter} = 170.2 N/m$, $S_{indenter} = 102$ nm/V (provided by Veeco Inc.), the effective contact stiffness of the samples are $k_{eff,belt} \approx 150.4 N/m$ and $k_{eff,bulk} \approx 159.3 N/m$. Modeling the sample and the cantilever indenter as two series connected springs (Figure 3.12) gives,

$$\frac{1}{k_{eff}} = \frac{1}{k_{sample}} + \frac{1}{k_{indenter}} \qquad (3.12)$$

We can estimate $k_{belt} \approx 1296 N/m$ and $k_{bulk} \approx 2480 N/m$. As the contact stiffness is proportional to the elastic modulus indicated by Eq. (3.7), the ratio of the elastic modulus between belt and bulk is equal to that of the contact stiffness. That is, $E_{belt} / E_{bulk} \approx k_{belt} / k_{bulk} \approx 1296 / 2480 \approx 0.523$, which is consistent with the results illustrated in Figure 3.9.

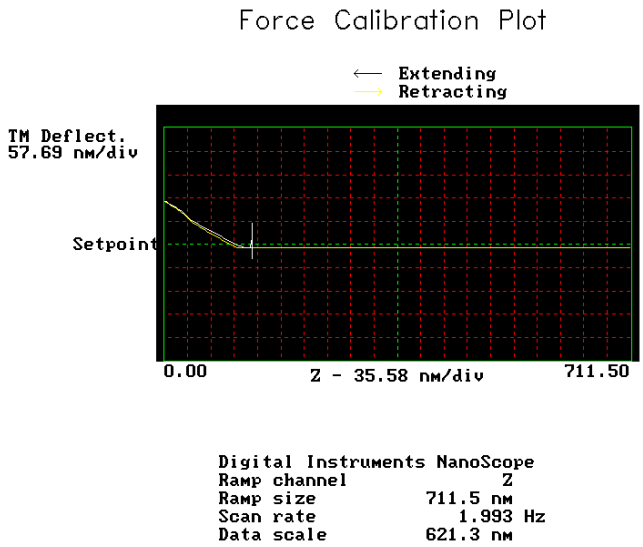

Figure 3.11 A typical deflection versus Z piezo movement curve of ZnO nanobelt by AFM cantilever indenter

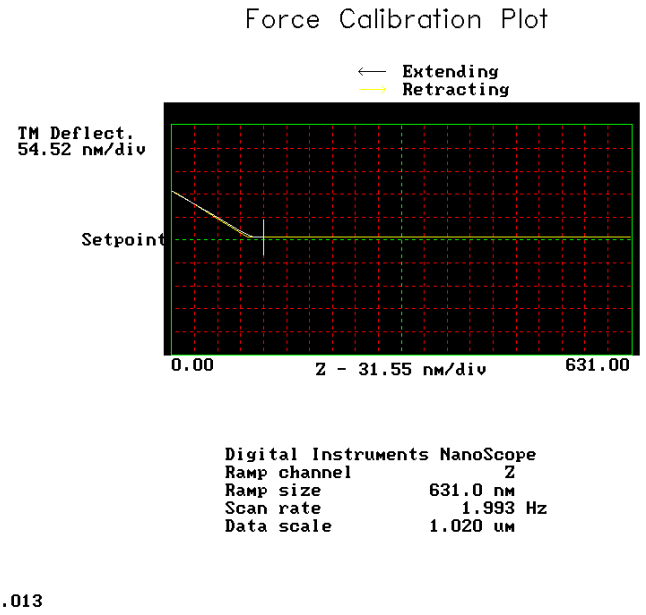

Figure 3.12 A typical deflection versus Z piezo movement curve of ZnO bulk by AFM cantilever indenter

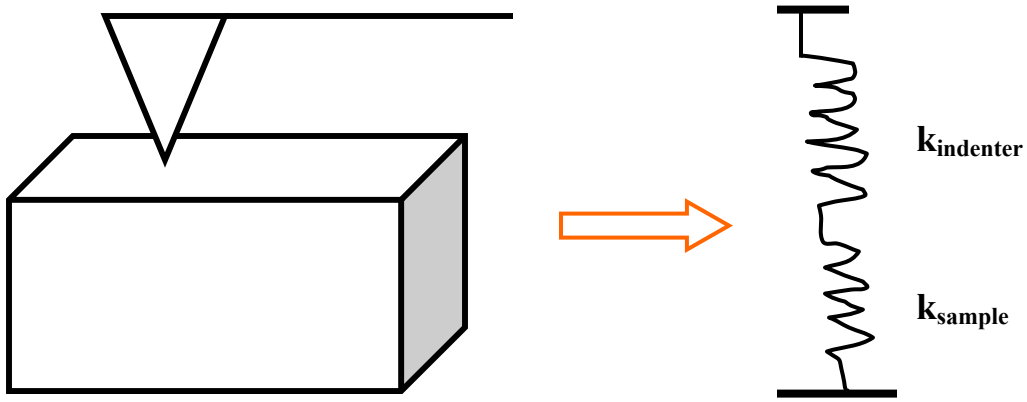

Figure 3.13 Modeling the AFM indenter-sample system as two series connected springs

3.5 PLASTIC BEHAVIORS

3.5.1 Pop in event near initial yield point

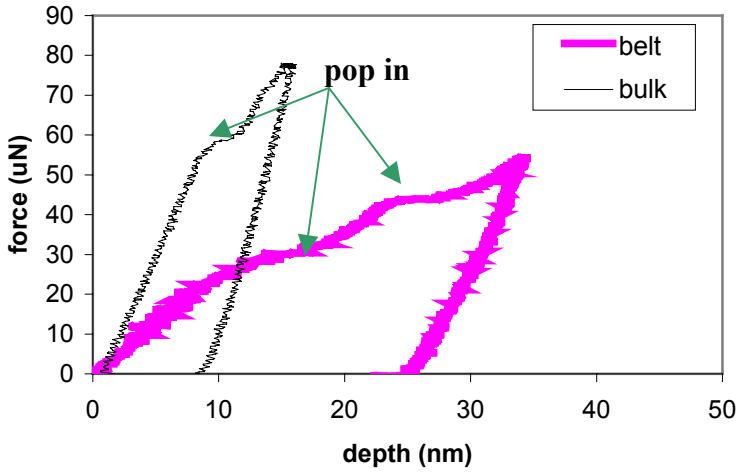

Figure 3.14 Typical force-displacement curves of ZnO nanobelt and bulk by Triboscope nanoindentations. Displacement excursions are distinct features in the loading portion of the curves.

The distinctive feature revealed in Figure 3.14 is the characteristic "pop in" event or displacement excursion during the loading part. The critical load for the first "pop in" event is about 65±10μN for (0001) ZnO bulk and 35±15μN for ZnO nanobelt. As proposed by previous studies [104-108], this critical load can be related to theoretical shear stress, which is regarded as the critical stress for the onset of the dislocation nucleation. It is interesting to estimate the magnitude of the critical stress, σ_C, for the onset of the pop in events. When the indentation depth, h, is within one third of the indenter radius, R, the contact area should be determined by spherical area function [109]. In this case, the indenter radius was determined to be 380nm

according to procedures outlined in Appendix A.2. Hence, the critical stress for the onset of pop in events was determined by Equations (3.13) and (3.14) using spherical area function.

$$\sigma_{C,belt} = \frac{F_{c,belt}}{\pi h_{c,belt}(2R - h_{c,belt})} = \frac{35\mu N}{\pi \times 15nm \times (2 \times 380nm - 15nm)} \approx 1.00(GPa) \quad (3.13)$$

$$\sigma_{C,bulk} = \frac{F_{c,bulk}}{\pi h_{c,bulk}(2R - h_{c,bulk})} = \frac{65\mu N}{\pi \times 8nm \times (2 \times 380nm - 8nm)} \approx 3.44(GPa) \quad (3.14)$$

As the theoretical shear stress is within $1/10 \sim 1/2\pi$ of the Young's modulus [110], the estimated critical stress for the onset of the pop-in events is much lower than the theoretical shear stress. Hence the first "pop in" event is not corresponding to the onset of the dislocation nucleation. A proper explanation might be the dislocation nucleation occurs at a stress level much lower than the theoretical shear stress. As the scale of a burger's vector is only a fraction of nanometer, a single or couples of dislocation activities are not detectable on the loading curve. The first "pop in" is observed when an avalanche of dislocations is produced.

3.5.2 Inverse pop-in and reverse thrust events

Besides the pop-in events near the initial yield point, we also observed inverse pop-in and reverse thrust events in some nanoindentation curves by AFM cantilever indenter. Although such events are not obvious in the original deflection versus z piezo movement curve (Figure 3.15), they are very clear in the converted load-displacement curve (Figure 3.16). The inverse pop-in event starts at the indentation depth of 11.85nm under 4.47 μN load and ends at the depth of 8.11nm under 5.73 μN load in the loading portion, while the reverse thrust event starts at the indentation depth of 8.11nm under 1.56μN load and ends at depth of 11.85nm under 0.25μN load. It is remarkable to notice that the displacement excursion for the two events is exactly the

same, which indicates that these two events must be related. This phenomenon can be accounted for in terms of phase transition in ZnO.

ZnO possesses a hexagonal wurtzite structure (B4) at normal condition of temperature and pressure. This phase transforms to the cubic rocksalt structure (B1) at a pressure in the vicinity of 9 GPa, resulting in an increase of coordination number, from 4 to 6, and a large volume decrease of about 18% [111-121]. The reverse transition ($B1 \rightarrow B4$) also exists but normally at lower pressure with hystersis of ~4GPa. Table 3.1 gives calculated and experimental lattice and internal parameters for ZnO.

Table 3.1 Calculated and experimental lattice and internal parameters for ZnO [111]

	Calculation	Experiment
Structure	Wurtzite	
Volume (A^3/f.u.)	23.62	23.796 [121]
c/a	1.59	1.602[121]
u	0.38	0.382[121]
Bulk modulus (GPa)	160	183[121] , 170 [122]
Structure	High pressure phase (NaCl)	
Volume (A^3/f.u.)	19.08	19.484[121]
Bulk modulus (GPa)	219	228[121]
Lattice constant (A) at 10GPa	4.19	4.211 [122]
Transition pressure (GPa)	8.0	2.0-8.7[121], 10.0[122]
Volume change, ΔV/V (%)	18.8	18.13[121], 18[122]

During nanoindentations on ZnO nanobelt by AFM indenter, ultrahigh pressure can build up under the indenter due to the sharp radius of the AFM tip. The critical stress at the onset of inverse pop-in and reverse thrust can be estimated using spherical area function. Tip radius, R, is estimated to be 18nm in the Appendix A.2.

$$\sigma_{C,inverse\ pop-in} = \frac{F_{C,i}}{\pi h_{C,i}(2R - h_{C,i})} = \frac{4.47\mu N}{\pi \times 11.85nm(2 \times 18nm - 11.85nm)} \approx 4.97(GPa) \qquad (3.15)$$

$$\sigma_{C,reverse\ thrust} = \frac{F_{C,r}}{\pi h_{C,r}(2R - h_{C,r})} = \frac{1.56\mu N}{\pi \times 8.11nm(2 \times 18nm - 8.11nm)} \approx 2.20(GPa) \quad (3.16)$$

The above estimated critical stress is mean stress below a spherical indenter. In the case of the pyramid indenter we used, the maximum stress under indenter may reach the critical pressure for the phase transition of B4 $\rightarrow$ B1. Moreover, the observed inverse pop-in event during loading is consistent with the volume reduction associated with the transition B4 $\rightarrow$ B1, while the reverse thrust event during unloading is in agreement with the volume increase associated with the transition B1 $\rightarrow$ B4. The reverse transition happens at a lower pressure is also consistent with other observations. Hence, it is very likely that the phase transition B4 $\rightarrow$ B1 is the origin of the inverse pop-in event in the loading part, while the reverse phase transition B1 $\rightarrow$ B4 can account for the reverse thrust event in the unloading part. Further experiment such as Raman spectroscopy is needed to confirm this hypothesis.

In addition, it is interesting to mention that reverse thrust event is also observed in the nanoindentation of SnO_2 nanobelt by Triboscope indenter. A typical "reverse thrust" event is shown in Figure 3.17 during unloading, which means SnO_2 nanobelt exhibited unusually large amounts of depth recovery in this stage. Similar phenomenon was observed in (001) silicon [82]. The reverse thrust is caused by the relaxation of densified material during unloading. In this experiment, load-displacement curve on (001) Si substrate was also shown on Figure 3.17 to rule out the possible transformation in the Si substrate. Previous study [123] on bulk SnO_2 indicated the pressures in excess of 150 kbar were required to form the orthorhombic phase from rutile phase. If a phase transformation between rutile and orthorhombic crystal structures happens during the unloading of indentation on SnO_2 nanobelt, such "reverse thrust" might happen.

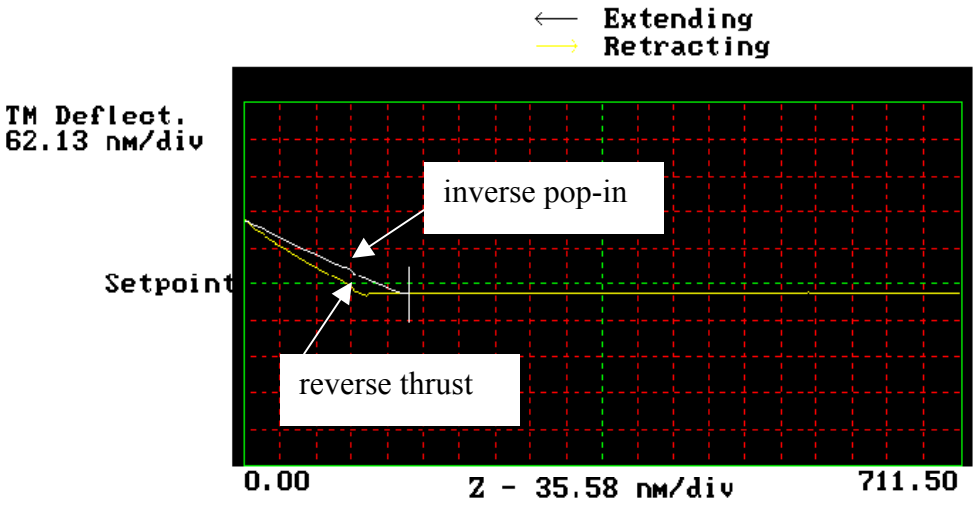

Figure 3.15 Deflection versus Z piezo movement curve of ZnO nanobelt with inverse pop-in and reverse thrust events by AFM cantilever indenter

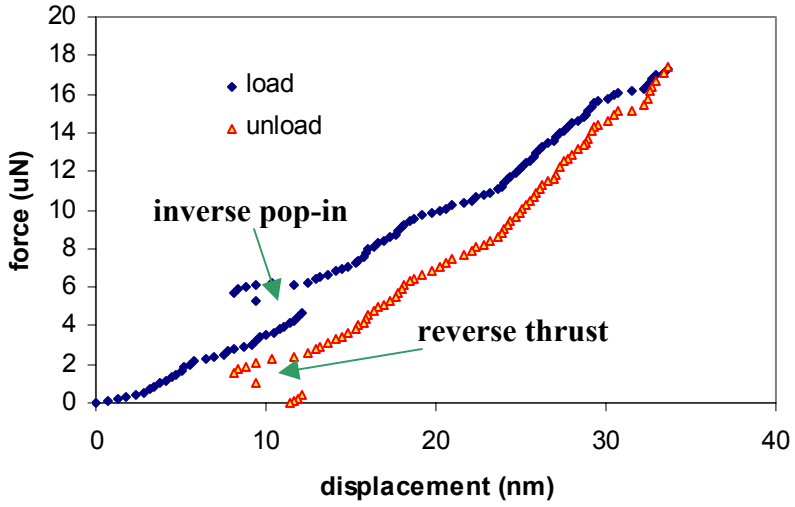

Figure 3.16 Force-displacement curve of ZnO nanobelt with inverse pop-in and reverse thrust events by AFM cantilever indenter

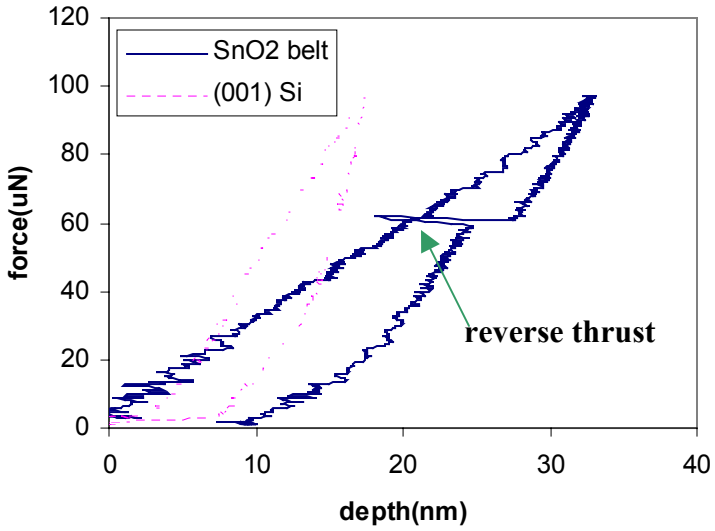

Figure 3.17 Force-displacement curve of SnO_2 nanobelt with reverse thrust event by Triboscope indenter. Nanoindentation curve on the Si substrate is also shown to confirm the observed phenomenon is not caused by the substrate or the instrument artifact.

3.5.3 Indentation size effect

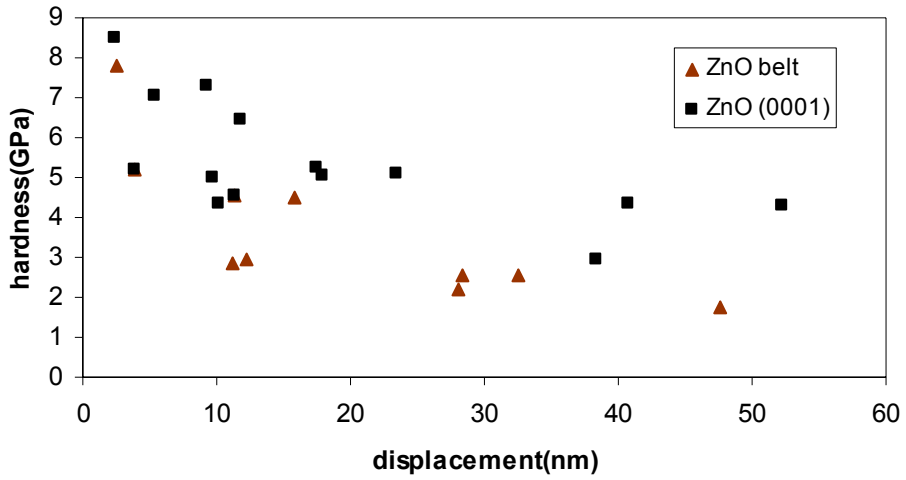

Figure 3.18 Comparison of hardness between ZnO nanobelt and bulk by Triboscope indenter

Comparison of ZnO nanobelt with ZnO bulk single crystal [124, 125] was carried out on (0001) plane by nanoindentations. As shown in Figure 3.18, the lower the penetration of the nanoindentation, the higher the hardness of the sample, which is attributed to indentation size effect (ISE) [126-130] due to the strain gradient for most materials. However, it is generally recognized that such strain gradient plasticity theories should not be used at very shallow depth in the vicinity of 100nm or less [128]. Recently, an alternative model [128] for indentation depths up to several hundred nanometers is proposed in terms of the surface to volume ratio $(S/V)_G$, where S is the projected contact area and V_G is the plastic volume under the contact. To understand how important the surface to volume ratio is, estimates of surface work and the volume work associated with plastic deformation under a contact are necessary.

Considering first the surface work. Using Maugis' terminology, the total work associated with creating either new area, dA, or new surface energy, dγ, can be written as

$$gdA=\gamma dA+Ad\gamma \qquad (3.17)$$

For a surface of N atoms with an area of $A=Na_o$ that the surface work is due to both elastically stretched bonds, da_o, and new numbers of atoms exposed, dN, giving

$$GdA=\gamma a_o dN+\sigma_s N da_o \qquad (3.18)$$

Where γ is surface energy and σ_s is the surface stress. With the definition of strain dA/A being both plastic, ε_p, and elastic, ε_E , it follows that

$$g = \gamma \frac{\varepsilon_P}{\varepsilon} + \sigma_s \frac{\varepsilon_E}{\varepsilon} \qquad (3.19)$$

Where ε is the total strain, Thus, the total surface work, Ws, is made up of new area associated with irreversible plastic work as well as elastically stretched bonds associated with reversible work. To first order, the total surface work can be given as the product of the contact area and surface energy.

$$W_s^{total} \approx \pi a^2 \gamma_s \qquad (3.20)$$

Next, consider the volume deformation associated with the plastic work, W_P. From a continuum standpoint W_P can be defined in terms of the plastic volume, V, and the tensile yield stress σ_{ys}, for an elastic-perfectly plastic material giving

$$W_P = \int_0^{\varepsilon_P} \sigma_{ys} d\varepsilon_P \qquad (3.21)$$

Defining an incremental strain as $d\varepsilon_p=d\delta/c$, where δ is the indentation depth and c is the plastic zone size described well by Johnson's cavity model,

$$c = [\frac{3P}{2\pi\sigma_f}]^{1/2} \tag{3.22}$$

Where P is the applied indentation load and σ_f is an appropriate flow stress. Noting that the hemispherical plastic volume would be $(2/3)\pi c^3$ and $\tau_{ys} \approx (2/3)\sigma_{ys}$ one sees that

$$W_p = V\int_0^\delta \frac{\sigma_{ys}}{c} d\delta = \frac{2}{3}\pi c^2 \sigma_{ys}\delta = \pi c^2 \tau_{ys}\delta \tag{3.23}$$

Using Eqs. (3.17) and (3.19), the surface to volume ratio is given by

$$\frac{W_S}{W_P} = \frac{\gamma_s}{\tau_{ys}\delta}(\frac{a}{c})^2 \tag{3.24}$$

Given that the a/c ratio is nearly constant at shallow penetration, this illustrates that the portion of surface work resisting penetration rapidly decreases with increasing depth of penetration as γ_s and τ_{ys} are constant.

If the contact area, πa^2, is coupled to a hemispherical volume of deforming materials, $(2/3)\pi c^3$, then a surface-to-volume ratio can be defined as

$$\frac{S}{V} = \frac{3a^2}{2c^3} \tag{3.25}$$

For plastic contacts of a spherical tip Johnson takes $a^2 \sim 2\delta R$ and combining this with the mean pressure defines hardness as

$$H \cong \frac{P}{\pi a^2} \cong \frac{P}{2\pi\delta R} \tag{3.26}$$

Using Eq. (3.22) to eliminate P, (3.26) becomes

$$H = \frac{\sigma_f}{(\frac{S}{V})^{2/3}} \cdot \frac{1}{(3\delta R)^{1/3}} \qquad (3.27)$$

For shallow depth of indentation the (S/V) is nearly independent of the depth. Hence the normalized hardness (H/σ_f) will decrease with larger indentation depth δ or indenter radius R, which not only address the ISE, but also the effect of tip radius. Figure 3.19 is the 17.5 μN indentation on ZnO nanobelt by AFM cantilever indenter. The force versus displacement curve (Figure 3.20b) is converted from the Figure 3.20a (Appendix A.1). The hardness is determined as 11.2 GPa at the indentation depth ~11nm using AFM indenter, while the hardness derived from Triboscope indenter is only 5-7 GPa at similar indentation depth. Taking consideration of the much sharper radius of the AFM indenter, the above results are reasonable according to Eq. (3.27). It is worth mention that Eq. (3.27) is applicable to more than the spherical tip indentation. For instance, pyramid tip should be treated as a spherical one when the indentation depth is below one third of the tip radius [109].

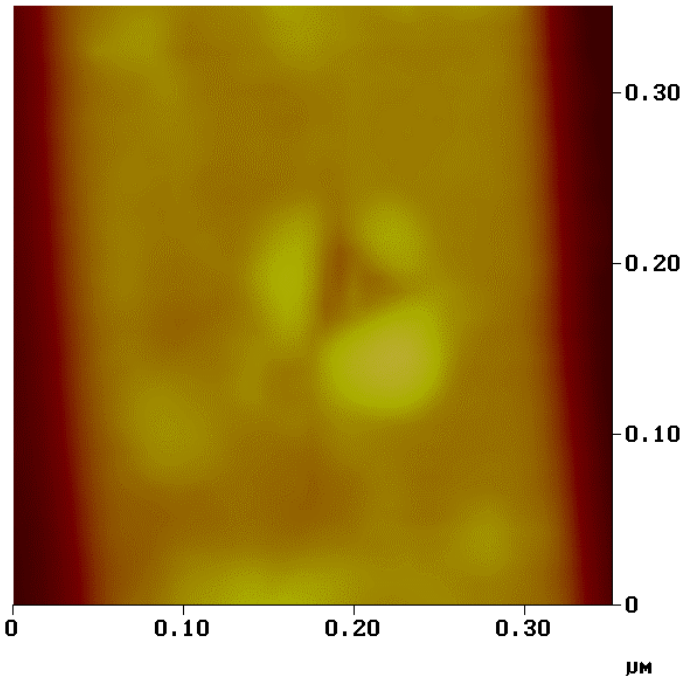

Figure 3.19 2D image of the nanoindentation on ZnO nanobelt by AFM cantilever indenter. (Peaking load: 17.5 μN)

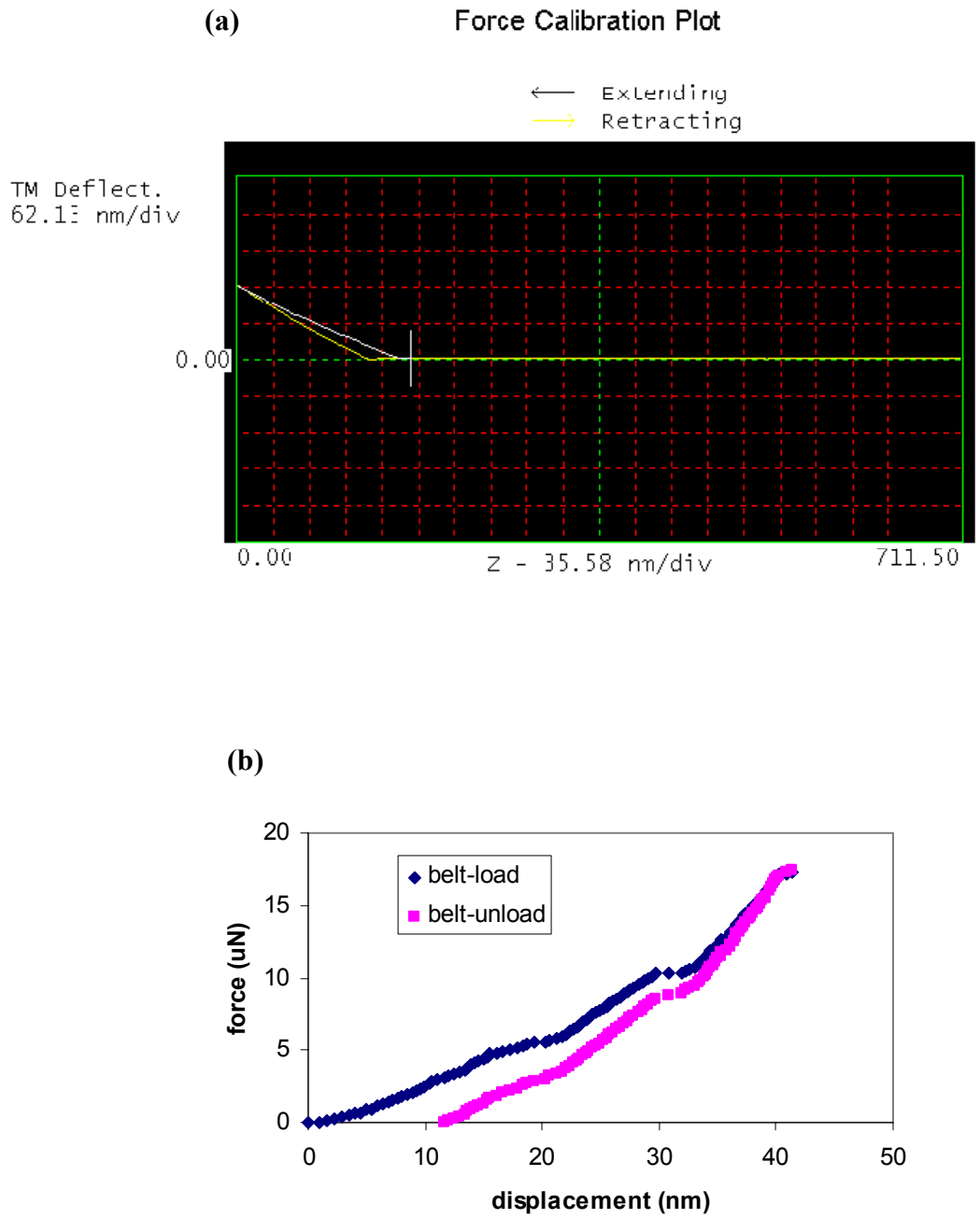

Figure 3.20 Force curve of nanoindentation on ZnO nanobelt (a) original deflection vs. z piezo movement curve (b) force vs. displacement curve

Another remarkable feature of Figure 3.18 is that ZnO nanobelt is softer than that of bulk single crystal, contrary to the conventional believing of "smaller is stronger" based on continuum considerations. One possible reason is due to difference in the mobility of the dislocation. Bradby [131] et al found the slip bands along the basal planes which result in pinning of dislocations in XTEM image of a spherical indent in (0001) ZnO bulk. The same might be true for our bulk sample. However, there might be no or little pinning of the dislocation in the nanobelt since the interval of slip bands along the basal planes which result in pinning is in the order of 1μm [131], while the dimension of the nanobelt is below 1μm. Hence, stronger dislocation mobility results in more plasticity in the nanobelt than the bulk.

Although measurements on plastic yielding of three different types of micrometer-sized single crystals [132], Ni, Ni_3Al-Ta and Ni superalloy, indicates the smaller the sample size, the higher the yield stress, our result is consistent with the nanoindentation of patterned metal lines on a Si substrate[133, 134]. The smaller the line width (from 5μm to 1.5μm), the more compliant the indentation response. The mechanism for the observed phenomena can be analyzed in terms of discrete dislocations.

Considering that those dislocations are generated near the indenter tip and that they glide along the slip plane to the side surfaces, the effect of dislocation glide on the indenter tip penetration depth in the nanobelt can be rationalized in the following manner. For simplicity, consider a nanobelt with dislocations parallel to the z direction. Assuming that the dislocations move in the cross-sectional plane of the belt, (which has height of h and width w, as shown in the schematic in Figure 3.21), the additional plastic shear strain of the cross-section becomes $\gamma = (2xb_x / wh)$, where b_x is the projected magnitude of the Burgers vector along x direction and

x is the dislocation glide distance parallel to the belt surface. When there are N dislocations that move over the average glide distance λ, the plastic strain around the indenter tip is given by $2\lambda Nb_x/wh$. This additional strain due to dislocation movement along the belt width direction is negligible in the case of bulk samples for which $w \to \infty$. For the case of the belt, however, the material displacement around the indenter tip accompanying this strain becomes $2\lambda Nb_x/w$ for a fixed belt thickness of h. As a first order approximation, the total indentation depth in the belt is assumed to be a linear sum of the displacement due to dislocation generation along the indentation direction ($h_{bulk} \sim Nb_y$, where b_y is the projected magnitude of the Burgers vector along the indentation direction), and the additional displacement of the tip due solely to the geometrical effect of the dislocation movement parallel to the belt surface. Thus the total indentation depth in the belt becomes:

$$h_{belt} = h_{bulk} + h_{geo} = h_{bulk} + \alpha \frac{2\lambda N b_x}{w} \qquad (3.28)$$

Where α is a geometrical constant that includes the relative direction of dislocation motion with respect to the indentation axis. Due to the finite width of the nanobelt, the nanobelt will be more compliant than the bulk according to Eq. (3.28). This finding has significant effect on the application of quasi-one-dimensional nanostructures in MEMS and NEMS.

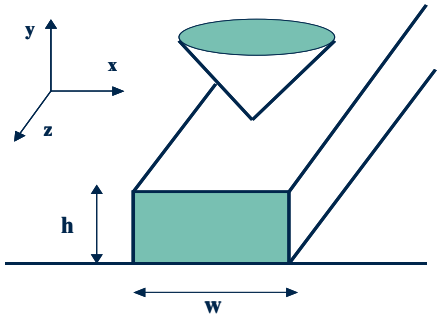

Figure 3.21 Schematic of nanoindentation on ZnO nanobelt

In addition, it is interesting to mention the Finite element modeling (FEM) [133]of a sharp conical indentation of the continuous Al-1.5wt%Si film, as well as on 2 and 3 μm wide lines of the same 1μm thickness on a Si substrate. The corresponding P-h curves in Figure 3.22 show that the response of these cases are essentially indistinguishable up to a load of 400μN, which is contradictory to the experimental finding. Therefore, the continuum-based approach such as FEM could not rationalize the experimental trend.

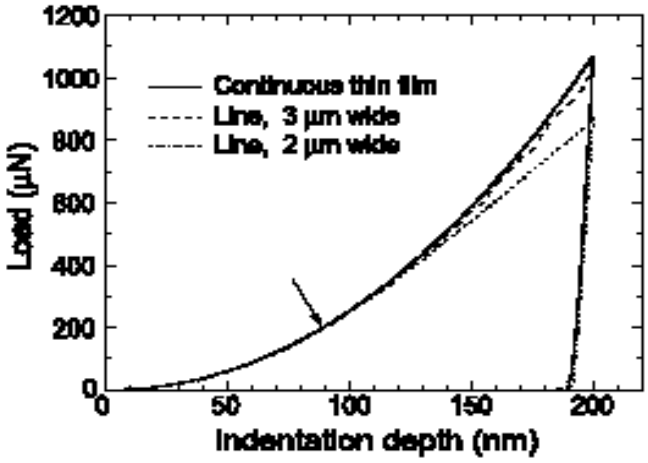

Figure 3.22 Load-displacement response of Al line predicted by FEM analysis [133]

In summary, plastic behavior of ZnO nanobelt is very different from its bulk counterpart. The hardness of the ZnO nanobelt is much smaller than that of the ZnO bulk. This trend cannot be explained by the existing theory based on continuum mechanics, while it is accountable using discrete dislocation concept. Furthermore, indentation size effect is analyzed in terms of surface to volume ratio. Hardness at the nanoscale is both depth and indenter dependent.

3.6 FRACTURE OF NANOBELT UNDER AFM NANOINDENTATION

Nanoindentations were also done using cantilever typed diamond indenter with a sharp tip radius of 18nm (determined by procedures in Appendix A.2). In this case, we frequently observed indentation-induced fracture in ZnO nanobelt, while it was not true for ZnO bulk up to an indentation force of 43μN. Figures 3.23 and 3.24 are 3 dimensional images of a typical ZnO nanobelt before and after nanoindentation. Before indentation, the surface of the nanobelt is perfect and smooth (with roughness Ra $\approx$ 0.2nm in a 200×200nm region). After indentation, the surface of the nanobelt becomes very rough. There are strip-like pile-ups along the axis of the nanobelt, indicating very severe plastic deformation involved in the nanobelt during indentation. This is remarkable since ZnO is normally regarded as a brittle material in bulk form. Furthermore, radial cracks along the apex of the pyramid indenter are clearly shown. It is of great interest if we can deduce the fracture toughness of the nanobelt from this test. Figure 3.25a is the cantilever deflection versus z piezo movement recorded during the indentation. A deflection drop is clearly shown in the graph, demonstrating the point that the crack is produced under the indenter. Figure 3.25b is the force versus displacement curve converted from Figure 3.25a by a standard procedure (Appendix A.1). The force dropping point is around 33 μN at the indentation depth of 58nm. The cracking thresholds can be estimated as [135] :

$$\sigma_C = \frac{1-2\upsilon}{3}\left(\frac{6E_r^2}{\pi^3 R^2}\right)^{1/3} P^{1/3} \qquad (3.29) \quad ,$$

where υ is Poisson's ratio (0.36 for ZnO), E_r is reduced modulus (61GPa for ZnO nanobelt), R is indenter radius (18nm), and P is the critical load (33 μN). Using the above parameters, the cracking thresholds was estimated to be 3.9GPa, which is comparable to the value

($\sigma_C \approx 3.4\ GPa$) reported on the SnO_2 nanobelt [74]. The average crack length, c, determined from Figure 3.24 is ~500nm. Taking E=70GPa and H=2GPa, the fracture toughness of the ZnO nanobelt is estimated to be 0.022 $MPa \cdot m^{1/2}$ using Eq. (3.11). This value is close to the average fracture toughness of SnO_2 nanobelt (0.044 $MPa \cdot m^{1/2}$) determined by nanoindentation [74]. But it is one order of magnitude less than the other bulk brittle materials [83]. That may be why we did not observe indentation induced crack in ZnO bulk.

It is worth mentioning that there may be large errors associated with the fracture toughness determined by Eq. (3.11), which is based on the brittle bulk materials. In this case, it is an one dimensional nanostructure. So the boundary condition here is very different from that of the bulk, which plays an important role in the cracking process. Furthermore, as ZnO nanobelt has much higher surface to volume ratio than that of the bulk, surface effects such as surface stress may affect the nucleation and development of the crack in the ZnO nanobelt. Hence, a new model for indentation induced cracking in one dimensional nanostructures is highly desirable. The preliminary results here show that the fracture toughness of one dimensional nanostructures may be one order lower than their bulk counterparts, which is of great importance for the MEMS and NEMS design and application.

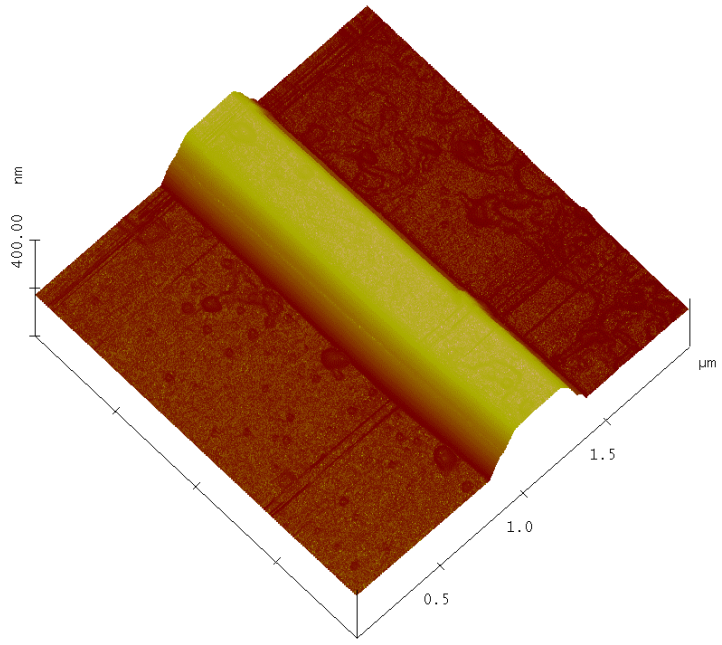

Figure 3.23 AFM 3D image of the nanobelt before indentation

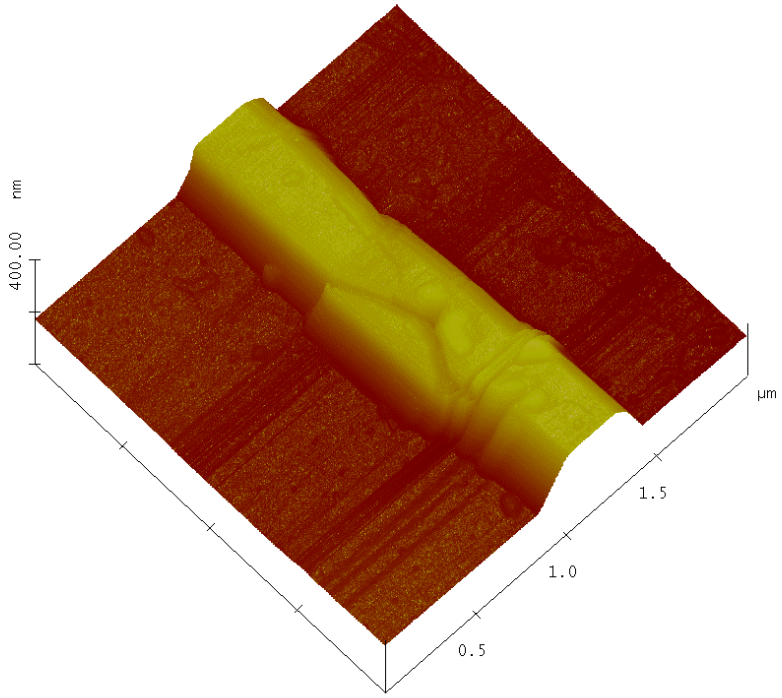

Figure 3.24 AFM 3D image the nanobelt after indentation (peak load 34 µN)

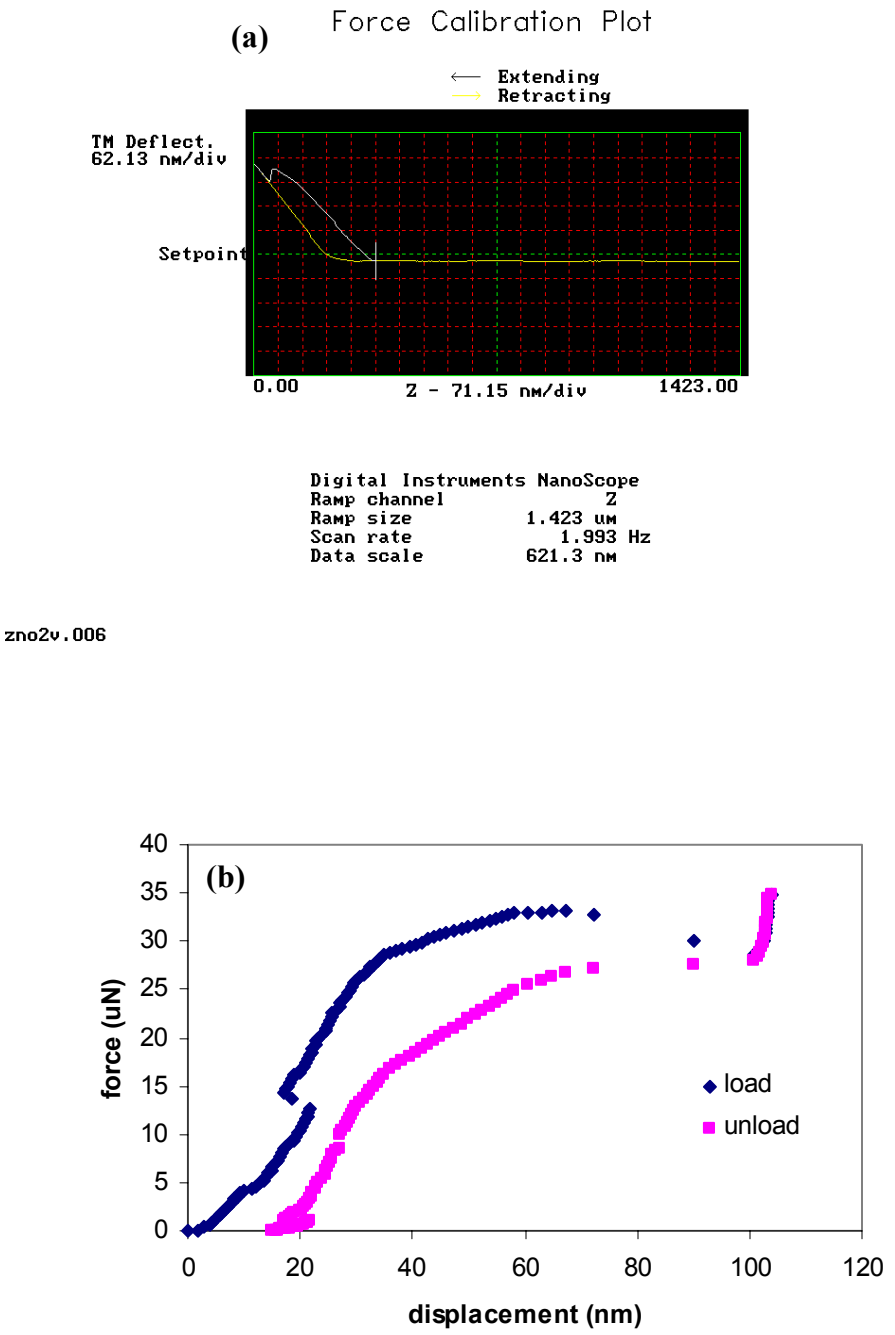

Figure 3.25 Mechanical response of the nanobelt during indentation (a) **cantilever deflection versus Z piezo movement curve** (b) **force versus displacement curve converted from (a)**

3.7 NANOMACHINING

As mentioned earlier, ZnO nanobelt is targeted for the fabrication of MEMS and NEMS. Nanomachining is necessary for the building blocks of nano devices. However, the nanoscale size prohibited the well-developed machining methods. AFM can serve as a powerful tool in this respect [136]. As shown in Figure 3.26, bending and cutting on ZnO nanobelt using AFM tip is possible. It is also remarkable to notice that ZnO nanobelt can be bent to a large angle while ZnO is a brittle material in the bulk form. This structural flexibility derives from the nanometer thickness of the ribbons, as the bending energy depends proportionally on the belt thickness cubed-the thinner the belt, the more flexible it will be.

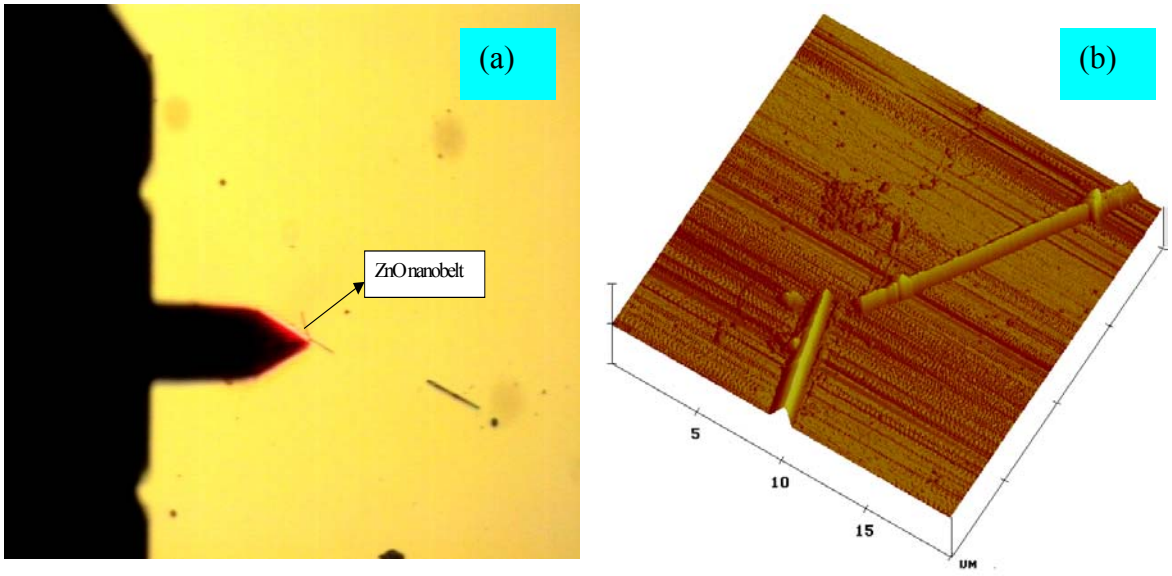

Figure 3.26 Nanomaching on ZnO nanobelt by AFM tip (a) bending (b) cutting

4.0 OPTOMECHANICAL PROPERTIES OF ZNO NANOBELT

Photoplastic effect is well known in bulk ZnO [137-139]. That is, the flow strength of the material increases after illumination. In addition, the optical properties (refractive index) of ZnO can be modified by elastic stress or elastic strain (photoelastic effect), suggesting a potential strong mechanical and optical coupling in ZnO. In the following, optomechanical properties of ZnO nanobelt will be studied in the two realms: elastic and plastic.

4.1 PHOTOINDUCED ELASTIC EFFECT

ZnO nanobelt, a quasi-one-dimensional nanostructure with rectangular cross section first reported by Dr. Wang's group in 2001, has unique mechanical [38] and piezoelectric properties [37], which are quite different from its bulk. Due to its perfect single crystallinity and excellent piezoelectric properties, ZnO nanobelt is becoming an attractive candidate for surface acoustic wave (SAW) devices[140] with the miniaturizing trend of SAW devices. As the velocity of surface acoustic wave is proportional to the square root of Young's modulus, the influence of the light on the elastic properties of a ZnO nanobelt is important for its application as a SAW device. Although the optical properties (refractive index) of ZnO can be modified by elastic stress or strain (photoelastic effect [141-143]), there has been no report in the influence of the light on the elastic properties of ZnO yet. Here we report the newly observed photoinduced reversible hardening of effective Young's modulus in a single ZnO nanobelt by AFM, while the effect is not observed in ZnO bulk. This is the first observed photoinduced strong elastic effect in an 1D semiconducting nanostructure. The physical mechanism for the observed phenomena is analyzed

in terms of surface effect and the electronic strain induced by the photogeneration of free carriers in ZnO.

Since traditional techniques on elastic modulus measurement, such as tensile test or acoustic measurement, are inapplicable to the nanoscale samples, nanoindentation is currently the first choice for the study of nanoelasticity [144]. Nanoindentations on ZnO nanobelt and (0001) bulk (5×5×0.5mm, supplied by M.T.I. Corp.) were first done by a Hysitron Triboscope nanoindenter in conjunction with a Veeco Nanoscope IIIa Multimode AFM. After nanoindentations, the indentation impression was imaged with the same tip, which verifies that the test was performed in the anticipated location. Reduced Young's modulus of ZnO nanobelt can be derived from unloading part of load-displacement curve using Oliver and Pharr method [87] .

Comparison of nanoindentations on the ZnO nanobelt with and without illumination reveals a marked difference in the load-displacement curve (Figure 4.1). Although the plastic deformation is similar in the two cases, the total deformation (elastic plus plastic deformation) with illumination is much smaller than that without illumination, which gives that the elastic deformation in darkness is much larger than that in light. As the load in two cases is similar, larger elastic deformation means lower elastic modulus. This is consistent with the results derived from unloading part of the load-displacement curve (Fig. 4.3) using Oliver-Pharr method. Fig. 4.3 provides comparison of illumination induced Young's modulus hardening between ZnO nanobelt and (0001) bulk. While there is little change of Young's modulus in ZnO bulk with and without illumination, the hardening of Young's modulus by illumination is at least 200% in the indentation depth from 10nm to 80nm. In the meantime, the effect was reversible. The hardening effect would disappear when the light was turned off.

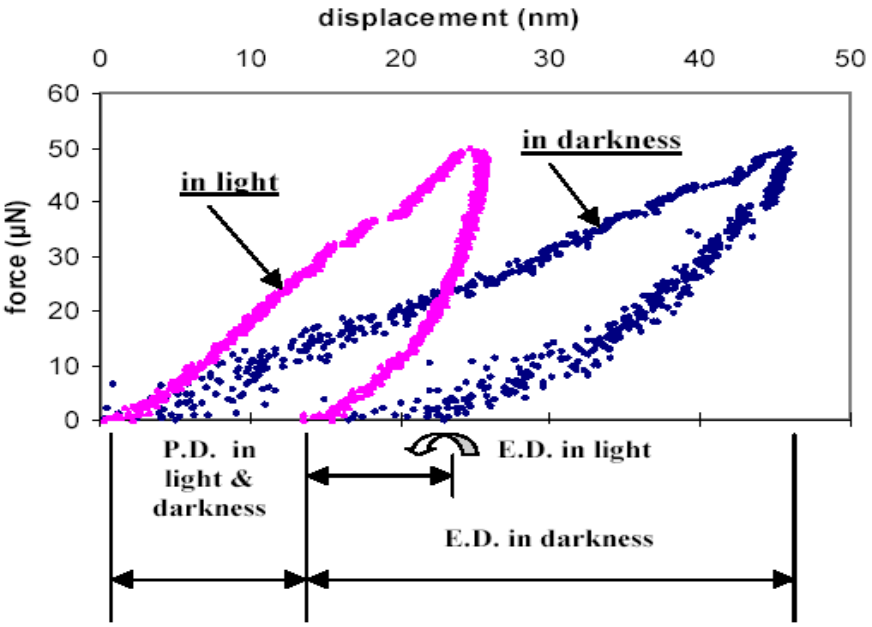

Figure 4.1 Comparison of force-displacement curve of ZnO nanobelt in light and darkness

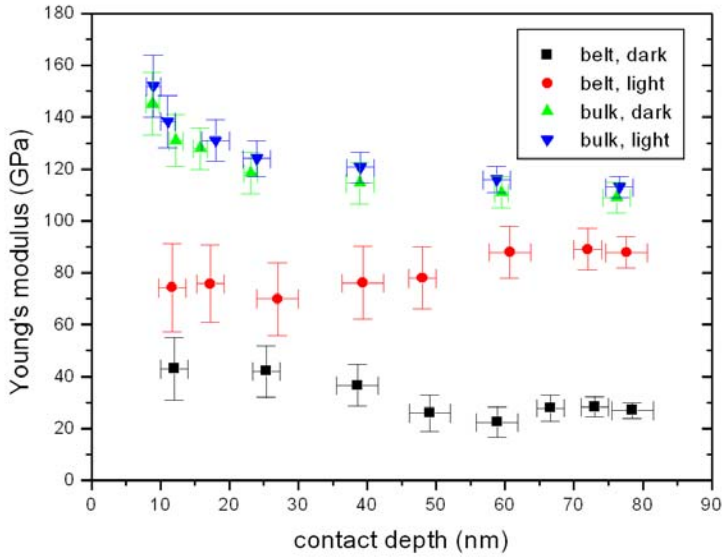

Figure 4.2 Comparison of measured Young's modulus between ZnO nanobelt and bulk with and without illumination

On the other hand, the Young's modulus estimated from the unloading stiffness is impossible to exclude the effect of inelastic processes, as unloading is not a purely elastic process [145]. Furthermore, there is an increase in the effect of inelastic processes on the unloading curve with increasing maximum load, which ranges from 20μN to 200μN currently. Further decreasing the maximum load on a ZnO sample by Triboscope will result in the unacceptable scattering of the data. That is why an alternative method was used to study this phenomenon and to check the consistency.

The other nanoindentation method was performed with Nanoscope IIIa Multimode AFM by using stainless steel cantilever with a diamond tip. In this case, an in-line filter box (FHS-UV from Ocean Optics Inc.) was applied between the light source and fiber illuminator. Two kinds of filter were used during illumination. One is a 360nm band-pass filter (passing 340-380nm light with peak at 360nm), which provides illumination with photon energy higher than the band gap of ZnO (3.34eV or ~380nm). The other kind of filter is a 550nm high pass filter (cutting light below 550nm), which provides illumination with photon energy lower than the band gap of ZnO. The spring constant of the cantilever was calibrated by Veeco Instruments to be 286.2 N/m. A diamond tip with a tetrahedral geometry (a three sided pyramid with an apex angle of 90 degrees and a nominal tip radius of 25nm) was mounted to the end of the cantilever in a way that the vertical axis of the pyramid was approximately normal to the sample surface. Before nanoindentation, the nanobelt was located by the diamond tip under tapping mode. Then the tip was positioned still to the center of the nanobelt. During nanoindentation, the contact between the tip and the sample at the ultra-low load (below 1μN) is mainly spherical and can be described as Eq. (4.1) using Hertzian model [146]. No indent is found after nanoindentation, which confirms the contact is elastic.

$$F = \frac{4}{3} E^* R^{1/2} h^{3/2} \text{ ……(4.1)}$$

Where F is the indentation load, E^* is the effective elastic modulus of the tip-sample system defined similar to Eq. (3.3). $E_i >> E \Rightarrow E \approx E^*$. R is the tip radius and h is the penetration depth in the sample. F and h can be experimentally derived from Eqs. (4.2) and (4.3).

$$F = k_c \times d_c = k_c \times \Delta \times U_c \qquad (4.2)$$

$$h = z - d_c = z - \Delta \times U_c \qquad (4.3)$$

Where k_c is the spring constant of the cantilever and d_c is the cantilever deflection, z represents the piezo-scanner movement along vertical direction and U_c is the cantilever deflection signal.

As z and U_c are directly available from the experiment (Figure 4.3a) and k_c=286.2 N/m, the key step to determine $F-h$ curve using Eqs. (4.2) and (4.3) is to find out the cantilever sensitivity Δ. This sensitivity is the ratio of the Z motion of the piezo, measured in nm, to the cantilever deflection, measured in volts. Its units are nm/volt and are determined from the slope of the force-plot curve by indenting on hard surface such as sapphire with a Young's modulus of 470GPa [145] . Under such circumstance, the penetration depth in the sample is negligible, which means $h \approx 0$ and $z \approx d_c$. Hence $\Delta \approx z / U_c$.

Once the $F-h$ curve is derived, we can find out E^* and R by parameter fitting using Eq. (4.1). However, there are two parameters involved in the fitting and R should be a fixed constant as long as the tip is not blunted during indentation. So we first find out R by nanoindenting on the fused quartz in the elastic region, of which the reduced Young's modulus is well known to be 69.6GPa. The average results of fitting to ten $F-h$ curves give $R \approx 18$nm.

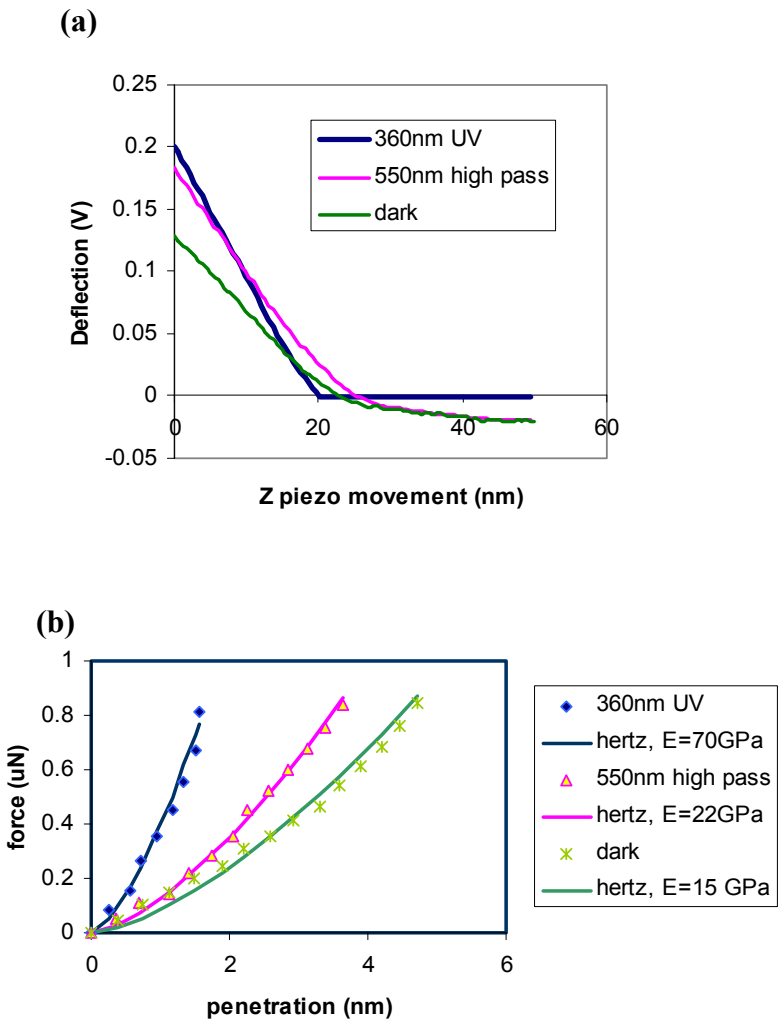

Figure 4.3 Nanoindentations on the ZnO nanobelt under various illuminated condition by cantilever typed diamond tip. (a) Comparison of the original Deflection-Z piezo movement curve of the ZnO nanobelt under 360nm UV, 550nm high pass illumination and in darkness by a cantilever-typed diamond indenter (only part of the approaching curves are shown here); (b) Comparison of a typical force-penetration curve of the ZnO nanobelt under 360nm UV, 550nm high pass illumination and in darkness by a cantilever-typed diamond indenter (radius R=18nm).

Once R is known, one parameter fitting to Eq. (4.4) gives E^*. Figure 4.3a is several original deflection-z piezo movement curves of ZnO nanobelt under 360nm UV, 550nm high pass illumination and in darkness by a cantilever-typed diamond indenter (only part of the approaching curves are shown here). Figure 4.3b is derived from Figure 4.3a using Eqs. (4.2) and (4.3), a comparison of a typical force-penetration curve of ZnO nanobelt under 360nm UV, 550nm high pass illumination and in darkness and fitted using Hertzian model of Eq. (4.1). By examining the features revealed in Figure 4.3, we can get the following information. First, the one-parameter fitting (indenter radius R=18nm) using Hertzian model matches perfectly to the experiment, which indicates that the contact between the indenter and ZnO nanobelt can be described as Hertzian elastic. Second, we can see that Young's modulus of the ZnO nanobelt in darkness (only 670nm laser is illuminated on the mirror of the cantilever) and 550nm high pass illumination is 15GPa and 22GPa respectively, while it is 70GPa under 360nm UV illumination and almost independent of the intensity of the illumination(~1-100mW/cm^2). Again we find the photoinduced hardening of Young's modulus in the ZnO nanobelt is reversible. The results provide us with the following information. i) Young's modulus of the ZnO nanobelt is very sensitive to the UV illumination (above the band gap of ZnO 380nm) and not sensitive to the below band gap illumination and light intensity. ii) Young's modulus of the ZnO nanobelt derived from the loading part of the force-penetration depth curve below 5nm using Hertzian model is comparable to that determined by the unloading part of the nanoindentation curve below 80nm using Oliver and Pharr method. Both results are in agreement with the derived values from the TEM resonance method, which ranges from 40-60GPa [15] . In contrast, there is

little difference in Young's modulus of the ZnO bulk with and without illumination, which varies from 100-120GPa.

Here comes the key question. What is the mechanism for the photoinduced reversible Young's modulus hardening in a ZnO nanobelt? In general, the physical mechanism for the observed phenomena may be related to the electronic strain induced by the photogeneration of free charge carriers in ZnO. It is well known that the injection of free carriers results in the local mechanical straining of a semiconductor [147-149]. By illumination with photons of energies above the ZnO band gap, electron-hole pairs are generated. The electronic strain in the illuminated diamond-type semiconductor is in the form of [148] ,

$$S_e = \frac{1}{3}\frac{d\varepsilon_g}{dP}\Delta n \qquad (4.4)$$

Where $d\varepsilon_g / dP$ is the pressure dependence of the band gap energy, Δn is the density of photogenerated excess charge carriers expressed in cm^{-3}.

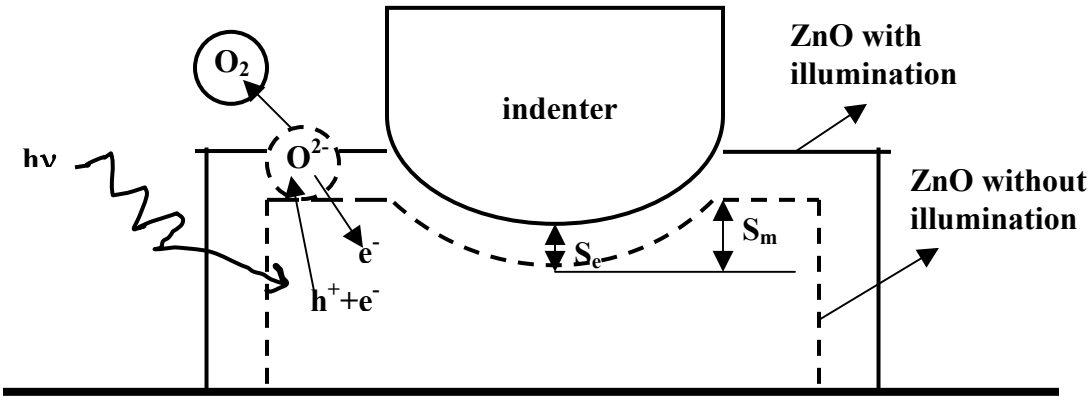

Figure 4.4 Surface response of ZnO by nanoindentations with and without illumination.

Without illumination, surface response of ZnO (dotted line) by nanoindentation is S_m and there are oxygen ions adsorbed on the surface. With illumination, the surface expanded (solid line) and the corresponding deformation due to the electronic strain is S_e, which gives the net surface

response S_m-S_e . In the meantime, holes produced by the illumination discharge the negatively charged oxygen ions on the ZnO surface, which results in extra free electrons in the ZnO.

As the expression of electronic strain for ZnO was not available, we treat the photoinduced electronic strain similar to the case of silicon. As shown in Figure 4.4, surface response of ZnO (segmented line) by nanoindentation is S_m without illumination. According to Eq. (4.4), the electronic strain in ZnO under illumination will be positive since the pressure dependence of band gap energy is positive for ZnO (~24.5 meV/GPa=3.92×10^{-24} cm^3 for ZnO [150]). This results in the expansion of the ZnO with illumination. The surface expands (Figure 4.4, solid line) and the corresponding deformation due to the electronic strain is S_e. It is worth mentioning that the electronic strain as a result of photogenerated free charge carriers resists the mechanical strain caused by the indenter. Hence, the net surface response S_t under illuminated indentation is given by,

$$S_t = S_m - S_e = \frac{\sigma}{E} - \frac{1}{3}\frac{d\varepsilon_g}{dP}\Delta n = (\frac{1}{E} - \frac{1}{3}\frac{d\varepsilon_g}{dP}\frac{\Delta n}{\sigma})\sigma \qquad (4.5)$$

Where S_m is mechanical strain caused by the indentation, σ is the mechanical stress, E is Young's modulus. In addition, we define the effective Young's modulus measured by illuminated nanoindentation as,

$$\frac{1}{E_{eff}} \equiv \frac{1}{E} - \frac{1}{3}\frac{d\varepsilon_g}{dP}\frac{\Delta n}{\sigma} \Rightarrow \frac{E}{E_{eff}} = 1 - \frac{1}{3}\frac{d\varepsilon_g}{dP}\frac{E \bullet \Delta n}{\sigma} \qquad (4.6)$$

To determine the effect of the illumination on Young's modulus, it is critical to estimate the magnitude of the second term in Eq. (4.6). For ZnO, $d\varepsilon_g / dP \approx 24.5 meV/GPa \approx 3.92\times10^{-24} cm^{-3}$, The mean compressive stress caused by

nanoindentation can be estimated to be $\sigma = F/2\pi R\delta$ [151] , where F is the load of the nanoindentation, R is the radius of the indenter and δ is the penetration depth. If taking F=1μN, R=18nm and δ=2nm, we get $\sigma \approx$5GPa. Hence the key step to determine the effect of illumination is to estimate the magnitude of the photoinduced density of charge carriers Δn.

In the dark, oxygen molecules adsorb on the ZnO surface as negatively charged ions by capturing free electrons from the n-type ZnO and create an electron depletion layer near surface [152]. Upon exposure to over band gap light, electron-hole pairs were generated in ZnO. Photo-generated holes then migrate to the surface and discharge the negatively charged oxygen ions on the ZnO surface (Figure 4.4). Hence, the photo-generated electrons can increase the density of free charge carriers Δn near the surface as ZnO is normally a n-type semiconductor [153] . To better understand the different case in ZnO belt and bulk; we will distinguish the increase of the free charge density by the following two contributions.

$$\Delta n = \Delta n_p + \Delta n_d \qquad (4.7)$$

Where Δn_p is the contribution from the photoinduced electron hole pairs ($h\gamma \rightarrow h^+ + e^-$), and Δn_d is the contribution from the desorption of the oxygen gas on the surface ($O_2^- + h^+ \rightarrow O_2$ or $O^{2-} + h^+ \rightarrow O_2 + e^-$) . It is important to note that the penetration depth for photons with energies higher than the band-gap energy of ZnO is only approximately 100nm [138]. Since the thickness of ZnO nanobelt is comparable to the penetration depth of UV light, the whole cross section of the nanobelt may be photo-activated and become an electron rich layer, while only the surface of ZnO bulk is photoactivated. Due to the diffusion of free carriers, we can conclude $\Delta n_{p,belt} >> \Delta n_{p,\ bulk}$ during illumination. Furthermore, as the nanobelt has much higher surface to volume ratio than the bulk, there will be more chance for the photo-generated holes to be discharged on

the surface of the nanobelt than that of the bulk. Hence, $\Delta n_{d,\ belt}$ is also larger than $\Delta n_{d,\ bulk}$ during illumination. In fact, the high density of electron carriers in the ZnO nanobelt was manifested by the several orders of increase of the current upon UV illumination [152, 154], compared to the several times of increase in ZnO bulk [138] . Therefore, we can qualitatively understand the photoinduced electronic strain would be much larger in the ZnO nanobelt than that in the ZnO bulk due to the surface effect. This may be the reason why photoinduced elastic hardening was not observed in the ZnO bulk. If we further make an estimation of the Δn required to have a marked elastic effect using Eq. (4.6), Δn is in the order of 10^{22} cm^{-3}, which is too high to reach. So the electronic strain in ZnO may be proportional to the $(\Delta n)^m$ instead of Δn in Si, where m is a constant greater than 1. For instance, if m=1.3 and $\Delta n=10^{17} cm^{-3}$, E/E_{eff} would be equal to 0.5 using revised Eq. (6). Such density of photo-generated charge is reasonable for the ZnO nanobelt during UV illumination. When light is turned off, the recombination of electron-hole and reabsorbed oxygen on the ZnO surface reduced the density of free charge carriers, which results in less contribution from electronic strain. Hence photoinduced strong elastic effect in the ZnO nanobelt is reversible.

In conclusion, photoinduced reversible hardening of Young's modulus was observed in a single ZnO nanobelt. This is the first observed photoinduced strong elastic effect in an 1D semiconducting nanostructure, which is of theoretical and practical significance. Theoretically, electronic strain may play an important role in the mechanical deformation of 1D semiconducting nanostructure under over band gap illumination. Practically, our experimental results indicate that elastic properties of 1D ZnO nanostructure may be tuned by the optical illumination, which sheds light on realizing nanoscale optical tunable SAW devices based on 1D ZnO nanostructure.

4.2 PHOTOINDUCED PLASTIC EFFECT

Photoplastic effect (PPE) in ZnO, the reversible increase in flow strength upon illumination, was first discovered by Carson and Svensson in 1968 [137, 138]. Zinc oxide is an n-type excess semiconductor that means that there is excess zinc in the crystal. These excess atoms exist in interstitial positions and are singly ionized at room temperature. This ionization caused the n-doping. By illumination with photons with energies higher than the bandgap, electron-hole pairs are generated. The holes will then be captured by traps in the material. It has been proposed that these traps are the excess zinc atoms which, by capturing a hole, becoming doubly ionized. The process is therefore an indirect ionization of Zn^{+} to Zn^{2+}. It is likely that direct photoionization of Zn^{+} to Zn^{2+} also occurs. In addition, it is reasonable to assume that the dislocations are negatively charged in n-type zinc oxide through trapping of majority carriers by traps in the dislocations. The negatively charged dislocations interact more strongly with the doubly charged zinc ions than the singly charged zinc ions thus raising the flow stress by dislocation locking. Recently, nanoindentations on ZnO bulk revealed PPE under 100nm indentation depth [139]. The current study finds similar effect in ZnO nanobelt as observed in ZnO bulk.

As shown in Figure 4.5, the hardness in the light is a bit higher than that in the darkness for the indentation depth below 50nm. The observation of a positive PPE effect at length scales significantly smaller than that required for dislocation charge was attributed to the much shorter dislocation travel distances required due to the high density of surface states which have energy levels within the bandgap. The lack of an observed PPE for indentations with a contact depth greater than 50nm is attributed to a reduced effect of the surface states to dislocation charging in this region and insufficient bulk charging resultant from short travel distances.

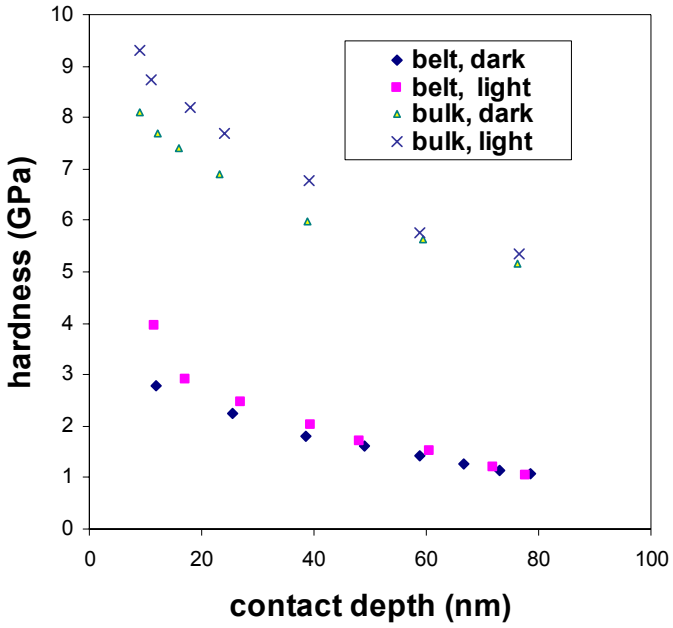

Figure 4.5 PPE effect of ZnO nanobelt and ZnO bulk by nanoindentations

5.0 ELECTROMECHANICAL PROPERTIES OF ZNO NANOBELT

ZnO is a traditional piezoelectric material with good electromechanical coupling. Piezoelectric ZnO is mainly employed in the form of polycrystalline thin film[16-23]. The grain boundary and other defects may weaken the piezoelectric coefficients because they pin the domain walls and inhibit poling of the materials. As ZnO nanobelt is perfect single crystalline and almost defect free, it is interesting to find out if it has much higher piezoelectric coefficient than that of polycrystalline thin film. The piezoelectric coefficients of the ZnO nanobelt are also critical parameters in the design of nanosensors or nanoactuators using its piezoelectric properties.

In addition, ferroelectricity was discovered in the Li-substituted piezoelectric ZnO [155-164]. It is also interesting to find out if ferroelectricity existed in Li-doped ZnO nanobelt. If Li-doped ZnO nanobelt is ferroelectric, it will be a promising material for nanoscale integrated ferroelectric devices and optoelectronic devices.

The following sections start from piezoelectric coefficient measurement of the ZnO nanobelt without and with Li doping. Then ferroelectric measurement on Li-doped ZnO nanobelt is carried out.

5.1 PIEZOELECTRIC MEASUREMENT

The most common growth direction of the ZnO nanobelt is along the c-axis [0001] or [01 $\bar{1}$ 0], with the top surface being ($2\bar{1}\bar{1}0$) and side surface being ($01\bar{1}0$) or (0001), respectively (Figures. 5.1a and b). This is because surface energy of ($01\bar{1}0$) and ($2\bar{1}\bar{1}0$) are lower than that

of (0001). Growth of (0001) surface dominated nanobelt has to overcome an energy barrier due to surface polarization. Recently, freestanding piezoelectric ZnO nanobelts with large top and bottom surfaces being the polar (0001) facets were reported [165].

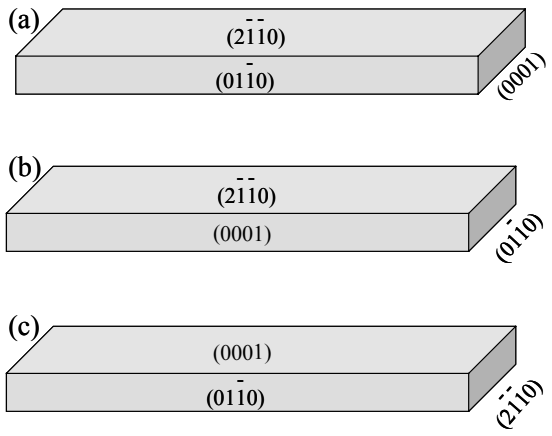

Figure 5.1 Surface facets of ZnO nanobelts: (a) growing along [0001] (c axis), top surfaces (2 $\bar{1}$ $\bar{1}$ 0) and side surfaces (01$\bar{1}$0), showing no piezoelectric property across thickness; (b) growing along [01$\bar{1}$0] (c axis), top surfaces (2 $\bar{1}$ $\bar{1}$ 0) and side surfaces (0001), showing no piezoelectric property across thickness; (c) growing along [2 $\bar{1}$ $\bar{1}$ 0] (a axis), top surfaces (0001) and side surfaces (01$\bar{1}$0), showing piezoelectric effect across thickness.

Investigating the piezoelectric properties of ZnO nanobelt using atomic force microscopy remains, however, a challenge because the sample's displacement due to the inverse piezoelectric effect by applying an electric field is in the order of pico-meter (pm). Several techniques [166], including scanning probe microscopy (SPM) [167-171], have been employed to measure these small piezoelectric displacements. In particular, piezoresponse force microscope (PFM) is becoming a standard method for the study of ferroelectric and piezoelectric phenomena. The PFM technique is based on the detection of local vibrations of a sample induced by an AC signal applied between the conductive tip of SFM and the bottom electrode of the

sample. The local oscillations of the sample surface are transmitted to the tip and detected using a lock-in technique. The out-of-plane piezoresponse signal is extracted from the z-deflection signal given by the PSD (position sensitive detector), and represents the local oscillations perpendicular to the plane of the sample surface. Though ferroelectric properties of individual Barium Titanate nanowires investigated by noncontact mode of SPM were reported by H. Park's group [170], there is no publication on piezoelectric measurement on one dimensional nanostructures using contact mode of SPM .

This study reports our measurement on the piezoelectric properties of individual ZnO nanobelt using PFM technique. The result is compared with that of the (0001) bulk ZnO and x-cut quartz. Our results show that the piezoelectric coefficient d_{33} for ZnO nanobelt is significantly larger than that of bulk ZnO, establishing the base of using ZnO nanobelts for nano-scale sensors and actuators.

5.1.1 Experimental description

The first step of the experiment was sample preparing. ZnO nanobelts without Li doping were prepared according to procedure mentioned in section **2.2.1**. ZnO nanobelts with Li doping were prepared by thermal evaporation of ZnO and Li_2CO_3 powder (10%) under 1300°C and 1200°C respectively. SEM and TEM pictures of Li doped ZnO nanobelt are shown in Figures 5.2 and 5.3. After coating (100) Si wafer with a 100nm Pd by DC sputtering, the prepared ZnO nanobelts were dispersed on the conductive surface similar to the way described previously. Then the whole surface was coated with another 5 nm Pd coating, which served as an electrode on ZnO nanobelt to get uniform electric field and avoid electrostatic effect. Extra care was taken to ensure that top and bottom surface of the nanobelt was not short circuited after Pd deposition.

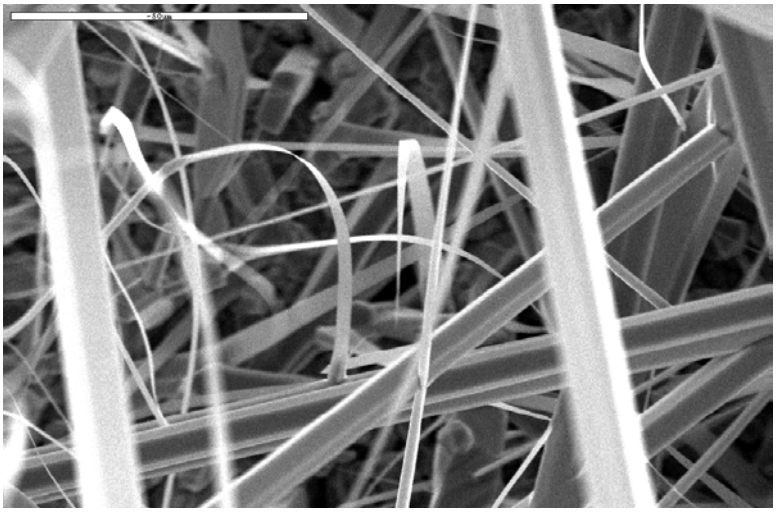

Figure 5.2 SEM picture of Li doped ZnO nanobelt synthesized by thermal evaporation

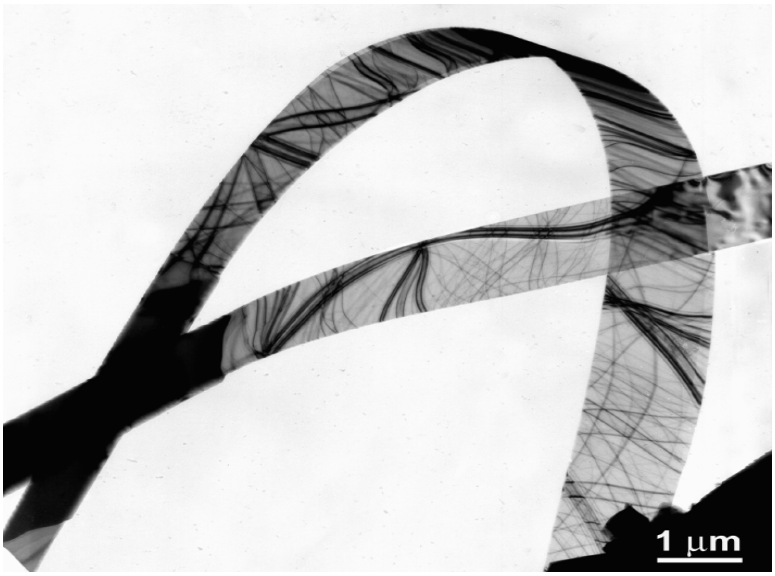

Figure 5.3 TEM picture of Li doped ZnO nanobelt

The single ZnO nanobelt was located by a commercially available AFM (Nanoscope IIIa, Multimode) under tapping mode. If contact mode was used, the nanobelt might be displaced by the tip during scanning, which caused a distorted image. Fig. 5.4 is a three dimensional image of an individual ZnO nanobelt lying on the surface by tapping mode, which clearly shows a rectangular cross section with thickness of 123nm. After locating the nanobelt, the tip was positioned still to the center of the nanobelt.

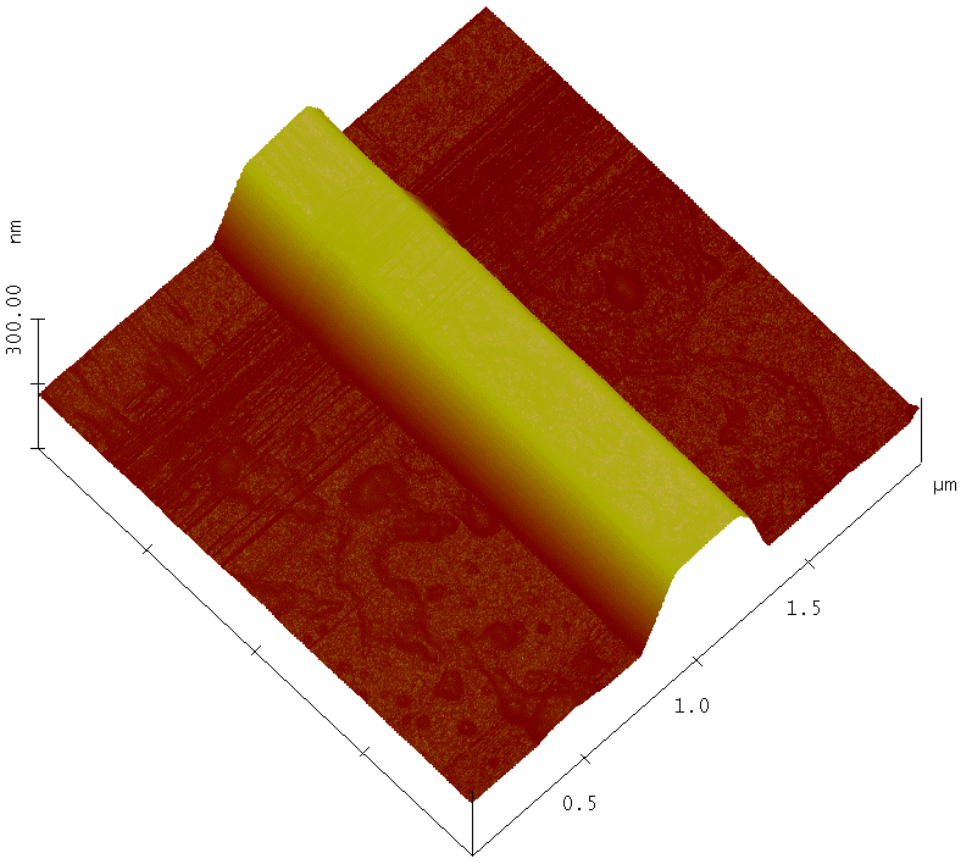

Figure 5.4 3D image of ZnO nanobelt for piezoelectric measurement

It is worth mentioning that not every nanobelt lying on the surface is piezoelectric. The nanobelt showing piezoelectric grows along [2 $\bar{1}$ $\bar{1}$ 0] with (0001) top surface as presented in Figure 5.1c. The polar axis of hexagonal wurtzite structured ZnO crystal is along [0001]. Piezoelectric measurements on ZnO nanobelt were performed in contact mode at a single point with the addition of a function generator, a lock-in amplifier (SR844) and a signal access module (SBOB) as shown in Figure 5.5.

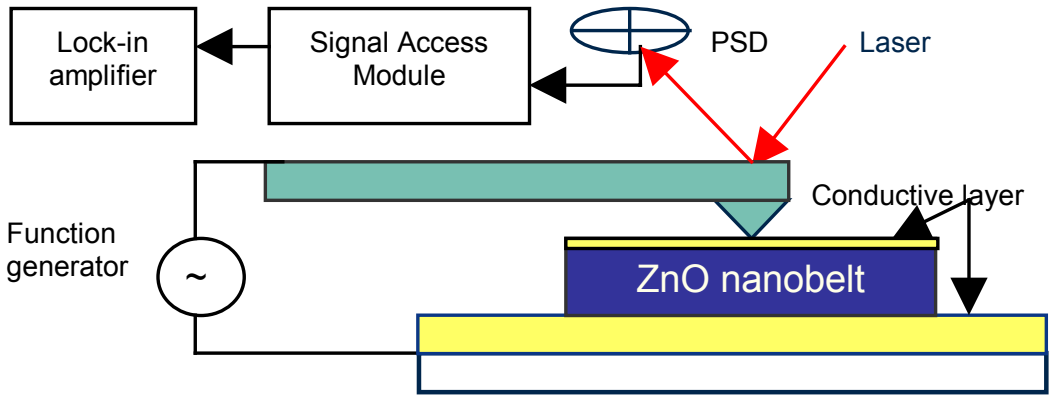

Figure 5.5 Schematic diagram of piezoelectric measurement setup.

In this configuration, the conductive tip supplies current to the electrode and also measures the piezoelectric motion. The conductive tip is made by coating 20 nm thick Pd on the commercial Olympus etched silicon probe with nominal spring constant of 42 N/m and tip radius of about 10nm. High stiffness cantilever is chosen to reduce the influence of electrostatic interaction with piezoelectric measurement [168]. The contact force between AFM tip and nanobelt is ~ 1800nN, which ensures the measurement is in the so-called strong-indentation regime proposed by S.V. Kalinin and D.A. Bonnell [172], as the piezoresponse in the strong-indentation regime is dominated by the d_{33} of the material. The typical resonance of the conductive tip is about 300

kHz. The frequency of signal applied on the sample is from 1kHz to 20 kHz, which is much higher than the low-pass cutoff frequency of AFM topography feedback loop and lower than the cantilever resonance frequency. The chosen frequency range is almost within the previously reported values on bulk or thin film samples, ranging from 1KHz to 16.7KHz [167-169, 171]. Input signal was in the range of 1-5 V (RMS). The corresponding vertical deflection signal of the cantilever is recorded by lock-in amplifier through SBOB. By multiplying the deflection signal with the calibration constant of the photo-detector sensitivity, the amplitude of the tip vibration is derived. The calibration constant is determined from the slope of force-distance plot after the scanner is calibrated using a standard grating. Since the scanner has been independently calibrated with a known step height, the vertical deflection signal is calibrated to the known vertical displacement. As illustrated in Equation (1), the slope of the amplitude A_f versus the input signal U_f gives the effective piezoelectric coefficient d_{33}^{eff} .

$$A_f = V_f \bullet \delta = d_{33}^{eff} \bullet U_f \tag{5.1}$$

Where A_f is vibration amplitude (in units of nm), V_f is vertical deflection signal of the cantilever (mV), δ is the calibration constant of the photo-detector sensitivity (nm/V), U_f is amplitude of the testing ac voltage (V).

To ensure the reliability and accuracy of the measurement, effective piezoelectric coefficient of (0001) bulk ZnO and x-cut quartz (serving as a piezoelectric standard) were measured using the same PFM technique. As to (0001) bulk ZnO (5×5×0.5mm, supplied by M.T.I. Corp.), both sides were coated with 100nm Pd and the bottom side was attached to the conductive surface using conductive epoxy. Similar process was applied to x-cut quartz (ϕ10×0.7mm, gold coating of 150nm on each side, courtesy of Bliley Technologies Inc).

5.1.2 ZnO nanobelt without Li doping

The best experimental results of piezoelectric measurement on the ZnO nanobelt without Li doping, (0001) ZnO bulk and x-cut quartz are presented in Figure 5.6.

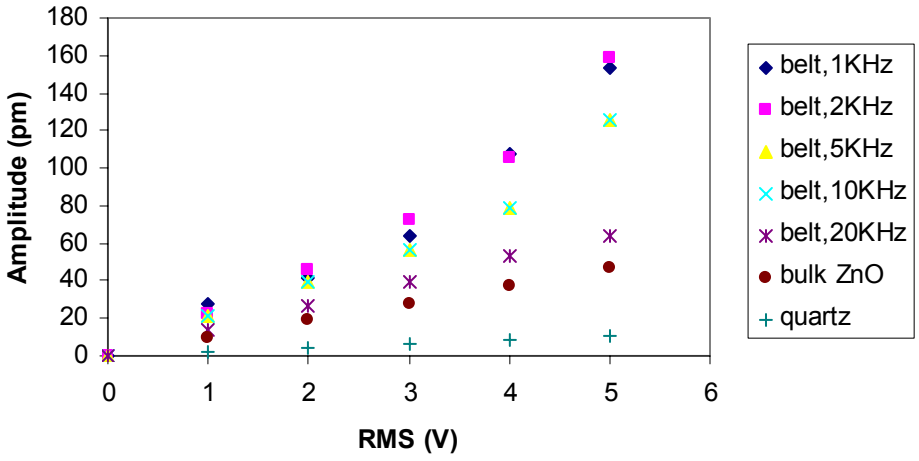

Figure 5.6 Piezoelectric measurements on ZnO nanobelt, bulk (0001) ZnO and x-cut quartz. Linear relationship between amplitude and applied voltage is shown in every case, the slope of which gives the piezoelectric coefficient.

From the slopes of the curve, the effective piezoelectric coefficient are d_{11} = 2.17 pm/V for x-cut quartz, d_{33} = 9.93 pm/V for (0001) bulk ZnO, which are almost independent of frequency. Compared to the accepted values, d_{11}=2.3 pm/V for quartz and d_{33} = 12.4pm/V for ZnO [168], the measured results for ZnO bulk and x-cut quartz are reasonable, confirming the reliability and accuracy of the measuring technique. The effective piezoelectric coefficient of ZnO nanobelt is frequency dependent and varies from 13.1 pm/V to 25.5 pm/V, which is much larger than that of the bulk ZnO. One possible reason for the observed enhanced electromechanical response for ZnO nanobelt might be due to its perfect single crystallinity and free of dislocation, as inherent reduction in the piezoelectric coefficient due to internal defects was revealed in ultra thin PZT

films [173]. As to commercially available single crystal bulk sample, certain degree of defects was inevitable. Next, increase of piezoelectric response with decreasing feature size in epitaxial PZT thin film was reported by S. Buhlmann et al [174]. The observed increase of piezoresponse amplitude was 300% with the decreasing of the film thickness from 200nm to 100nm, which was proposed to be mostly due to a change of domain configuration. Although this mechanism was not applicable to ZnO nanobelt with tens of nanometer in thickness, the possible size effect of its piezoelectricity needs further investigation. Furthermore, the different elastic boundary condition in piezoelectric measurement on ZnO nanobelt and bulk sample may contribute to the enhanced piezoelectric response. As to ZnO nanobelt, there is no constraint at interface between bottom side and conductive layer, while conductive epoxy is applied in the case of bulk sample. Hence, effective piezoelectric coefficient of ZnO nanobelt and bulk is given by Equation (5.2) and (5.3) using lateral free [175] and lateral full constrain [176] boundary condition respectively.

$$d_{33,belt}^{eff} \cong d_{33} \tag{5.2}$$

$$d_{33,bulk}^{eff} \cong d_{33} - \frac{2S_{13}}{S_{11}+S_{12}} d_{31} \tag{5.3}$$

Assuming d_{33} is the same in Equation (5.2) and (5.3), it is interesting to estimate the magnitude of the second term in Equation (5.3), which provides the effect of boundary condition. However, the components (S_{ij}) of compliance matrix (S) of ZnO is not directly available, which are derived from stiffness matrix C [177] using the relationship $S=C^{-1}$.

$$S = \begin{bmatrix} 6.401 & -1.932 & -2.539 & 0 & 0 & 0 \\ -1.932 & 6.401 & -2.539 & 0 & 0 & 0 \\ -2.539 & -2.539 & 8.351 & 0 & 0 & 0 \\ 0 & 0 & 0 & 14 & 0 & 0 \\ 0 & 0 & 0 & 0 & 14 & 0 \\ 0 & 0 & 0 & 0 & 0 & 17 \end{bmatrix} \times 10^{-12} (m^2/N) \tag{5.4}$$

Using the S_{ij} value from Equation (4) and d_{31}= -5.1 pm/V, we can estimate the second term in Equation (3) to be 5.795 pm/V. Taking d_{33}=12.4 pm/V (accepted piezoelectric coefficient of single crystal ZnO), we derive the conclusion that the boundary condition can change the effective piezoelectric coefficient up to 47%.

The frequency dependence of the piezoelectric coefficient is shown in Figure 5.7. Both ZnO bulk and x-cut quartz are almost frequency independent. As to ZnO nanobelt, the higher the frequency, the lower the piezoelectric coefficient d_{33}, which almost depends linearly on the logarithm of the applied field frequency. However, the result of 1 kHz measurement is abnormal to the general trend, which may be caused by noise at low frequency. Previous PFM measurement indicated the lower the measurement frequency, the higher the noise level. Such logarithmic frequency dependence was reported in ferroelectric materials such as PZT [178]. Even though ZnO is not ferroelectric, the logarithmic frequency dependence is generally valid in random systems that have properties controlled by interface pinning [179], such as pinning of spontaneous polarization in ZnO, which might be caused by surface charge due to the high surface to volume ratio of ZnO nanobelt. Another possible reason of the unexpected frequency dependence might originate from the imperfect electrical contact between the bottom of nanobelt and the conductive layer. With the increase of the input frequency, the quality of electrical contact decreases, which induces the lower electromechanical response of ZnO nanobelt.

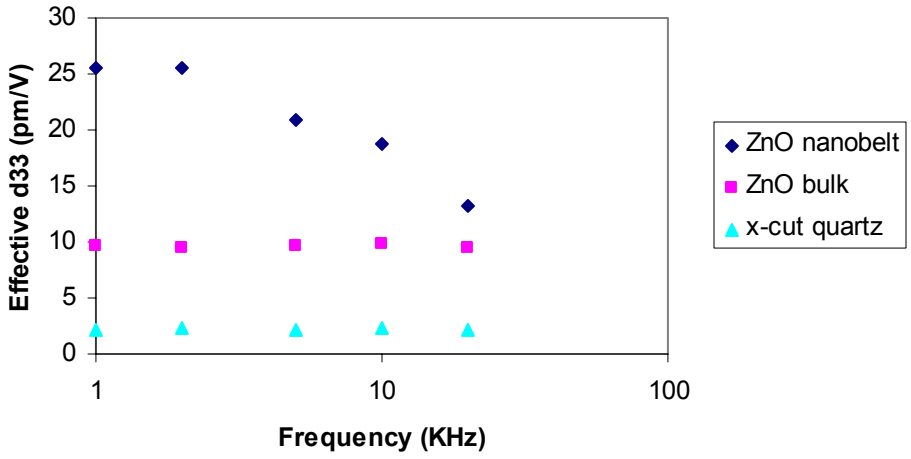

Figure 5.7 Frequency dependence of piezoelectric coefficient of ZnO nanobelt, bulk (0001) ZnO and x-cut quartz. Only piezoelectric coefficient of ZnO nanobelt is frequency dependent.

In summary, effective piezoelectric coefficient of the (0001) surface dominated ZnO nanobelt without Li doping has been measured by PFM and it is significantly larger than that of bulk (0001) ZnO. The effective piezoelectric coefficient of ZnO nanobelt is also frequency dependent, which may be due to the surface charge effect or imperfect electrical contact at the interface. However, it is worth mention that the above results are the best one selected from the measurement of 20 nanobelts. The majority of the nanobelts show little piezoelectric response (defined as d_{33} <3pm/V). The distribution of the experimental data will be provided at the next section.

5.1.3 ZnO nanobelt with Li doping

Figure 5.8 is a SIMS (Secondary Ions Mass Spectroscopy) graph of Li doping ZnO nanobelt, which shows Li peak. As no standard sample is available, we cannot quantatively determine the concentration of Li. However, as Li was not detected by XPS (X-ray Photoelectron Spectroscopy) analysis, its concentration must be lower than 8 mol%.

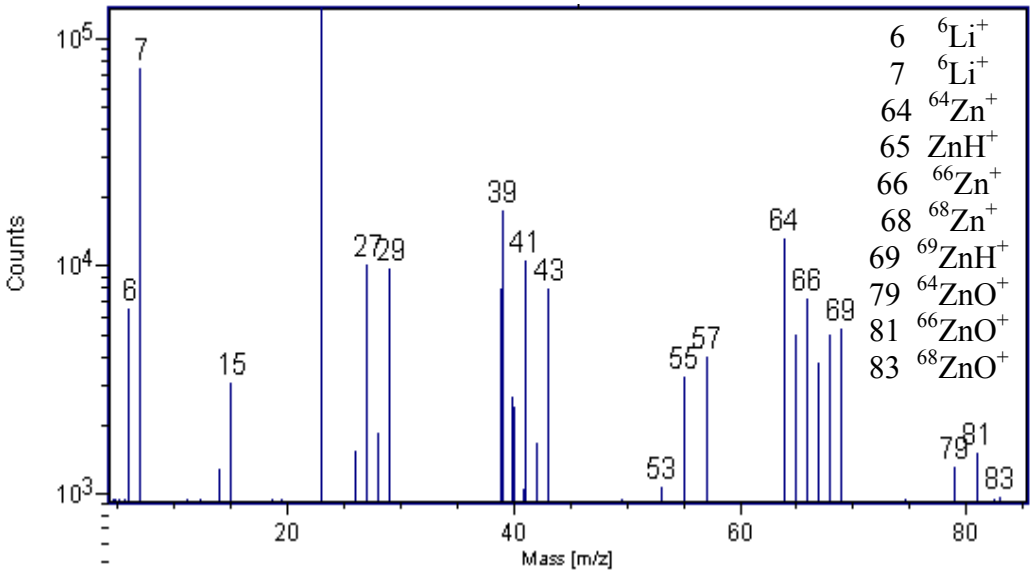

Figure 5.8 SIMS analysis of Li doped ZnO nanobelts.

Figure 5.9 shows the best results of effective d_{33} measurement derived from pure ZnO nanobelt, Li doping 1300 °C and Li doping 1200 °C. The striking feature is that the best results on the piezoelectric coefficient of the three cases are of little difference. Furthermore, the piezoelectric coefficient is frequency dependent and the highest piezoelectric response was captured at frequency of 2KHz. However, if we analyze 20 sets of the piezoelectric measurement data in each case, marked difference is shown in Figure 5.10. 18 out of 20 nanobelts without Li doping show little piezoelectric response, while only 2 out of 20 nanobelts are in the same category with Li doping. This may be attributed to the huge resistance increase by Li doping [155], which is

beneficial to the piezoelectric properties. In addition, the difference between 1300 °C and 1200°C Li doping was minor.

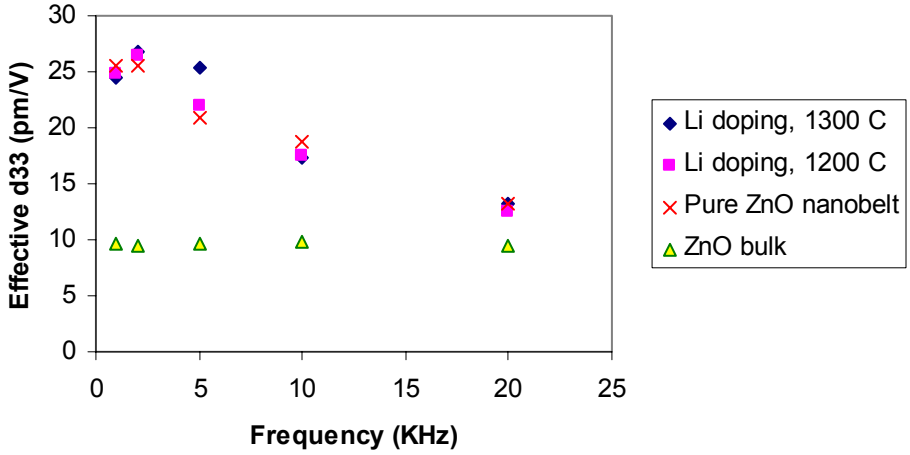

Figure 5.9 The best results of piezoelectric response of ZnO nanobelt with and without Li doping

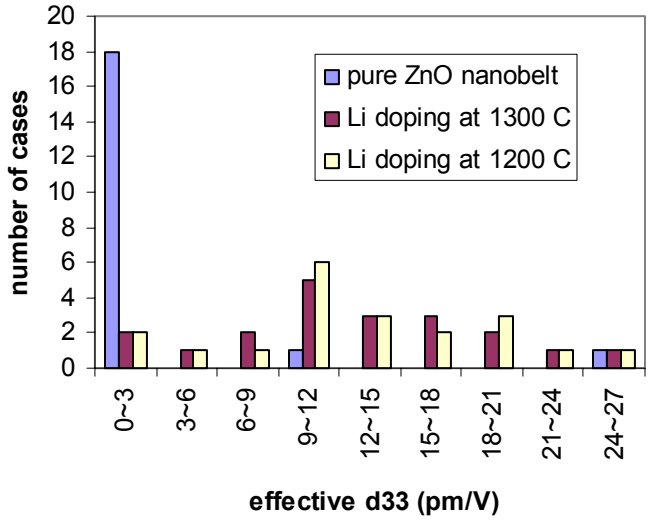

Figure 5.10 Distribution of 20 sets of data on the piezoelectric coefficient measurement of ZnO nanobelt with and without Li doping. The measurement frequency was set at 2 KHz.

5.2 FERROELECTRIC MEASUREMENT

As ferroelectric properties were reported in Li-doped ZnO thin film, it was interesting to find out if Li-doped ZnO nanobelt is ferroelectric. Li –doped ZnO nanobelts were prepared by thermal evaporation of zinc oxide and lithium carbonate (10 : 1 mol%) at 1300°C. After coating (100) Si wafer with a 100nm Pd, Li doped ZnO nanobelts were dispersed on the conductive surface similar to the way described previously . Next, the ZnO nanobelt was located by a commercially available AFM (Nanoscope IIIa, Multimode) under tapping mode. After locating the nanobelt, the tip (SSS-NCH by Nanoworld®, ~0.01 $\Omega \cdot$cm) was positioned still to the center of the nanobelt. Ferroelectric measurements on PZT thin film (prepared by sol-gel on Pt-coated Si, 1μm thick, serving as a reference sample for ferroelectric measurement) and Li-doped ZnO nanobelt were performed in contact mode at a single point with the addition of a signal access module (SBOB), a lock-in amplifier (SR850, Stanford Research Systems) and a DC voltage source. The contact force between AFM tip and nanobelt is ~1200nN, which ensures the measurement is in the so-called strong-indentation regime proposed by S.V. Kalinin and D.A. Bonnell [172], as the piezoresponse in the strong-indentation regime is dominated by the d_{33} of the material. A direct voltage pulse with duration of 12 seconds supplied by the DC source was applied to the tip with the Pd bottom electrode grounded to polarize the region underneath the tip. After the polarization, the tip was grounded and an AC voltage with a root-mean-square (rms) amplitude of 1V and a frequency of 2 kHz was applied to the bottom electrode.

Figure 5.11 is a phase sensitive piezoelectric amplitude image on a bare and polarized PZT thin film. The phase sensitive piezoresponse image (X output) clearly shows inverse contrast after 20V and –20 V polarizations.

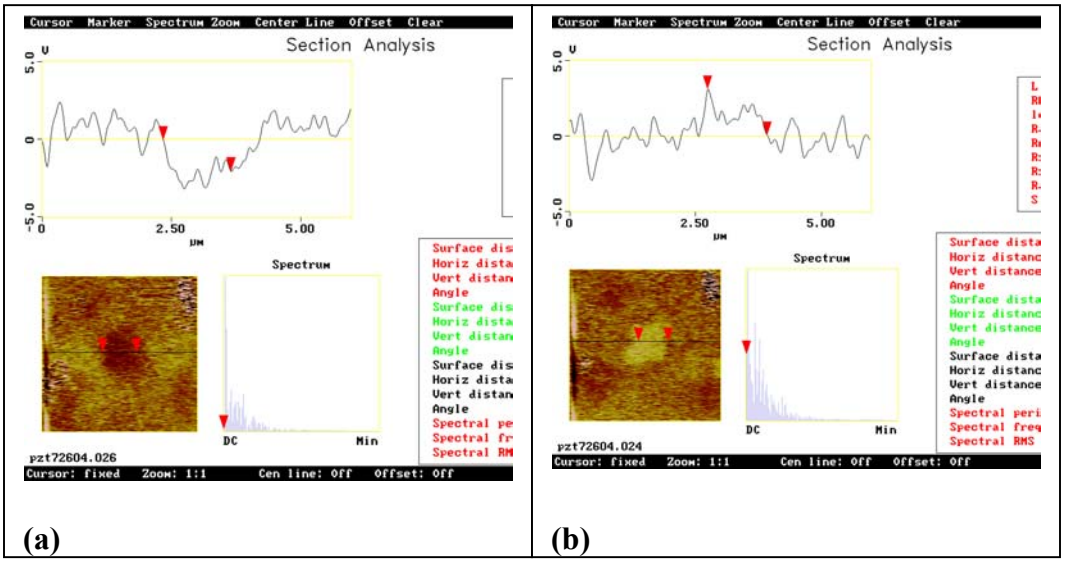

Figure 5.11 Phase sensitive piezoelectric amplitude image on a bare and polarized PZT thin film. The scan size for polarization is 1μm×1μm. (a) After 20V polarization. (b) After –20V polarization.

The tip vibration amplitude was equal to the product of the lock-in signal and the AFM detector sensitivity. The detector sensitivity was derived from the slope of several force-distance plots on hard surface such as sapphire. The piezoresponse d_{33} was equal to the tip vibration amplitude divided by the modulation voltage of 1V. By varying the DC polarization voltage, the piezoresponse d_{33} versus polarizing voltage hystersis curve (Figure 5.12) was obtained. These results confirmed the validity of our AFM-based ferroelectric measurement.

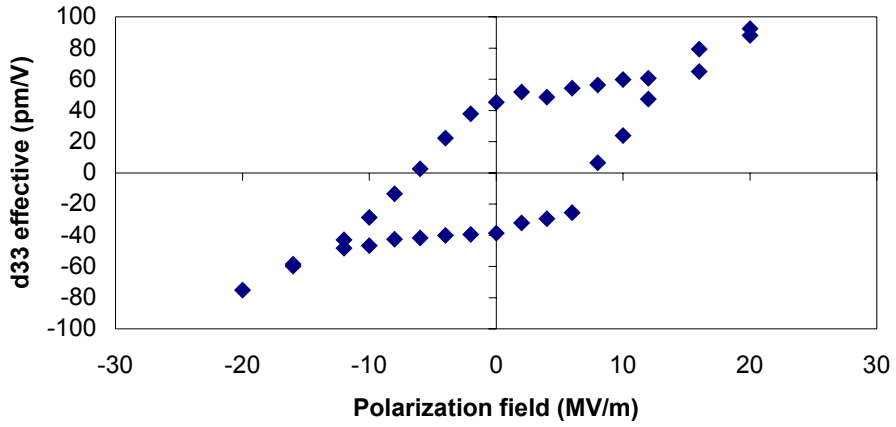

Figure 5.12 Piezoresponse d_{33} versus polarizing voltage hystersis curve on PZT thin film

However, we have not got the convinced results yet showing ferroelectric properties in Li-doped ZnO nanobelt. This may be due to the insufficient Li content in the ZnO sample. As shown in Figure 5.13, a new ferroelectric phase transition in $Zn_{1-x}Li_xO$ was possible at 330k only when x>0.06. The Curie temperature also increases with increasing Li molar ratio. Although 10% Li was mixed in the raw material, the actual Li concentration in ZnO nanobelt might still below 6%. This might due to the melting temperature of Li_2CO_3 (618°C) is much lower than that of ZnO (1975°C). A large amount of Li was lost before the decomposition of ZnO, which results in insufficient amount of Li doping in ZnO. Therefore, higher melting temperature Li compound, such as LiF, should be used in doping instead of Li_2CO_3.

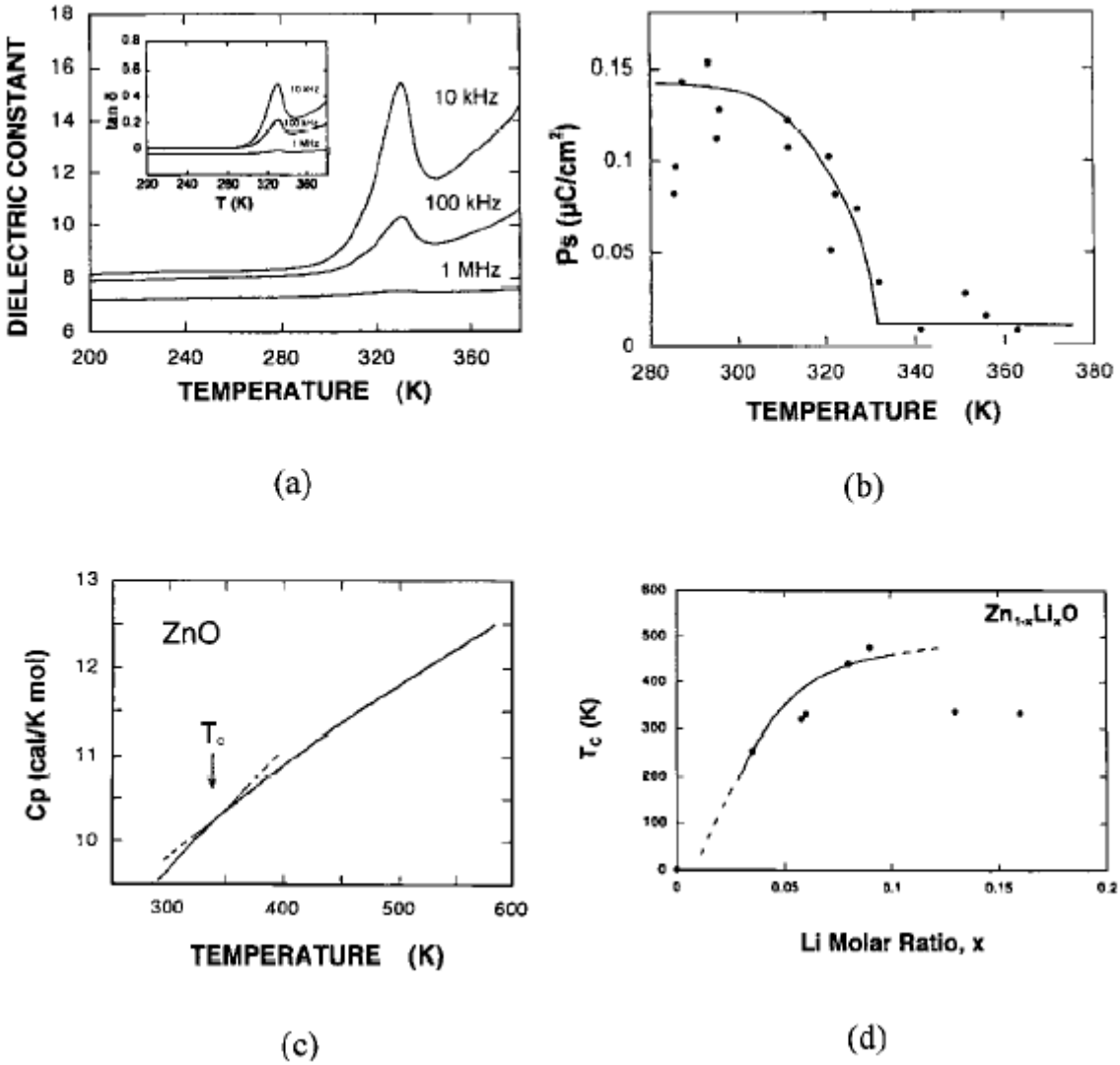

Figure 5.13 Dielectric properties of ZnO; (a) dielectric constant, (b) spontaneous polarization, (c) specific heat, (d) Curie temperature, T_c, versus Li molar ratio, x. [155]

6.0 UV PHOTODETECTOR BASED ON SINGLE ZNO NANOBELT

6.1 INTRODUCTION

A photodetector is an optoelectronic device that absorbs optical energy and converts it to electric energy, which usually manifest as a photocurrent. There are generally three steps involves in the photodetection process: (1) absorption of optical energy and generation of carriers; (2) transportation of the photogenerated carriers across the absorption and/or transit region, and (3) carriers collection and generation of a photocurrent, which flows through external circuitry.

Photodetectors are classified into intrinsic and extrinsic types. An intrinsic photodetector usually detects light of wavelength close to the bandgap of the semiconductor. Photo excitation creates electron-hole pairs, which contribute to the photocurrent. An extrinsic photodetector detects light of energy smaller than the bandgap energy. In these devices the transition corresponding to the adsorption of photos involves deep impurity and defect levels within the bandgap.

ZnO is a wide band-gap (3.37eV) compound semiconductor that is suitable for ultraviolet (UV) photo detection. Its high radiation hardness enables it to be used in harsh environment. ZnO UV detector is expected to be found in many applications, such as solar UV radiation monitoring, ultra-high temperature flame detection, and airborne missile warning systems, etc. For instance, ZnO thin film was reported to be a UV photodetector [180].

It is known that oxygen chemisorption and photodesorption plays a critical role on regulating the photosensitivity of bulk or thin film ZnO, where a UV sensitivity of similar

magnitude has been observed [181]. However, chemisorption and photodesorption are slow processes, which were dominant in polycrystalline ZnO due to multiple grain boundaries and surfaces. So the response speed of a polycrystalline ZnO UV detector is usually slow (Figure 6.1). As ZnO nanobelt is perfect single crystalline and almost free of defect, it is expected to have a fast response speed.

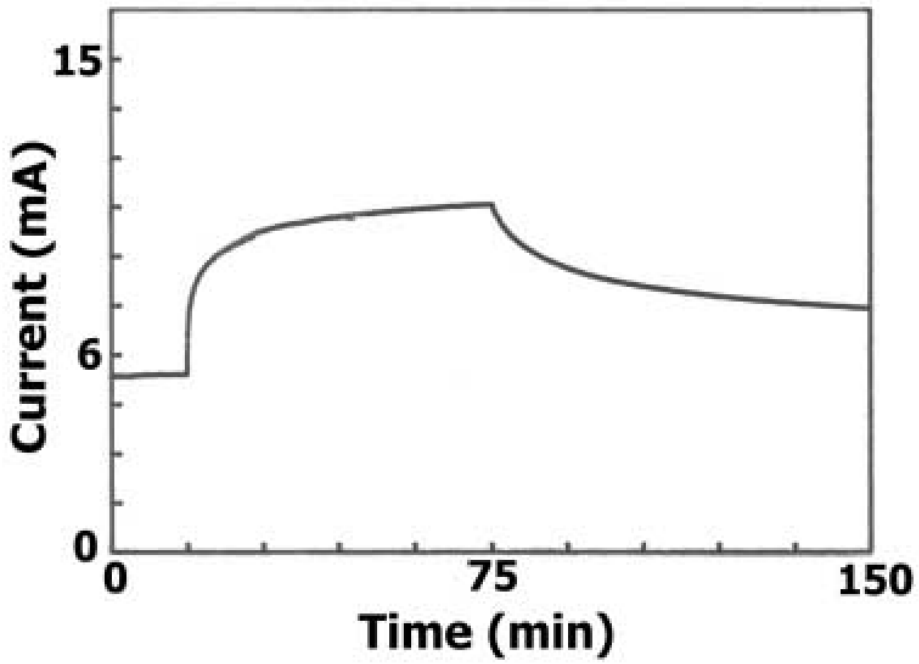

Figure 6.1 Temporal response of a thin film ZnO UV photodetector [182]

6.2 EXPERIMENTAL DESCRIPTION

In this study, we constructed a UV photodetector based on a single ZnO nanobelt. First, ZnO nanobelts prepared by thermal evaporation without addition were dispersed on the pre-patterned Pt electrodes similar to the aforementioned procedures. The Pt electrodes were connected to the external circuits by micro bonding. Data acquisition and control of the current and voltage were done simultaneously with Gamry electrochemical measurement system. Figure 6.2 shows the UV photodetector composed of a single ZnO nanobelt between the two Pt electrodes. Next, under constant 2.5V DC voltage, the current versus time (I-t) curves were recorded with the periodic light on and off. Two kinds of the light source are used. One is 8 watts UV source (254nm); the other is 7.5 watts soft –white light bulb. The illumination intensity is approximately 50 mW/cm^2.

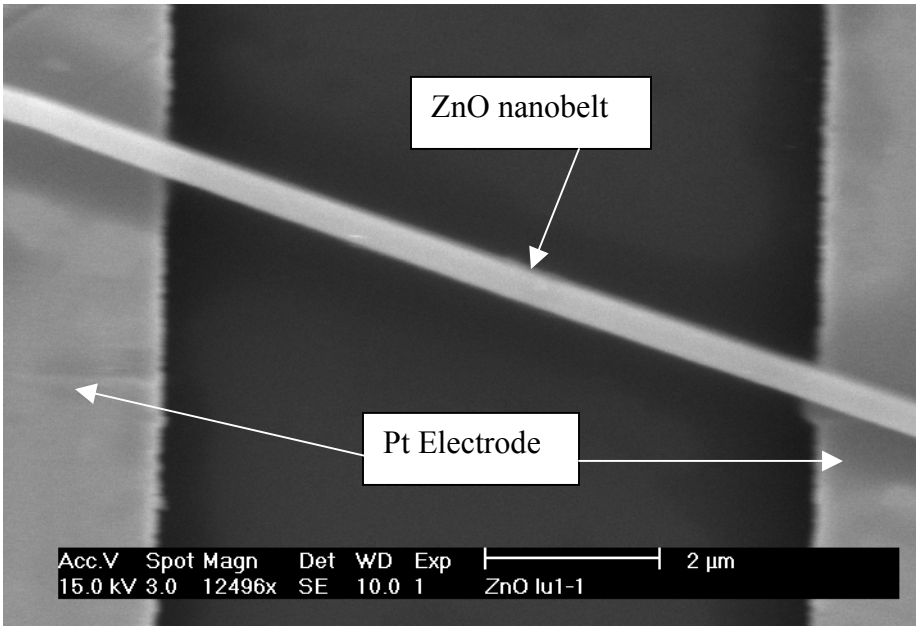

Figure 6.2 UV photodetector based on a single ZnO nanobelt between two Pt electrodes

6.3 RESULTS AND DISCUSSION

Figure 6.3 shows the response of the photodetector under UV and white light illumination. Fast response and recovery speed, high sensitivity and selectivity to UV light are demonstrated. The response and recovery time is only several seconds in comparison to the thin film UV photodetector (Figure 6.1). The increase of the photo current as high as 5 orders by UV illumination demonstrates its high sensitivity to UV, while 2 orders increase of the photo current by the same power white light illumination indicates its high selectivity to the UV spectrum, as the white light contains less than 0.1% UV spectrum. This behavior shows it is an intrinsic UV photodetector.

It is generally accepted that oxygen chemisorption play an important role in enhancing photosensitivity of bulk or thin film ZnO. Considering the high surface to volume ratio in ZnO nanobelt, further enhancement to the sensitivity of photo response of ZnO nanobelt is expected. It was generally believed that the photo response of ZnO consists of two parts: a solid-state process by which an electron and a hole are created ($h\upsilon \rightarrow h^+ + e^-$) and a two-step process involving oxygen species adsorbed on the surface. In the dark, oxygen molecules adsorb on the oxide surface as a negatively charged ion by capturing free electrons of the n-type oxide semiconductor ($O_2(g) + e^- \rightarrow O_2^-(ad)$) thereby creating a depletion layer with low conductivity near the nanowire surface. Upon exposure to UV light, photo-generated holes migrate to the surface and discharge the adsorbed oxygen ions ($h^+ + O_2^-(ad) \rightarrow O_2(g)$) through surface electron-hole recombination. Meantime, photo-generated electrons destruct the depletion layer, which results in the significant increase of the conductivity of the ZnO nanobelt.

In conclusion, the UV photodetector based on a single ZnO nanobelt is highly sensitive and selective to UV light with fast response speed. It is very promising to serve as ultra sensitive UV photodetector in many applications such as microanalysis and missile plume detection, as well as fast switching devices for nanoscale optoelectronic applications where on and off states can be addressed optically.

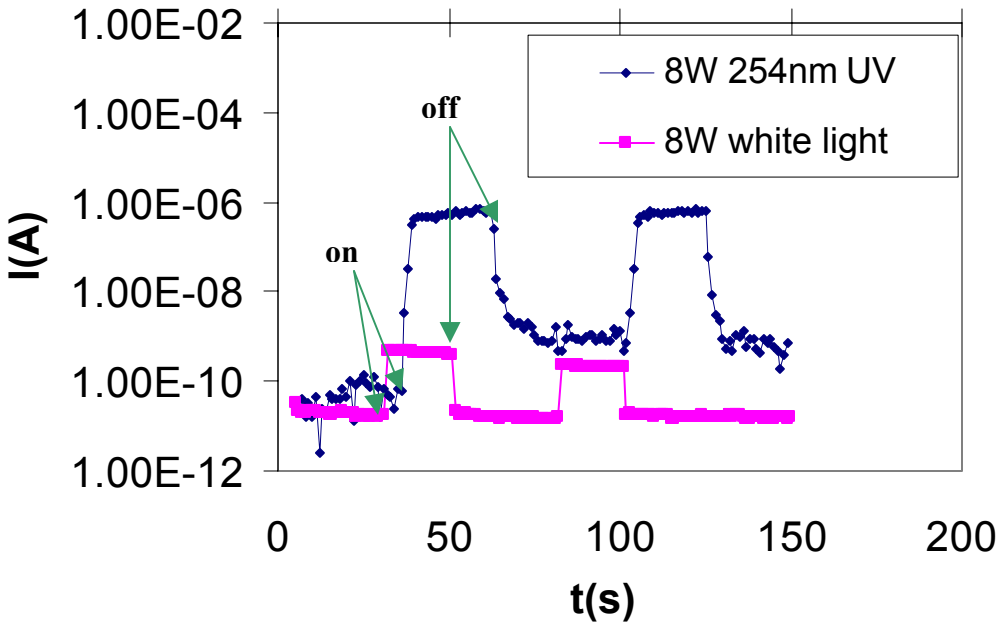

Figure 6.3 Temporal response of the single ZnO nanobelt UV photodetector under UV and white light illumination. Fast response and recovery speed, high sensitivity and selectivity to UV light are demonstrated.

7.0 CONCLUSIONS AND OUTLOOK

7.1 CONCLUSIONS

In this study, we revealed the following unique nanomechanical and electromechanical properties of a single ZnO nanobelt using Atomic Force Microscopy.

(i) The elastic modulus, hardness and fracture toughness of the ZnO nanobelt are much smaller than its bulk counterpart.

(ii) Strong photoinduced elastic effect is observed in ZnO nanobelt, while there is no effect in its bulk counterpart.

(iii) The effective piezoelectric coefficient, d_{33}, of ZnO nanobelt is frequency dependent and much higher than that of its bulk counterpart.

With thickness of tens to hundreds of nanometers, ZnO nanobelt is too small for the macro scale theory such as continuum mechanics, while it is too large for atomic scale theory such as quantum mechanics. Surface effects may play an important role in the unique properties of ZnO nanobelt thanks to its high surface to volume ratio. One of the consequences of our findings is that these properties are fundamental to the real applications. For instance, the strong photoinduced elastic effect in ZnO nanobelt sheds light on the realization of optical tunable surface acoustic wave devices. The excellent piezoelectric properties of ZnO nanobelts support their applications as nanosensors and nanoactuators.

7.2 OUTLOOK

ZnO nanostructures are attracting more research efforts worldwide. Using a solid –vapor phase thermal sublimation technique, nanocombs, nanorings, nanohelixes/nanosprings, nanobelts, nanowires and nanocages of ZnO have been synthesized under specific growth conditions. These unique nanostructures clearly demonstrate that ZnO probably has the richest family of nanostructures among all materials, both in structures and properties. Future work on the synthesis of 1D ZnO nanostructures is mainly focus on the following two aspects. One is the controlled growth of 1D ZnO nanostructure. The other is functionalizing the 1D ZnO nanostructure by doping and surface modification. As to the nanomechanical and electromechanical characterization on 1D ZnO nanostructures using AFM, the optical resolution of the CCD camera is a bottleneck in the investigation. The nanobelt which can be located optically is mainly in the thickness of several hundred nanometers. This makes the study of size effects on the properties of ZnO nanobelt extremely difficult. In addition, nano devices based on a single ZnO nanobelt seem promising in the near future.

APPENDIX A

A.1 PROCEDURES FOR CONVERTING FORCE CURVES OF NANOSCOPE AFM

In many cases, it is desirable to replace the "tip deflection versus z scanner position" curve to "force versus sample displacement" curve. The latter one is often more useful for comparing the measurements with theory because they show directly the dependence of the force on distance between the tip and sample. However, no procedures for the converting are disclosed in the Nanoscope AFM manual. The procedures are outlined as follows.

(1) Export the "tip deflection versus z scanner position curve" in ASCII format. Go to "utilities" choose "ASCII export". Remember to include the head of the file.

(2) Open the ASCII file using delimited width format by spreadsheet software, such as excel. The opened file consists of two parts. The first part (normally row 1 to row 291) is the head of the file, which contains information of the original file name and the experimental parameters. The second part is an one column data, showing the LSB value of the tip deflection voltage. Normally there will be 1024 (for 512 data points setting) or 512 (for 256 data points setting) sets of data. The first half is for extending cycle and the second half is for retracting cycle. Multiplying this value by the Sens. Deflection (included in the first part of the file, in unit of V/LSB) and deflection sensitivity (determined by the slope of the force curve on the hard surface such as sapphire, in units of nm/V) and the spring constant of the cantilever (in units of N/m) gives the deflection of the tip in units of nN. List these results as column 2.

(3) List the z scanner position in column 3. Starting with the zero for the first row. The value of the second row was the sum of the first row and the step value. The step value is derived as follows. First multiply the Sens. Zscan (in units of nm/V) by the ramp size (in units of voltage) and then divide the product by the number of the steps in the measurement ("511" for 512 data points and "255" for 256 data points). Repeat the step until the contact point of the extending cycle. It is critical to determine the contact point to the sample in this column, as the deflection value at the extending contact point is not necessary zero due to other types of force existed in the system. A good tactic for determining the contact point is to carefully examine the data in the column 1 from the first row. In the contact range, the data should be decreasing sharply all the time. The first data point where the data almost keep constant is defined as the contact point. The corresponding z scanner movement is defined as contact displacement.

(4) Column 4 is listed as the sample displacement. The value from the first row until the extending contact point is determined by the contact displacement minus the z scanner movement (value in column 3) and minus the cantilever deflection (column2 divided by the cantilever spring constant). As to the retracting cycle, the first row is the one with the largest value after a number of continuous zero. The value of column 4 in the first row is equal to that of the first row in the extending cycle. Repeat this to the following row in the retracting cycle until the deflection force in column 2 becomes zero or almost zero. The corresponding value in column 4 is regarded as the final displacement of the sample.

A.2 DETERMINATION OF TIP RADIUS USING AFM

Determination of tip radius is very critical to nanoindenter and AFM application. Normally, the sharper tips will provide more plastic deformation while keeping the elastic zone to a minimum. Hertzian elastic analysis is applicable as long as the contact region is elastic regardless of the geometry of the tip. The principle of the analysis is given by Equation (A.1).

$$F = \frac{4}{3} E^* R^{1/2} h^{3/2} \tag{A.1}$$

$$E^* = \left(\frac{1}{E_s} + \frac{1}{E_i}\right)^{-1} \tag{A.2}$$

Where F is the indentation load, E^* is the effective modulus of the indenter sample system, given by Equation (A.2), E_s and E_i are the elastic modulus for the sample and indenter respectively. R is the tip radius and h is the indentation depth.

The analysis starts from the indentation on the sample with well-known elastic modulus. Usually it is fused quartz with elastic modulus of 69.6 GPa. Extra care should be taken to make sure the contact is elastic. That is, no residual indent is observable after indentation. Once $F - h$ curve is derived, the tip radius is deduced by one parameter fitting to the $F - h$ curve. Figure A.1 and Figure A.2 are $F - h$ nanoindentation curves on fused quartz by cube corner indenter and AFM cantilever indenter respectively. The fitting results give the radius of the cube corner tip is 380nm and AFM cantilever tip is 18nm.

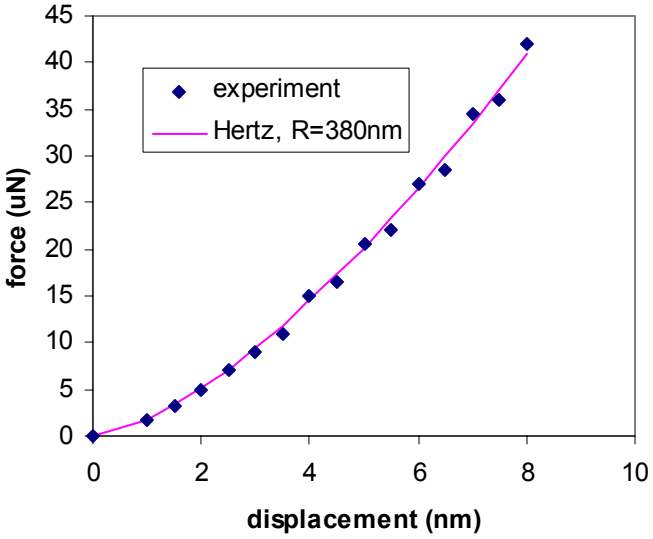

Figure 7.1 Force –displacement curve of nanoindentation on fused quartz by cube corner indenter

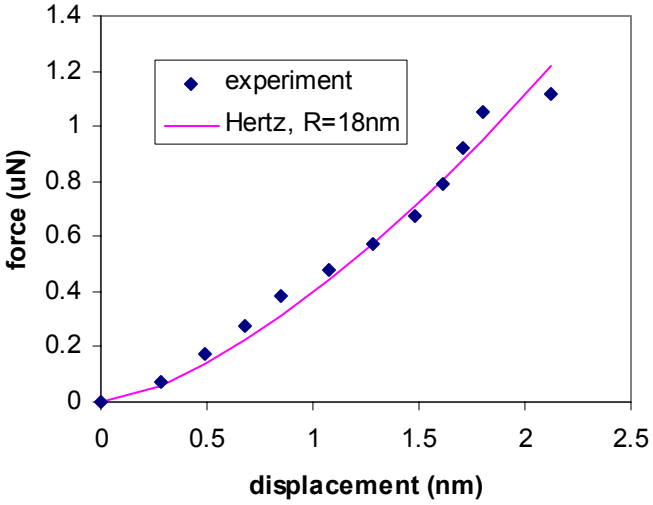

Figure 7.2 Force –displacement curve of nanoindentation on fused quartz by AFM cantilever indenter

A.3 ELASTIC CONSTANTS OF ZNO

Table 7.1 Calculated and experimental elastic constants of ZnO (Mbar) [111]

	Calculation		
	LDA	GGA	Experiment
C_{11}	2.09	2.30	2.096[a], 2.070[b]
C_{12}	0.85	0.82	1.211[a],1.177[b]
C_{13}	0.95	0.64	1.051[a], 1.061[b]
C_{33}	2.70	2.47	2.109[a], 2.095[b]
C_{55}	0.46	0.75	0.425[a], 0.448[b]
Bulk modulus[c]	1.38	1.25	1.436[a], 1.426[b]

[a] T.B. Bateman, J. Appl. Phys. **33**, 3309 (1962).

[b] I.B. Kaobiakov, Solid State Commun. **35**, 305 (1980).

[c] The bulk modulus is calculated from the elastic constants using the following relation:

$$B = \frac{2}{9}(C_{11} + C_{12} + 2C_{13} + C_{33}/2).$$

BIBLIOGRAPHY

1. Pan, Z.W., Dai, Z.R., Wang, Z.L., *Nanobelts of semiconducting oxides.* Science, 2001. **291**: p. 1947-1949.

2. Wang, Z.L., *Nanostructures of ZnO oxide.* Materials Today, 2004. **7**(6): p. 26-33.

3. Wang, Z., *Zinc oxide nanostructures: growth, properties and applications.* J. Phys.: Condens. Matter, 2004. **16**: p. R829-858.

4. Wang, Z., *Functional oxide nanobelts: materials, properties and potential applications in nanosystems and biotechnology.* Annu. Rev. Phys. Chem., 2004. **55**: p. 159-96.

5. Wang, Z., *Nanobelts of semiconductive oxides: a structurally and morphologically controlled nanomaterials system.* International Journal of Nanoscience, 2002. **1**: p. 41-51.

6. Dai, Z.R., Pan, Z.W., and Wang, Z.L., *Novel nanostructrues of functional oxides synthesized by thermal evaporation.* Adv. Funct. Mater., 2003. **13**: p. 9-24.

7. Wang, Z.L., *Nanobelts, nanowires, and nanodiskettes of semiconducting oxides-from materials to nanodevices.* Adv. Mater., 2003. **15**: p. 432-436.

8. Wang, Z.L., *Properties of nanobelts and nanotubes measured by in-situ TEM.* Microsc. Microanal., 2004. **10**: p. 158-166.

9. Xia, Y.N. and et al., *One-Dimensional Nanostructures: Synthesis, Characterization and Applications.* Adv. Mater., 2003. **15**(5): p. 353-389.

10. Lao, J.Y., Wen, J.G. , and Ren, Z.F., *Hierarchial ZnO Nanostructures.* Nano Lett., 2002. **2**(11): p. 1287-1291.

11. Zapien, J.A. and et al., *Room-temperature single nanoribbon lasers.* Appl. Phys. Lett., 2004. **84**: p. 1189-1191.

12. Comini, E., Faglia, G., Sberveglieri, G., Pan, Z.W., and Wang, Z.L., *Stable and highly sensitive gas sensors based on semiconducting oxide nanobelts.* Appl. Phys. Lett., 2002. **81**: p. 1869-1871.

13. Hughes, W.L., and Wang, Z.L., *Nanobelts as nanocantilevers.* Appl. Phys. Lett., 2003. **82**: p. 2886-2888.

14. Arnold, M.S., Avouris, P. , Pan, Z.W., and Wang, Z. L., *Field-Effect Transistors Based on Single Semiconducting Oxide Nanobelts.* J. Phys. Chem. B, 2002. **107**(3): p. 659-663.

15. Bai, X.D., Wang, E.G., Gao, P.X., Wang, Z.L., *Dual-mode mechanical resonance of individual ZnO nanobelts.* Appl. Phys. Lett., 2003. **82**: p. 4806-4808.

16. Carcia, P.F. and et al., *ZnO thin film transistors for flexible electronics.* Mater. Res. Soc. Symp. Proc., 2003. **769**: p. H.7.2.1-H.7.2.6.

17. Look, D.C., *recent advances in ZnO materials and devices.* Mater. Sci. & Eng. B, 2001. **80**: p. 383-387.

18. Nahhas, A., and Kim, H.K., *Epitaxial growth of ZnO films on Si substrates using an epitaxial GaN buffer.* Appl. Phys. Lett., 2001. **78**: p. 1511-1513.

19. Norton, D.P., Heo Y.W. , Ivill, M.P. , IP, K. , Pearton, S.J. , Chisholm, M.F. ; and Steiner, T., *ZnO: growth, doping and processing.* Materials Today, 2004. **7**(6): p. 34-40.

20. Ohgaki, T. and et al., *Electrical and optical properties of zinc oxide thin films and heavily aluminum-doped zinc oxide thin films prepared by Molecular beam epitaxy.* Mater. Res. Soc. Symp. Proc., 2003. **744**: p. M5.1.1-M5.1.6.

21. Ohta, H., and Hosono, H., *Transparent oxide optoelectronics.* Materials Today, 2004. **7**(6): p. 42-51.

22. Roy, S., and Basu, S., *Improved zinc oxide film for gas sensor applications.* Bull. Mater. Sci., 2002. **25**: p. 513-515.

23. Shibata, T., Unno, K. , Makino, E. , Ito, Y., Shimada, S., *Characterization of sputtered ZnO thin film as sensor and actuator for diamond AFM probe.* Sensors and Actuators A, 2002. **102**: p. 106-113.

24. Biswas, S.K., Schujman, S.B., Vajtai, R., Wei, B.Q., Parker, A., Schowalter, L.J., and Ajayan, P.M., *AFM-based electrical characterization of nano-structures.* Mater. Res. Soc. Symp. Proc., 2003. **738**: p. G9.2.1-G9.2.7.

25. Indermuhle, P.-F., Schurmann, G, Racine, G-A, and Rooij, N F de, *Atomic force microscopy using cantilevers with intergrated tips and piezoelectric layers for actuation and detection.* J. Micromech. Microeng., 1997. **7**: p. 218-220.

26. Shao, R., Kalinin, S.V., and Bonnell, D.A., *Nanoimpedance microscopy and spectroscopy.* Mater. Res. Soc. Symp. Proc., 2003. **738**: p. G4.4.1-G4.4.6.

27. Burnham, N.A., Colton, R.J., *Measuring the nanomechanical properties and surface forces of materials using atomic force microscope.* J. Vac. Sci. Technol. A, 1989. **7**: p. 2906-2913.

28. Kimitake, F., Kawai, S., Saya, D., and Kawakatsu, H., *Measurement of mechanical properties of three-dimensional nanometric objects by an atomic force microscope incorporated in a scanning electron microscope.* Rev. Sci. Instr., 2002. **73**: p. 2647-2650.

29. Borovsky, B., Krim, J., Asif, S.A.S, Wahl, K.J., *Measuring nanomechanical properties of a dynamic contact using an indenter probe and quartz crystal microbalance.* J. Appl. Phys., 2001. **90**: p. 6391-6396.

30. Fraxedas, J., Garcia-Manyes, S., Gorostiza, P., Sanz, F, *Nanoindentation: Toward the sensing of atomic interactions.* PNAS, 2002. **99**: p. 5228-5232.

31. Tombler, T.W. and et al., *Reversible electromechanical characteristics of carbon nanotubes under local-probe manipulation.* Nature, 2000. **405**: p. 769-772.

32. Asif, S.A.S., Wahl, K.J., Colton, R.J., Warren O.L., *Quantitative imaging of a nanoscale mechanical properties using hybrid nanoindentation and force modulation.* J. Appl. Phys., 2001. **90**: p. 1192-1200.

33. Garcia-Manyes, S., Gorostiza, P., and Sanz, F. *Nanoindentation: from forces to energies*. in *Mat. Res. Symp. Proc.* 2003.

34. Sundararajan, S. and Bhushan, B., *Development of AFM-based techniques to measure mechenical properties of nanoscale structures.* Sensors and Actuators A, 2002. **101**: p. 338-351.

35. Espinosa, H.D., Porok, B.C., and Fischer, M., *A methodology for determining mechanical properties of free standing thin films and MEMS materials.* J. Mech. Phys. Solids, 2003. **51**: p. 47-67.

36. Wong, E.W., Sheehan, P.E., and Lieber, C.M., *Nanobeam mechanics: elasticity, strength, and toughness of nanorods and nanotubes.* Science, 1997. **277**: p. 1971-1975.

37. Zhao, M.H., Wang, Z.L., and Mao, S.X., *Piezoelectric characterization of individual zinc oxide nanobelt probed by piezoresponse force microscope.* Nano Lett., 2004. **4**: p. 587-590.

38. Mao, S.X., Zhao, M.H., and Wang, Z.L., *Nanoscale mechanical behavior of individual semiconducting nanobelts.* Appl. Phys. Lett., 2003. **83**: p. 993-995.

39. Wang, Z.L., *Nanowires and nanobelts: materials, properties and devices*. Vol. volume 2: Nanowires and nanobelts of functional materials. 2003: Kluwer Academic Publishers.

40. Shao, R., Kalinin, S.V., and Bonnell, D.A., *Local impedance imaging and spectroscopy of polycrystalline ZnO using contact atomic force microscopy.* Appl. Phys. Lett., 2003. **82**: p. 1869-1871.

41. Chen, Y.Y. and et al., *Analysis of the frequency response of a dispersive IDT/ZnO/sapphire SAW filter using effective permittivity and the coupling of modes model.* J. Phys. D: Appl. Phys., 2004. **37**: p. 120-127.

42. Huang, M.H. and Wu, Y.Y., et al, *Catalytic growth of zinc oxide nanowires by vapor transport.* Adv. Mater., 2001. **13**: p. 113-116.

43. Vayssieres, L., *Growth of arrayed nanorods and nanowires of ZnO from aqueous solutions.* Adv. Mater., 2003. **15**: p. 464-466.

44. Xu, C., et al., Scripta Mater, 2003. **48**: p. 1367.

45. Hu, J.Q.L., Q.; Meng, X.M.; Lee, C.S.; Lee, S.T., Chem. Mater., 2003. **15**: p. 305.

46. Park, W.I., et al., *Metalorganic vapor-phase epitaxial growth of vertically well-aligned ZnO nanorods.* Appl. Phys. Lett., 2002. **80**(22): p. 4232-4234.

47. Chen, Z., et al., *Effect of N2 flow rate on morphology and structure of ZnO nanocrystals synthesized via vapor deposition.* Scripta Mater, 2005. **52**: p. 63-67.

48. Dai, Y., et al., Chem Phys Lett, 2002. **358**: p. 83.

49. Yan, H.Q., et al., Adv. Mater., 2003. **15**: p. 402.

50. Tang, C.C., Chem Phys Lett, 2001. **333**: p. 12.

51. Roy, V. and et al., Appl. Phys. Lett., 2003. **82**: p. 141.

52. Vanheusden, K. and et al., J. Appl. Phys., 1996. **79**: p. 7983.

53. Wang, Y.G. and et al., J. Appl. Phys., 2003. **94**: p. 354.

54. Dai, L. and et al., J. Phys: Condens Mater, 2003. **15**: p. 2221.

55. Zhang, D.H., Xue, Z.Y., and Wang, Q.P., J. Phys. D.: Appl. Phys, 2002. **35**: p. 2837.

56. Bachari, E.M., et al., Thin Solid Films, 1999. **348**: p. 165.

57. Lin, B.X., Fu, Z.X., and Jia, Y.B., Appl. Phys. Lett., 2001. **79**: p. 943-945.

58. Im, S., Jin, B.J., and Yi, S., J. Appl. Phys., 2000. **87**: p. 4558.

59. Wang, Q.P., Zhang, D.H., and et al., Appl Surf Sci, 2003. **220**: p. 12.

60. Zhang, Y., Wang, N., and Gao, S., Chem Mater, 2002. **14**: p. 3564.

61. Bonnell, D., *Scanning Probe Microscopy and Spectroscopy: Theory, Techniques, and Applications*. 2nd Edition ed. 2000.

62. *Applied Scanning Probe Methods*. Nanoscience and Technology, ed. Bhushan, B.F., Harald; Hosaka, Sumio. 2004: Springer.

63. Zhang, J. and et al., *Determination of the Ionisation State of 11-Thioundecyl-1-Phosphate in Self-Assembled Monolayers by Chemical Force Microscopy.* Anal. Chem., 2000. **72**: p. 1973-1978.

64. Prater, C.B., et al., *Probing nano-scale forces with the atomic force microscope*. 1998, Digital Instruments.

65. ZELENKA, J., *Piezoelectric Resonators and their Applications*. 1986, ELSEVIER.

66. LaHaye, M.D., et al., *Approaching the quantum limit of a nanomechanical resonator.* Science, 2004. **304**: p. 74-77.

67. Badzey, R.L., et al., *A controllable nanomechanical memory element.* Appl. Phys. Lett., 2004. **85**: p. 3587-3589.

68. Carlotti, G. and Socino, G., *Acoustic Investigation of the elastic properties of ZnO films.* Appl. Phys. Lett., 1987. **51**: p. 1889-1891.

69. Wang, Z.L., *Mechanical properties of nanowires and nanobelts*, in *Encyclopedia of Nanoscience and Nanotechnology*. 2004, Marcel Dekker: New York. p. 1773-1786.

70. Wang, Z.L., et al., *Nanoscale mechanics of nanotubes, nanowires and nanobelts.* Adv. Engr. Mater., 2001. **3**: p. 657-661.

71. Hues, S.M., Draper, C.F., and Colton, R.J., *Measurements of nanomechanical properties of metals using the atomic force microscope.* J. Vac. Sci. & Tech. B, 1994. **12**: p. 2211-2214.

72. Chizhik, S.A., et al., *Micromechnical properties of elastic polymeric materials as probed by scanning force microscopy.* Langmuir, 1998. **14**: p. 2606-2609.

73. Akhremitchev, B.B. and Walker, G.C., *Finite sample thickness effects on elasticity determination using atomic force microscopy.* Langmuir, 1999. **15**: p. 5630-5634.

74. Wang, Y.G., et al., *Measurement of the fracture toughness and critical stress for cracking in SnO2 nanobelts using nanoindentation.* ACTA Metallurgica Sinica, 2004. **40**: p. 594-598.

75. Marszalek, P.E., et al., *Atomic force microscopy captures quantized plastic deformation in gold nanowires.* PNAS, 2000. **97**: p. 6282-6286.

76. Stalder, A. and Durig, U., *Study of plastic flow in ultrasmall Au contacts.* J. Vac. Sci. & Tech. B, 1996. **14**: p. 1259-1263.

77. Giannakopoulos, A.E. and Suresh, S., *Determination of elastoplastic properties by instrumented sharp indentation.* Scripta Mater, 1999. **40**: p. 1191-1198.

78. Wolf, B., *Inference of mechanical properties from instrumented depth sensing indentation at tiny loads and indentation depths.* Cryst. Res. Technol., 2000. **35**: p. 377-399.

79. Vanlandingham, M.R., *Review of Instrumented Indentation.* J. Res. Natl. Inst. Stand. Technol., 2003. **108**: p. 249-265.

80. Cheng, Y.T. and Cheng, C.M., *Scaling, dimensional analysis, and indentation measurements.* Mater. Sci. & Eng. R, 2004. **44**: p. 91-149.

81. Franco, A.R. and et al., *The use of a vickers indenter in depth sensing indentation for measuring elastic modulus and vickers hardness.* Mater. Res., 2004. **7**: p. 483-491.

82. Page, T.F., Oliver, W.C., and McHargue, C.J., *The deformation behavior of ceramic crystals subjected to very low load nanoindentations.* J. Mater. Res., 1992. **7**: p. 450-473.

83. Pharr, G.M., *Measurement of mechanical properties by ultra-low load indentation.* Mater. Sci. & Eng. A, 1998. **253**: p. 151-159.

84. Li, X.D. and Bhushan, B., *A review of nanoindentation continuous stiffness measurement technique and its applications.* Materials Characterization, 2002. **48**: p. 11-36.

85. Pharr, G.M. and Bolshakov, A., *Understanding nanoindentation unloading curves.* J. Mater. Res., 2002. **17**: p. 2660-2671.

86. Wolf, B. and Richter, A., *The concept of differential hardness in depth sensing indentation.* New Journal of Physics, 2003. **5**: p. 15.1-15.17.

87. Oliver, W.C. and Pharr, G.M., *An improved technique for derermining hardness and elastic-modulus using load and displacement sensing indentation experiments.* J. Mater. Res., 1992. **7**: p. 1564-1583.

88. Doerner, M.F. and Nix, W.D., *A method for interpretating the data depth-sensing indentation instruments.* J. Mater. Res., 1986. **1**: p. 601-609.

89. Gerberich, W.W. and et al., *Elastic loading and elastoplastic unloading from nanometer level indentations for modulus determinations.* J. Mater. Res., 1998. **13**: p. 421-439.

90. ISO, *ISO/FDIS 14577-1. Metallic materials-Instrumented indentation test for hardness and material parameter, Part 1: Test method.* 2002: Geneve, Switzerland.

91. Sneddon, I.N., *The relation between load and penetration in the axisymmetric Boussinesq' problem for a punch of arbitrary profile.* International Journal of Science Engineering, 1965. **3**: p. 47-57.

92. King, R.B., *Elastic analysis of some punch problems for a layered medium.* International Journal of Solids Structures, 1987. **23**: p. 1657-1664.

93. *Hysitron Triboscope nanoindenter user manual*.

94. Pharr, G.M., Oliver, W.C., and Brotzen, F.R., *On the generality of the relationship among contact stiffness, contact area, and elastic modulus during indentation.* J. Mater. Res., 1992. **7**: p. 613-617.

95. Hardening, D.S., Oliver, W.C., and Pharr, G.M. in *Mater. Res. Soc. Symp. Proc.* 1995.

96. Lawn, B.R., Evans, A.G., and Marshall, D.B., J. Am. Ceram. Soc., 1980. **63**: p. 574.

97. Bhushan, B. and Li, X.D., Int. Mater. Rev., 2003. **48**: p. 125-164.

98. DeVoe, D.L. and Pisano, A., *Modelling and Optimal Design of Piezoelectric Cantilever Microactuators.* Journal of Microelectromechanical Systems,, 1997. **6**(3).

99. Wang, J.G., et al. *Nanoindentation and nanowear studies of sputter-deposited ultrathin tin oxide films on glass substrates*. in *Mater. Res. Soc. Symp. Proc.* 2002.

100. Kracke, B. and Damaschke, B., *Measurement of nanohardness and nanoelasticity of thin gold films with scanning force microscope.* Appl. Phys. Lett., 2000. **77**: p. 361-363.

101. Schaefer, D.M., et al., *Elastic properties of individual nanometer-size supported gold clusters.* Phys. Rev. B, 1995. **51**: p. 5322-5332.

102. Li, X.X., et al., *Ultrathin single-crystalline-silicon cantilever resonators: fabrication technology and significant specimen size effect on Young's modulus.* Appl. Phys. Lett., 2003. **83**: p. 3081-3083.

103. Liang, H.Y., Ni, X.G., and Wang, X.X., *Atomic simulation of tension properties of nano crystal copper wire under surface effects.* ACTA Metallurgica Sinica, 2001. **37**: p. 833-836.

104. Gouldstone, A., Vliet, K.J.V., and Suresh, S., *Simulation of defect nucleation in a crystal.* Nature, 2001. **411**: p. 656.

105. Gouldstone, A., et al., *Discrete and continuous deformation during nanoindentation of thin films.* Acta Materialia, 200. **48**: p. 2277-2295.

106. Gerberich, W.W. and et al., *Nanoindentation-induced defect-interface interactions: phenomena, methods and limitations.* Acta Materialia, 1999. **47**: p. 4115-4123.

107. S. Suresh, Nieh, T.-G., and Choi, B.W., *Nano-indentation of copper thin films on silicon substrates.* Scripta Mater, 1999. **41**: p. 951-957.

108. Gerberich, W.W., et al., *Indentation induced dislocation nucleation: the initial yield point.* Acta Materialia, 1996. **44**: p. 3585-3598.

109. *Hysitron Technical note: Measuring the radius of a curvature of a probe tip*. 1999.

110. Courtney, T.H., *Mechanical behavior of materials*. 1990: McGraw-Hill Publishing Company.

111. Ahuja, R., et al., *Elastic and high pressure properties of ZnO.* J. Appl. Phys., 1998. **83**: p. 8065-8067.

112. Zaoui, A. and Sekkal, W., *Pressure-induced softening of shear modes in wurtzite ZnO: A theoretical study.* Phys. Rev. B, 2002. **66**: p. 174106.

113. Limpijumnong, S. and Jungthawan, S., *First-principles study of the wurtzite-to-rocksalt homogeneous transformation in ZnO: A case of a low-transformation barrier.* Physical Review B, 2004. **70**(5).

114. Saitta, A.M. and Decremps, F., *Unifying description of the wurtzite-to-rocksalt phase transition in wide-gap semiconductors: The effect of d electrons on the elastic constants.* Physical Review B, 2004. **70**(3).

115. Decremps, F., et al., *Local structure of condensed zinc oxide.* Physical Review B, 2003. **68**(10).

116. Wu, Z.Y., et al., *Conductance and phase transition of freestanding ZnO nanocrystals under high pressure.* Materials Science and Technology, 2003. **19**(7): p. 981-984.

117. Manjon, F.J., Syassen, K., and Lauck, R., *Effect of pressure on phonon modes in wurtzite zinc oxide.* High Pressure Research, 2002. **22**(2): p. 299-304.

118. Decremps, F., et al., *High-pressure Raman spectroscopy study of wurtzite ZnO.* Physical Review B, 2002. **65**(9).

119. Kusaba, K., Syono, Y., and Kikegawa, T., *Phase transition of ZnO under high pressure and temperature.* Proceedings of the Japan Academy Series B-Physical and Biological Sciences, 1999. **75**(1): p. 1-6.

120. Sharma, S.K. and Exarhos, G.J., *Raman spectroscopic investigation of ZnO and doped ZnO films, nanoparticles and bulk material at ambient and high pressures.* Solid State Phenomena, 1997. **55**: p. 32-37.

121. Karzel, H., et al., *Lattice dynamics and hyperfine interactions in ZnO and ZnSe at high external pressures.* Physical Review B, 1996. **53**(17): p. 11425-11438.

122. Gerward, L. and Olsen, J.S., J. Synchrotron Radiat., 1995. **2**: p. 233.

123. Suito, K., Kawai, N., and Masuda, Y., Mater. Res. Bull., 1975. **10**: p. 677.

124. Lucca, D.A., et al., *Investigation of polished single crystal ZnO by nanoindentation.* CIRP Annals-Manu. Tech., 2002. **51**: p. 483-486.

125. Kucheyev, S.O., et al., *Mechanical deformation of single-crystal ZnO.* Appl. Phys. Lett., 2002. **80**: p. 956-958.

126. Saha, R., et al., *Indentation of a soft metal film on a hard substrate: strain gradient hardening effects.* J. Mech. Phys. Solids, 2001. **49**: p. 1997-2014.

127. Swadener, J.G., George, E.P., and Pharr, G.M., *The correlation of the indentation size effect measured with indenters of various shapes.* J. Mech. Phys. Solids, 2002. **50**: p. 681-694.

128. Gerberich, W.W., et al., *Interpretations of Indentation Size Effects.* J. Appl. Mech., 2002. **69**: p. 433-442.

129. Zhao, M.H., et al., *Materials-length-scale-controlled nanoindentation size effects due to strain-gradient plasticity.* Acta Materialia, 2003. **51**: p. 4461-4469.

130. Zhang, T.Y., Xu, W.H., and Zhao, M.H., *The role of plastic defrmation of rough surfaces in the size dependent hardness.* Acta Materialia, 2004. **52**: p. 57-68.

131. Bradby, J.E., et al., *Contact-induced defect propagation in ZnO.* Appl. Phys. Lett., 2002. **80**: p. 4537-4539.

132. Uchic, M.D., et al., *Sample dimensions influence strength and crystal plasticity.* Science, 2004. **305**: p. 986-989.

133. Choi, Y. and Suresh, S., *Nanindentation of patterned metal lines on a Si substrate.* Scripta Mater, 2003. **48**: p. 249-254.

134. Choi, Y., et al., *Size effects on the onset of plastic deformation during nanoindentation of thin films and patterned lines.* J. Appl. Phys., 2003. **94**: p. 6050-6058.

135. Bahr, D.F., Kramer, D.E., and Gerberich , W.W., Acta Mater, 1998. **46**: p. 3605.

136. Li, X.D., et al., *Nanoindentation on silver nanowires.* Nano Lett., 2003. **3**: p. 1495-1498.

137. Carlsson, L. and Svesson, C., *Increase of flow stress in ZnO under illumination.* Solid State Commun., 1969. **7**: p. 177-179.

138. Carlsson, L. and Svesson, C., *Photoplastic effect in ZnO.* J. Appl. Phys., 1970. **41**: p. 1652-1656.

139. Klopfstein, M.J., Lucca, D.A., and Cantwell, G., *Effects of illumination on the response of (0001) ZnO to nanoindentation.* phys. stat. sol, 2003. **196**: p. R1-R3.

140. Chu, S.Y., Chen, T.Y. & Water, W., *Deposition of preferred-orientation ZnO films on the ceramic substrates and its application for surface acoustic wave filters.* J. Vac. Sci. & Tech. A, 2004. **22**: p. 1087-1092.

141. Berkowicz, R. and Skettrup, T., *Brillouin scattering, piezobirefringence, and dispersion of photoelastic coefficients of CdS and ZnO.* Phys. Rev. B, 1975. **11**: p. 2316-2326.

142. Sasaki, H., Tsubouchi, K., and Mikoshiba, N., *Photoelastic effect in piezoelectric semiconductor: ZnO.* J. Appl. Phys., 1976. **47**: p. 2046-2049.

143. Azuhata, T. and et al., *Brillouin scattering study of ZnO.* J. Applied Phys., 2003. **94**: p. 968-972.

144. Domke, J. and Radmacher, M., *Measuring the elastic properties of thin polymer films with the atomic force microscope.* Langmuir, 1998. **14**: p. 3320-3325.

145. Soifer, Y.M. and Verdyan, A., *Investigation of the local mechanical properties of potassium chloride single crystals by atomic force microscopy.* Physics of the Solid State, 2003. **45**: p. 1701-1705.

146. Suresh, S., Nieh, T.G., and Choi, B.W., *Nano-indentation of copper thin films on silicon substrate.* Scripta Mater, 1999. **41**: p. 951-957.

147. Todorovic, D.M., Nikolic, P.M. & Bojicic, A.I., *Photoacoustic frequency transmission technique: Electronic deformation mechanism in semiconductors.* J. Appl. Phys., 1999. **85**: p. 7716-7718.

148. Stearns, R.G. and Kino, G.S., *Effect of electronic strain on photoacoustic generation in silicon.* Appl. Phys. Lett., 1985. **47**: p. 1048-1050.

149. Datskos, P.G., Rajic, S. & Datskou, I., *Photoinduced and thermal stress in silicon microcantilevers.* Appl. Phys. Lett., 1998. **73**: p. 2319-2321.

150. Segura, A., Sans, J.A., Manjon, F. J., Munoz, A. & Herrera-Cabrera, M. J., *Optical properties and electronic structure of rock-salt ZnO under pressure.* Appl. Phys. Lett., 2003. **83**: p. 278-280.

151. Caro, J., Fraxedas, F., Gorostiza, P. & Sanz, F., *Nanomechanical properties of molecular organic thin films.* J. Vac. Sci. Technol. A, 2001. **19**: p. 1825-1828.

152. Kind, H., Yan, H.Q., Messer, B., Law, M. & Yang, P.D., *Nanowire ultraviolet photodetectors and optical switches.* Adv. Mater., 2002. **14**: p. 158-160.

153. Heo, Y.W. and et al., *Electrical transport properties of single ZnO nanorods.* Appl. Phys. Lett., 2004. **85**: p. 2002-2004.

154. Keem, K. and et al., *Photocurrent in ZnO nanowires grown from Au electrodes.* Appl. Phys. Lett., 2004. **84**: p. 4376-4378.

155. Onodera, A., *Novel ferroelectricity in II-VI semiconductor ZnO.* Ferroelectrics, 2002. **267**: p. 131-137.

156. Onodera, A., et al., *Dielectric activity and ferroelectricity in piezoelectric semiconductor Li-doped ZnO.* Jpn. J. Appl. Phys., 1996. **35**: p. 5160-5162.

157. Onodera, A., et al., *Li-substitutution effect and feroelectric properties in piezoelectric semiconductor ZnO.* Jpn. J. Appl. Phys., 1998. **37**: p. 5315-5317.

158. Onodera, A., et al., *Li-induced ferroelectricity and its structural phase transisition in ZnO.* Ferroelectrics, 1999. **230**: p. 465-470.

159. Nagata, T. and et al., *Ferroelectrocity Li-doped ZnO: X thin films and their application in optical switching devices.* Jpn. J. Appl. Phys., 2001. **40**: p. 5615-5618.

160. Yoshio, K., et al., *Stal structure of ZnO: Li at 293K and 19K by X-ray diffraction.* Ferroelectrics, 2001. **264**: p. 1791-1796.

161. Hagino, S. and et al., *Electronic ferroelectricity in ZnO.* Ferroelectrics, 2001. **264**: p. 1893-1898.

162. Joseph, M., Tabata, H., and Kawai, T., *Ferroelectric behavior of Li-doped ZnO thin films on Si(100) by pulsed laser deposition.* Appl. Phys. Lett., 1999. **74**: p. 2534-2536.

163. Ni, H.Q. and et al., *Investigation of Li-doped ferroelectric and piezoelectric ZnO films by electric force microscopy and Raman spectroscopy.* Appl. Phys. Lett., 2001. **79**: p. 812-814.

164. Nagata, T., et al., *Electro-optic property of ZnO: X (X=Li, Mg) thin films.* J. Crystal Growth, 2002. **237**: p. 533-537.

165. Kong, X.Y. and Wang, Z.L., *Spontaneous polarization-induced nanohelixs, nanosprings, and nanorings of piezoelectric nanobelts.* Nano Lett., 2003. **3**: p. 1625-1631.

166. Winters, R., et al., J. Vac. Sci. Technol. B, 1995. **13**: p. 1316.

167. Zavala, G., Fendler, J.H., and Trolier-McKinstry, S., J. Appl. Phys., 1997. **81**: p. 7480.

168. Christman, J.A., et al., Appl. Phys. Lett., 1998. **73**: p. 3851.

169. Agronin, A.G., Rosenwaks, Y., and Rosenman, G., Nano Lett., 2003. **3**: p. 169.

170. Yun, W.S., et al., Nano Lett., 2002. **2**: p. 447.

171. Harnagea, C., et al., Appl. Phys. A, 2000. **70**: p. 261.

172. Kalinin, S.V. and Bonnell, D.A., Phys. Rev. B, 2002. **65**: p. 125408.

173. Dunn, S., Integrated Ferroelectrics, 2003. **59**: p. 1505.

174. Buhlmann, S., et al., Appl. Phys. Lett., 2002. **80**: p. 3195.

175. Li, J., Moses, P., and Viehland, D., Rev. Sci. Instrum., 1995. **66**: p. 215.

176. Lefki, K. and Dormans, G.J.M., J. Appl. Phys., 1994. **76**: p. 1764.

177. Lee, W., Jeong, M.C., and Myoung, J.M., Nanotechnology, 2004. **15**: p. 254.

178. Damjanovic, D., Phys. Rev. B, 1997. **55**: p. R649.

179. Damjanovic, D., J. Appl. Phys., 1997. **82**: p. 1788.

180. Schreiber, P. and et al. in *Proc. SPIE 3629*. 1999.

181. Takahashi, Y., et al., Jpn. J. Appl. Phys., 1994. **33**: p. 6611.

182. Liu, M.J., *Study of Ultra-thin zinc oxide epilayer growth and UV detection properties*. 2003, University of Pittsburgh.